Mechanisms for Intrinsic Stress Evolution during and after Polycrystalline Film Growth

by

Hang Yu

B.S. Physics, Peking University, 2007

Submitted to the Department of Materials Science and Engineering in Partial Fulfillment of the Requirement for the Degree of

DOCTOR OF PHILOSOPHY

at the

Massachusetts Institute of Technology

June 2013

Signature of Author: _____

February 26, 2013. Department of Materials Science and Engineering

Certified by: _____

Carl V. Thompson

Stavros Salapatas Professor of Materials Science and Engineering

Director, Materials Processing Center

Thesis Supervisor

Accepted by: _____

Gerbrand Ceder

Chair, Departmental Committee on Graduate Students

Mechanisms for Intrinsic Stress Evolution during and after Polycrystalline Film Growth

by

Hang Yu

Submitted to the Department of Materials Science and Engineering on February 26, 2013 in Partial Fulfillment of the Requirement for the Degree of

DOCTOR OF PHILOSOPHY

ABSTRACT

Growth of polycrystalline films involves poorly understood kinetic processes that occur far from equilibrium and lead to complex co-evolution of the surface, microstructure and intrinsic stress of the films. Here we present a comprehensive study consisting of *in situ* stress measurements, microstructure characterization, and analytical modeling for various polycrystalline systems. We find that in systems of high atomic mobility, the stress change after polycrystalline film growth can be attributed to a fast reversible surface process and a slow irreversible bulk process. The fast process is weakly dependent on temperature and is associated with changes in the shape of grain surfaces. The slow process is strongly dependent on temperature and is mostly associated with grain growth in the bulk of the film. We also discovered a turnaround phenomenon in which, under conditions of intermediate atomic mobility, the stress evolves from a tensile toward a compressive state, and then turns around to evolve toward a tensile state. This stress turnaround phenomenon is strongly dependent on the substrate temperature and deposition rate, and can be attributed to an increase of the grain size during film deposition. Grain growth during deposition not only leads to a tensile component of the intrinsic stress, but also changes the

grain size dependence of the compressive component. The compressive component results from incorporation of excess adatoms in grain boundaries, and the magnitude of the compressive stress is controlled by a competition between adatom incorporation in 2D islands and incorporation at grain boundaries. We also investigated the effect of the angle of incidence of the flux of depositing atoms on stress and structure evolution during polycrystalline film growth. We find that as the angle of incidence increases, the coalescence thickness increases and the stress becomes less compressive or more tensile. We attribute these phenomena to the enhanced surface roughness, the shadowing effect, the steering effect and the presence of Ehrlich-Schwoebel barriers during oblique angle deposition. All these effects lead to suppression of the adatom-grain boundary incorporation process.

Based on this thesis work, intrinsic stresses in polycrystalline films can be categorized into three types: Type I, the intermediate type and Type II. These behaviors are observed in systems of low, intermediate and high atomic mobility, respectively. Compressive stresses develop in Type II behavior and tensile stresses develop in Type I behavior. The transition of the stress behavior from Type I, to the intermediate type and to Type II is continuous and can be achieved by adjusting deposition conditions. Whether the post-coalescence stress is tensile, or compressive, or evolving from compressive to tensile depends on the homologous temperature, the deposition rate and the angle of the incidence of the flux of depositing atoms.

Thesis Supervisor: Carl V. Thompson

Title: Stavros Salapatas Professor of Materials Science and Engineering

Director, Materials Processing Center

I dedicate this thesis to my parents.

ACKNOWLEDGEMENTS

First, I would like to thank my advisor Professor Carl Thompson, whose support and guidance have been indispensible for this work. In many ways, especially through the long-term discussion on the stress models, he has taught me how to think deeply and critically, and how to communicate as a scholar. His attitude, passion, wisdom and enthusiasm for science are impressive and enlightening. I sincerely hope his mentoring and guidance can continue as I explore my scientific career in the future. I would also like to thank the members of my thesis committee, Professor Samuel Allen and Professor Christopher Schuh, for their time and insightful comments. They have been incredibly helpful during this process and it is my great pleasure to work with them.

I would like to thank the past and present members in the Thompson group. For the former group members, in particular, I would like to thank Steven Boles and Qiang Quo, with whose help and encouragement I was able to overcome the hard times in the second year. Other senior students had also been helpful. For the present members, I would like to thank Robert Mitchell for his help and knowledge in the lab and wish him all the best with his future job in Intel. I would like to thank Dr. Dan for his help for making cross-sectional TEM samples. I wish all the other group members best luck in their pursuits of Ph.D.

A special thank goes to my technician friends, Kurt Broderick and Dave Terry. During my initial years at MIT, they had been extremely helpful whenever I had a problem with the vacuum system. Discussion with them gained me practical knowledge in the lab and it was always a lot of fun to talk about non-technical things with them, such as culture, food and politics. I would also like to thank our group technician Richard Perilli, whose expertise on vacuum systems has been amazingly helpful to me during the past year.

Most importantly, I owe my sincere gratitude to my family. Over the years, I have been privileged with Mom's love and wisdom and Dad's smartness and humor. The weekly

video meetings with them have been a panacea whenever I was frustrated with the vacuum system and research progress. Finally, I would like to thank my beautiful and brilliant wife, Yunhui, who has always been supporting and believing in me. Her love, push and encouragement constantly move me forward, and in the right direction. I have also been impressed with and benefited from her knowledge on physics, programming, reading and cooking. After living in different places for many years, I hope we can eventually move together as she completes her Ph. D. in the near future.

TABLE OF CONTENTS

LIST OF FIGURES

LIST OF TABLES

CHAPTER 1

INTRODUCTION

1.1 MOTIVATION

Complex kinetic processes are involved during the growth of polycrystalline films, which is typically carried out far from equilibrium. Minor changes in processing conditions can lead to tremendous differences in surface morphology, grain structure and residual stress in the films, which strongly influence their performance and reliability in a rich variety of applications, ranging from nano- and microelectromechanical devices and systems (N/MEMS)[1, 2], protective coatings [3, 4], to magnetic, plasmonic, flexible electronic and medical device[5-9]. Control of the residual stress is especially important in applications based on microbeam structures, such as electrically actuated switches and accelerometers [10, 11]. For example, in a doubly supported beam structure, an average compressive stress on the order of 10MPa can cause buckling, while a tensile stress of similar magnitude can change the beam's effective spring constant. Figure 1.1 shows the problems caused by residual stresses in released micro-structures and devices.

From the point of view of applications, it is thus critical to comprehensively understand the underlying mechanisms for structure and stress evolution during polycrystalline film growth, so that the properties and residual stresses of these films can be tailored to meet specific engineering goals. From the point of view of fundamental science, understanding the complex

processes associated with the surface and grain structures, and their effects on intrinsic stress evolution can lead to an improved understanding of the general physics far-from-equilibrium, the theoretical framework for which has not yet been established.

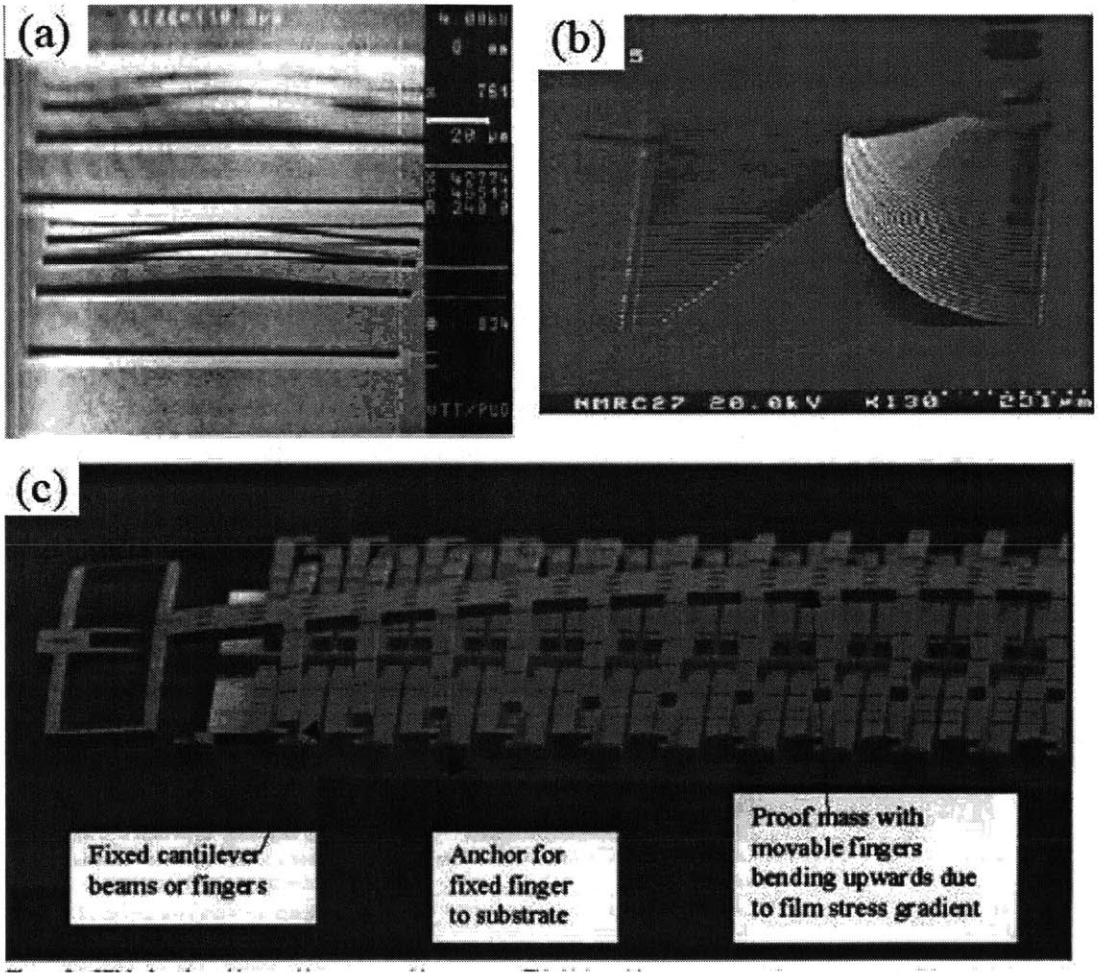

Figure 1.1. SEM images of (a) a released doubly-supported micro-beams under a compressive stress [11], (b) curved cantilevers due to a stress gradient [11] and (c) an accelerometer with extreme positive curvature caused by residual compressive stress in the shuttle mass [10].

1.2 FAR-FROM-EQUILIBRIUM GROWTH OF THIN FILMS

Vapor phase growth of thin films always involves far-from-equilibrium processes. Take evaporative deposition as an example. When the source material is heated above its melting point, source atoms escape from the crucible, travel through the vacuum and eventually arrive on cold substrates. Based on thermodynamics, the equilibrium vapor pressure of a condensed phase strongly depends on temperature T [12]:

$$P_e \propto (k_B T)^{1/2} \exp(-\frac{L_0}{k_B T}). \tag{1.1}$$

Here, k_B is the Boltzmann constant, and L_0 is a constant that can be viewed as the sublimation energy. Because of the significant difference between the source and substrate temperature, the actual vapor pressure P at the substrate is much greater than its equilibrium vapor pressure P_e, which gives rise to a large supersaturation. Under typical deposition conditions, for instance, the vapor pressure of Ni at the surface of a room temperature substrate is on the order of $10^{-7} Torr$, whereas its equilibrium vapor pressure at room temperature is on the order of $10^{-63} Torr$ [13]. This leads to a large thermodynamic driving force for phase condensation:

$$\Delta\mu = k_B T \ln(\frac{P}{P_e}) = 128.9 k_B T = 3.35 eV \tag{1.2}$$

1.2.1 CONDENSATION, ADATOM DIFFUSION, NUCLEATION AND COALESCENCE

The kinetic energy of arriving atoms depends on the specific deposition techniques, with ~0.1eV for evaporative deposition and ~1-10eV for sputter deposition [14]. When approaching the substrate surface, atoms are accelerated by attractive force from the substrate. Upon condensation, most of the kinetic energy of the atoms is lost to substrate by heat dissipation. Insufficient dissipation of energy causes desorption of the atoms from the substrate. Those atoms that dissipate enough energy stick to the substrate and become adatoms, which are able to diffuse on the substrate surface before coming to rest in surface sites at which they will have low chemical potentials. 2D random walk theory predicts that adatom diffusion follows:

$$<|\vec{r}(t)-\vec{r}(0)|^2>=4Dt\,, \tag{1.3a}$$

where

$$D=\frac{1}{4}a^2\nu_0 e^{-E_a/k_BT}\,. \tag{1.3b}$$

Here $\vec{r}(t)$ and $\vec{r}(0)$ denote the position of an adatom at time t and time zero. D is the surface diffusion coefficient for adatoms; a and ν_0 are the jump distance and attempt frequency; E_a is the energy barrier for diffusion. The adatom surface diffusion coefficient should be distinguished from the collective surface diffusion coefficient in Fick's Law. In low coverage

limits, however, the two can be viewed as identical. The high driving force for condensation and the low temperature for adatom diffusion lead to complex and kinetics dependent surface morphology during thin film deposition.

The early stage of thin film growth is strongly influenced by the substrate surface. If the substrate is crystalline, homoepitaxial or heteroepitaxial growth can occur, depending on whether the film and substrate are of the same material. Homoepitaxial growth often proceeds in a layer-by-layer mode, in which a single layer of atoms is formed by nucleation, growth and coalescence of 2D islands. For heteroepitaxial growth, depending on the relationship of surface and interface energies and experimental conditions, the growth can be in the Volmer-Weber mode, Stranski-Krastanov mode or Frank-van-der-Merwe mode (i.e. a layer-by-layer mode)[15].

If the substrate is noncrystalline, the film is expected to grow in the Volmer-Weber mode. Initially, adatoms diffuse on the amorphous surface and nucleate to form clusters. If we define n^* as the critical cluster size so that the minimum stable cluster consists of n^*+1 atoms. The nucleation rate I depends on the deposition rate R and the substrate temperature T as [16]

$$I = I_0 R^{n^*} \exp(\frac{-\Delta G_{n^*}}{k_B T}). \tag{1.4}$$

Here ΔG_{n^*} is the energy to form a cluster of size n^* and I_0 is a constant independent of temperature and deposition rate. Under normal experimental conditions for physical vapor deposition, a dimer is stable on the surface, i.e. $n^*=1$. Equation (1.4) suggests that the nucleation rate increases with deposition rate. The critical cluster size is inversely

proportional to the supersaturation [16]. As the substrate temperature is increased, the supersaturation decreases; the critical cluster size increases so that ΔG_{n^*} also increases. It is thus difficult to determine the temperature dependence of the nucleation rate solely based on Equation (1.4). Nevertheless, empirically, it is generally found the nucleation rate decreases with increasing temperature [16].

As more atoms arrive, the clusters grow to become 3D islands. Lateral growth of these single crystal islands results in island impingement and grain boundary formation. When the distance between the two islands is small enough, the lateral attractive force could cause them to snap together by a 'zipping process'[17], which is considerably faster than surface diffusion. *In situ* Scanning Tunneling Microcopy (STM) experiments on Ag film growth by Polop *et al.* [18] showed that at this stage, the in-plane shape of the resulting islands (in which grain boundaries are observed) is irregular and meandering. This observation indicates that the grain boundary mobility is insufficient for grain boundaries to be removed so that surface diffusion can allow the islands to develop compact shapes. This is probably because the islands have grown too large for surface diffusion to be sufficient. In the next stage of growth, further condensation, surface diffusion and grain boundary zipping result in network formation to the point of percolation, followed by full coalescence to form a film. *In situ* STM results of early stage growth of Ag films are shown in Figure 1.2. Because the in-plane crystallographic orientations of the 3D islands are random, numerous grain boundaries are formed as the film becomes continuous. One example of Volmer-Weber systems is room temperature deposition of gold films on a silicon nitride substrate, with a coalescence thickness of ~ 10nm and coalescence grain size of ~ 10-15 nm.

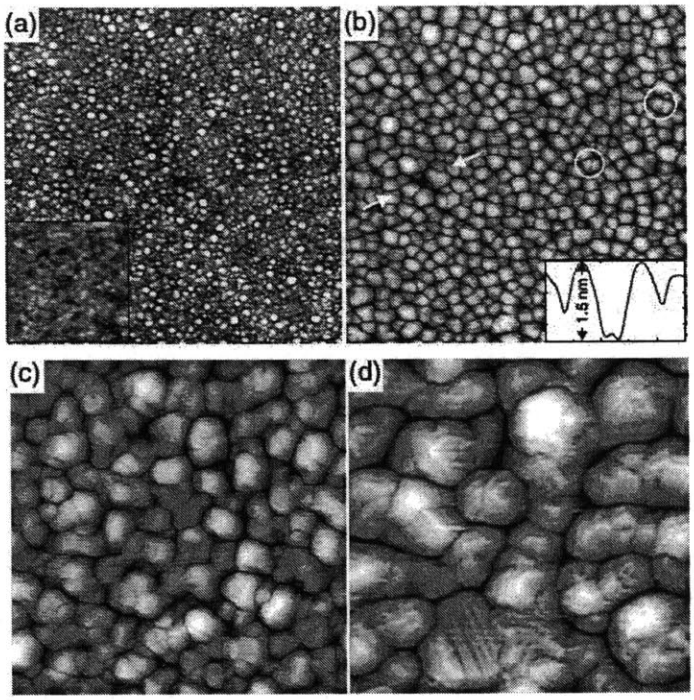

Figure 1.2. Surface topography of Ag films (deposited at 300K) measured using in situ STM. From (a) to (d), the film thicknesses are 0.3 nm, 1.0 nm, 2.7 nm, and 8.5 nm. The image size is $160nm \times 160nm$ [18].

1.2.2 POSTCOALESCENCE GROWTH

Once the film becomes fully continuous, i.e. in the post-coalescence stage, new atom layers start to deposit on individual grain surfaces, in a layer-by-layer homoepitaxial way. Because of ongoing grain boundary zipping, the grain surfaces remain relatively flat during subsequent deposition. For a 60nm thick Ni film deposited at room temperature, the RMS (root mean square) roughness is only ~1nm.

Different microstructures can develop based on atomic mobility after coalescence, as illustrated in Figure 1.3(a). For low mobility systems such as Cr, Fe, Ta, and W deposited at room temperature, adatom diffusivities are low. As a result, only grain thickening as grain-by grain epitaxial growth occurs. As the film further thickens, the in-plane grain size becomes small compared to the film thickness, leading to columnar structures. Post-deposition annealing can cause grain growth and lead to a more equiaxed grain structure. On the other hand, for high mobility systems like Au, Ag, Cu, and Al deposited at room temperature, the microstructure keeps evolving during deposition—grain growth results in equiaxed grain structures, in which the in-plane and through-thickness grain sizes of most grains are comparable in the as-deposited films. In addition, abnormal grain growth can occur during deposition and during post-deposition annealing. This often leads to a bimodal distribution of the grain size, featured by abnormal large grains embedded into numerous small matrix grains (see the sketch in Figure 1.3(b)).

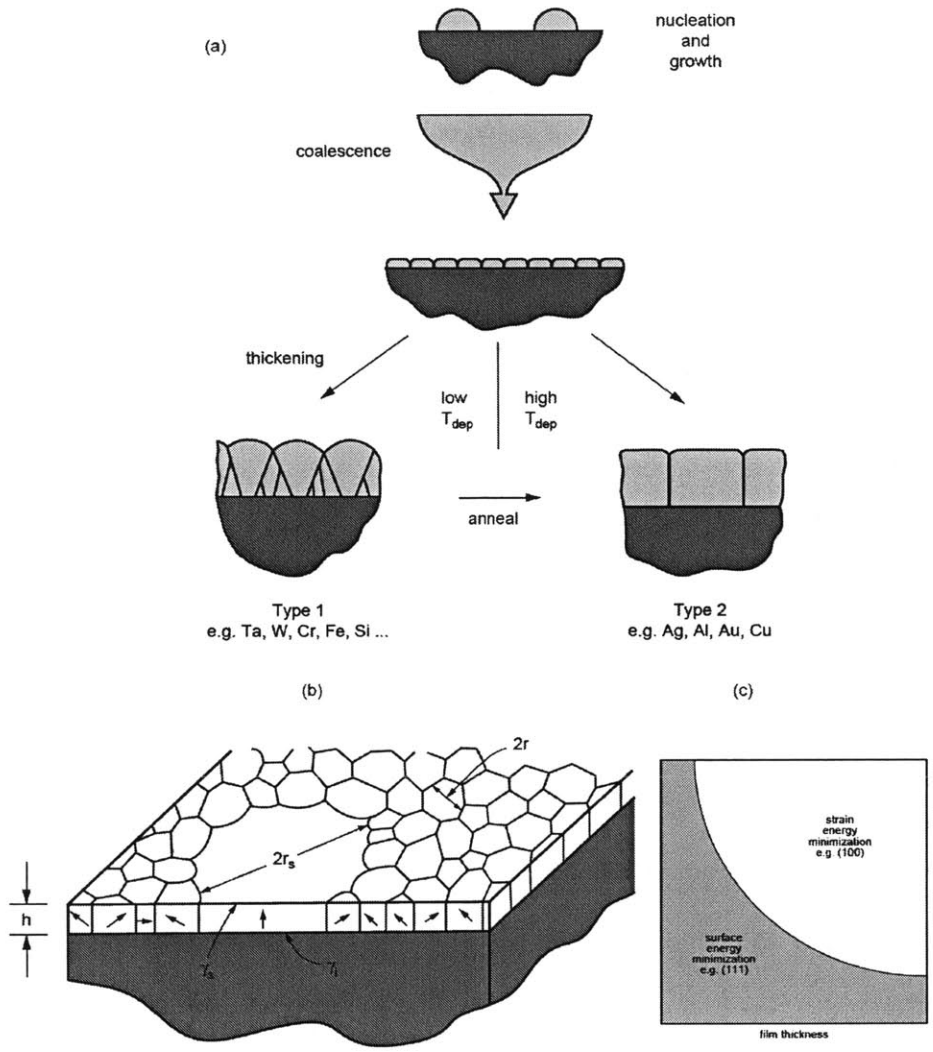

Figure 1.3 [16]. (a) Cross sectional view of grain structure evolution during Volmer-Weber growth of metallic thin films. (b) Bimodal distribution of grain size due to abnormal grain growth. (c) A texture map for the texture resulting from grain growth of metallic thin films with different thickness and strain.

Grain growth can occur both during deposition and during post-deposition processing. Normal grain growth is driven by the reduction of grain boundary area. The corresponding energy change is

$$\Delta E_{gb} = \overline{\gamma_{gb}}\left(\frac{2}{\overline{d_0}} - \frac{2}{\overline{d}}\right), \tag{1.5a}$$

where $\overline{\gamma_{gb}}$ is the average grain boundary energy, and $\overline{d_0}$ and $\overline{d}$ are the average grain size in the film before and after grain growth. In contrast, abnormal grain growth is often driven by minimization of surface and interface energy, which results in preferred growth of grains with specific out-of-plane orientations. The related energy change for this type of abnormal grain growth is

$$\Delta E_{s/i} = (\Delta\gamma_s + \Delta\gamma_i)\frac{1}{h}, \tag{1.5b}$$

where $\Delta\gamma_s$ and $\Delta\gamma_i$ are the reduction of surface and interface energy due to growth of abnormal grains and h is the film thickness. Grain growth can also change the strain energy in the film by changing the stress state due to film densification and by changing the biaxial modulus, which is a function of crystallographic orientation. The related energy change is

$$\Delta E_{\varepsilon} = \frac{1}{2}(M_0\varepsilon_0^{\,2} - M\varepsilon^2). \tag{1.5c}$$

Here M_0 and M are the biaxial modulus, and ε_0 and ε are the biaxial strain in the film before and after grain growth. When the film is thin, surface and interface energy minimization dominates, so that films of FCC metals generally have (111) planes parallel to the plane of the film. In the case that strain energy dominates the energetic term, the films with FCC structures are likely to develop a (100) texture because this texture has the lowest biaxial modulus and therefore minimizes strain energy. Texture evolution in the films depends on film thickness as well as processing conditions and history. Figure 1.3(c) shows a texture map resulting from grain growth under different conditions [16].

All the key processes involved in structure evolution, such as adatom diffusion, cluster nucleation, island coarsening and grain growth are thermally activated kinetic processes. Because of the far-from-equilibrium nature of thin film growth, the energetic and kinetic effects are interwoven during deposition and post-deposition processing. Any deviation from thermodynamic predications should have a kinetic explanation. Experimentally, substrate temperature, deposition rate, vacuum conditions, the angle of the incidence the flux of depositing atoms, substrate topography and intrinsic stresses all play important roles in the structure evolution and texture development processes.

1.3 INTRINSIC STRESSES IN THIN FILMS

Because of the far-from-equilibrium nature of the deposition process, and because of traction at the substrate-film interface, complex intrinsic stresses develop and evolve during and after thin film growth. Thin films are generally considered to be in a plane stress state. If we define

the out-of-plane direction (normal to the free surface) as the z direction, then $\sigma_z = 0$. For an isotropic system, the strain-stress relation is:

$$\varepsilon_x = \frac{1}{E}(\sigma_x - \nu\sigma_y)\ , \varepsilon_y = \frac{1}{E}(\sigma_y - \nu\sigma_x), \text{ and } \varepsilon_z = -\frac{\nu}{E}(\sigma_x + \sigma_y), \tag{1.6a}$$

where E and ν are the Young's modulus and Poisson's ratio. In the case of equal biaxial strain ($\varepsilon_x = \varepsilon_y = \varepsilon$), we have $\sigma_x = \sigma_y = \sigma$ and $\varepsilon = \frac{1-\nu}{E}\sigma$. The biaxial modulus is defined as

$$M = \frac{\sigma}{\varepsilon} = \frac{E}{1-\nu}. \tag{1.6b}$$

Under normal deposition conditions, in which grains are randomly oriented or have a (111) or (100) texture, the in-plane elastic properties of FCC polycrystalline films are isotropic. The in-plane elastic properties of a single crystal film or a polycrystalline film with asymmetric grain structures (e.g. caused by oblique deposition) can be anisotropic. For instance, for a cubic single crystal film FCC with a (110) plane normal to the z-axis, the elastic moduli are different in the mutually perpendicular [001] and [$\bar{1}$10] directions.

1.3.1 STRESS MEASUREMENT

Intrinsic stress or residual stress in thin films can only be measured indirectly. With knowledge of the elastic properties and equilibrium lattice constant (d_0) of the film, we can determine the intrinsic stress by measuring the elastic strain along the z direction using X-ray

diffraction: $\sigma = -\frac{E}{2\nu}\varepsilon_z$. This method can be improved with higher precision based on a tensor transformation. The strain in a Cartesian coordinate system can be transformed to any arbitrary direction (Ψ, φ) by the orthogonal matrix [19]

$$a_{ij}^{LS} = \begin{pmatrix} \cos\varphi\cos\Psi & \sin\varphi\cos\Psi & -\sin\Psi \\ -\sin\varphi & \cos\varphi & 0 \\ \cos\varphi\sin\Psi & \sin\varphi\sin\Psi & \cos\Psi \end{pmatrix}$$ (Figure 1.4).

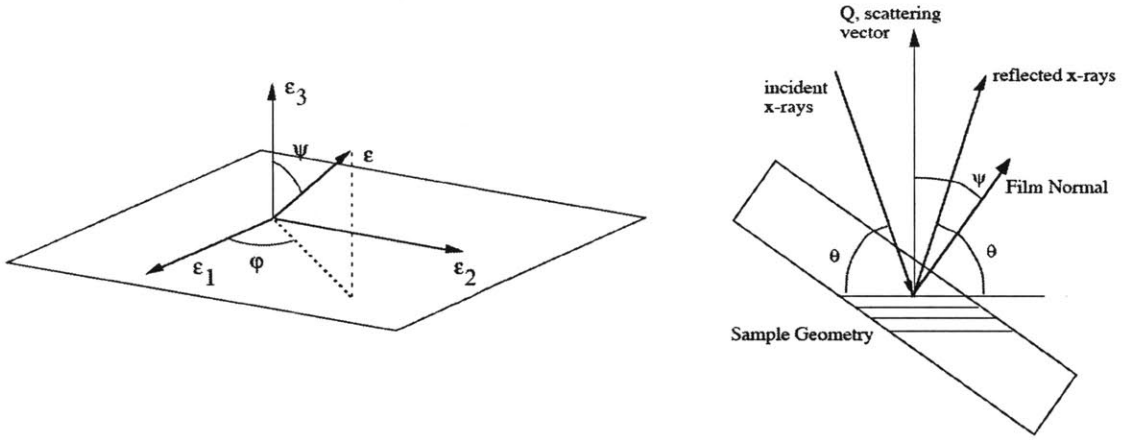

Figure 1.4. Left: principal coordinates for strains in thin films. Right: sample geometry for non-symmetric x-ray diffraction [20].

In the case of an equal biaxial stress, the strain in the Ψ direction is

$$\varepsilon_\Psi = \frac{1+\nu}{E}\sigma\sin^2\Psi - \frac{2\nu}{E}\sigma \ , \qquad (1.7a)$$

and the measured lattice constant in the Ψ direction d_Ψ can be derived [20] as

$$d_\Psi = [1 - \frac{2\nu}{E}\sigma]d_0 + \sigma d_0 \frac{1+\nu}{E}\sin^2\Psi . \qquad (1.7b)$$

The equilibrium lattice constant d_0 can be measured in the Ψ^* direction, where $\Psi^* = \sin^{-1}[(\frac{2\nu}{1+\nu})^{1/2}]$. The biaxial stress can then be determined from the slope in the $d_\Psi - \sin^2\Psi$ plot.

Using the wafer curvature method [21], the intrinsic stress can be measured without knowing the film's elastic properties. When the film is deposited on a wafer, the stress in the film causes the wafer to bend. If the film is much thinner than the wafer, Stoney's equation [22] shows that the force per unit width ($\frac{F}{w}$) exerted at the substrate-film interface can be determined by measuring the curvature of the wafer:

$$(\frac{F}{w}) = M_s \frac{\kappa h_s^2}{6}, \qquad (1.8)$$

where M_s, h_s and κ are the biaxial modulus, thickness and curvature of the substrate, respectively. A force balance leads to

$$(\frac{F}{w}) = \bar{\sigma} \times h_f + S . \qquad (1.9)$$

Here, h_f is the film thickness, $\overline{\sigma}$ is the average stress in the bulk of the film, and S is the surface stress.

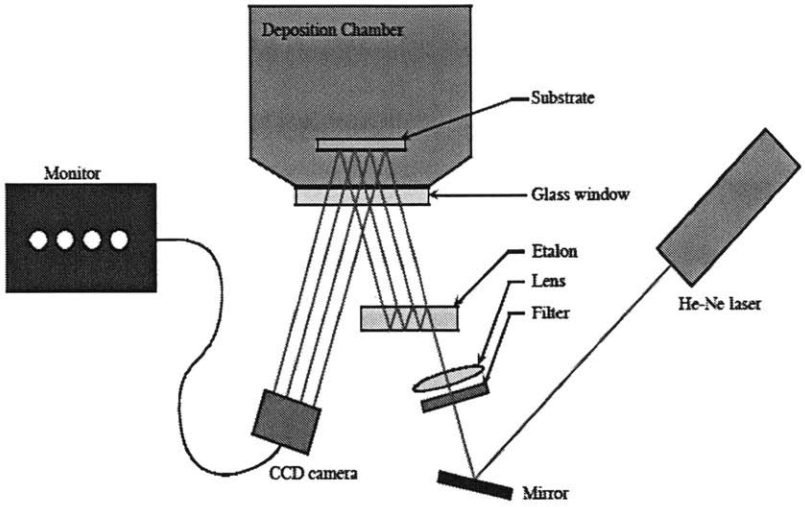

Figure 1.5. Drawing of a MOSS system for *in situ* stress measurement [20].

The first way developed to accurately measure the substrate curvature is to scan a laser beam along the curved surface [21], while measuring the position of the reflected beam. As a laser beam is scanned across the surface of the wafer, the beam reflects at different angles. The curvature is thus measured by detecting the reflected beam using a position sensitive photodetector. As a second method, Multibeam Optical Stress Sensor (MOSS) (illustrated in Figure 1.5) enables quick measurements of the curvature without scanning the laser beam [20, 21]. A single laser beam transmitting through an etalon generates multiple parallel output beams. When reflecting from a curved surface, the separation of each reflected beam changes, from which the substrate curvature can be determined. In a third technique, when a film is

deposited on a cantilever, the curvature or the deflection of the cantilever can be monitored by measuring the capacitance between the cantilever and a fixed electrode.

1.3.2 STRESS EVOLUTION IN POLYCRYSTALLINE FILMS

Both MOSS and the capacitance sensor enable *in situ* stress measurement during deposition. Depending on the homologous temperature of the system, or the atomic mobility, two types of intrinsic stress evolution behaviors have been identified in polycrystalline systems [23-25], as schematically shown in Figure 1.6 (a). Type I behavior is observed in low atomic mobility systems, represented by refractory metals (e.g. Ti, Cr, and W) deposited at room temperature, and Type II behavior is observed in high atomic mobility systems, including metals with low melting points (e.g. Au, Ag, and Cu) deposited at room temperature and refractory metals deposited at elevated temperatures.

For low atomic mobility systems, the stress remains tensile in all growth stages with no relaxation observed during growth interruptions. On the other hand, high atomic mobility systems usually develop a much more complicated stress behavior. After an initial compressive dip during deposition of the first few monolayers, a tensile rise is observed up to roughly 100-150 Å, during which isolated islands start to impinge and coalesce until the film becomes fully continuous. The instantaneous stress , or the slope of the stress curve, shifts to compressive in the postcoalescence stage. Eventually the overall measured $(\frac{F}{w})$ becomes negative, so the average stress becomes compressive. When the growth is stopped, a change in the stress is always observed in the tensile direction. Intriguingly, upon resumption of

growth, the stress rapidly returns to the pre-interruption stress trajectory and continues as if the growth had never been interrupted. This is the so-called reversible stress [26-28], shown in Figure 1.6(b).

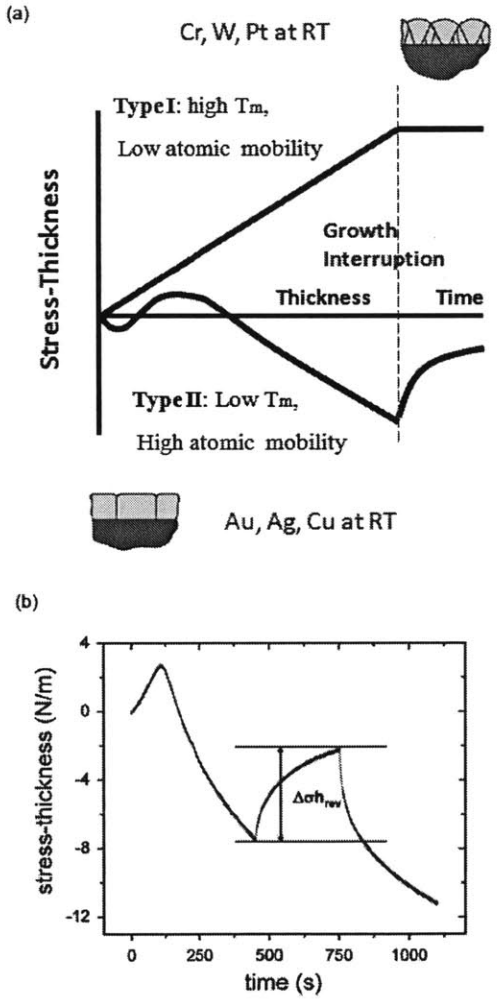

Figure 1.6. (a) Schematics of stress evolution history during Volmer-Weber Growth. (b) The reversible stress: measured stress evolution for a gold film deposited on SiNx at300K, 1.0Å/s [31].

It is generally believed that these complex stress behaviors originate from surface and grain structure evolution during deposition. The initial compressive stress observed in Type II systems might be attributed to the adatom-substrate interaction or the Laplace [29, 30] pressured caused by surface stress on the islands. The tensile coalescence stress in both Type I and Type II systems relates to island impingement and network formation. The temperature dependence of the postcoalescence stress suggests the important roles played by the kinetic processes on the film surface, such as diffusion of adatoms on terraces and incorporation of adatoms to clusters. In terms of the stress behavior during a growth interruption, especially the 'reversible stress', quite a few models have been proposed and the underlying mechanisms are still under debate. Previously proposed models for the initial compressive stress, the tensile coalescence stress and the reversible compressive stress will be reviewed in Chapter 2.

1.4 OVERVIEW OF THE THESIS

From both the point of view of applications and fundamental science, understanding the underlying mechanisms for intrinsic stress evolution in polycrystalline films is of great importance. To date, however, a model that can self-consistently explain all the stress behaviors observed during growth and growth interruption has not been developed. This is partially because the previous models are mainly based on the measured stress curves, with relatively little characterization of the surface and microstructure evolution that accompanies stress evolution.

This thesis work aims at systematically solving this problem. To accomplish this goal, an inclusive study consisting of *in situ* stress measurements, surface, microstructure and texture

characterization, and analytical modeling has been carried out for various polycrystalline systems, under different kinetic conditions. Stress evolution in thin films is measured *in situ* as a function of material type, substrate temperature, deposition rate, film thickness, angle of the incident atomic flux, and interruption time. The results led to initial hypotheses about the underlying mechanisms. We then tested these hypotheses and developed analytic models based on further stress measurements and characterization of surface topography evolution and grain structure evolution of the films. Cycles of test and analysis ultimately led to a comprehensive understanding of the stress evolution mechanisms during and after polycrystalline film growth.

With the current chapter serving as the introduction, our investigation of stress evolution mechanisms will proceed as follows. To 'gain new knowledge by reviewing old' (Confucius quotes), the previously proposed stress evolution mechanisms are reviewed in detail in Chapter 2. This starts from a general discussion on sources of stress in thin films, followed by an introduction of the Laplace pressure model [29, 30] and the Nix-Clemens-Hoffman model [17, 32], which have been used to explain the stress behavior before and during coalescence. After that, we discuss models for the origin of the postcoalescence compressive stress observed in Type II systems. In these models, surface defects, adatom populations, grain boundaries and island stress are considered as the origin of the reversible compressive stress.

The experimental methods of this work are presented in Chapter 3. We first introduce the ultra high vacuum (UHV) e-beam evaporation system used for polycrystalline film growth. Second, we describe the capacitance-based sensor for *in situ* stress measurement. In particular, a tiltable platform enabling stress measurement for arbitrary angles of incidence of the

evaporant flux. The characterization methods for surface topography, microstructure and texture will then be reviewed, including the method through which the grain size distributions were quantified, and roughness and inclination angles of the surface were quantified. Finally, the methods for heating and quenching the samples inside the vacuum chamber are discussed.

The subsequent three chapters represent the core results of the thesis research. Chapter 4 focuses on understanding the mechanisms leading to stress evolution during interruptions of Volmer-Weber growth. By measuring the stress evolution as a function of interruption time-scales, the film thickness, and the substrate temperature, a fast process and a slow process are identified during long interruptions of growth. Grain growth is discovered during interruption of gold film growth. By measuring the grain size as a function of interruption time, we calculate the densification stress caused by grain growth and compare it with the stress evolution measured during the slow process. The fast process is proposed to be associated with a change of shape of the grain surface. Characterization of surface topography supports this proposal.

In Chapter 5, we elucidate the postcoalescence stress evolution in all three types of Volmer-Weber systems, i.e. the systems of low, intermediate and high atomic mobility. A previously unobserved 'stress turnaround' behavior that occurs at intermediate homologous temperatures was investigated. We found that the grain size scales with film thickness in Ni films under such conditions. A model is developed to quantify the influence of grain growth during deposition on the instantaneous stress. After that, we discuss the processes of adatom incorporation into 2D islands on the film's surface and to the surface sites of grain boundaries. A new analytical model is built to quantify the influence of these processes on the

instantaneous stress. Grain growth and adatom-grain boundary (GB) incorporation are then shown to be important processes that affect stress evolution during postcoalescence growth. Stress curves predicted by the model capture all of the important features of those curves obtained from *in situ* measurements. The chapter concludes with an updated stress categorization scheme, including a summary of the stress behaviors, underlying mechanisms and representative systems.

Chapter 6 provides a comprehensive study of the structure and stress evolution in Ni and Au films when the evaporant flux arrives at different angles of incidence. After a brief literature review on oblique angle deposition, we show experimental results of *in situ* stress measurement, surface topography evolution and grain structure evolution in Ni and Au films deposited at different incidence angles. At a higher angle of incident flux, the dome height increases, the grain size slightly decreases, and the stress in the film becomes less compressive or more tensile. These phenomena can be attributed to the shadowing effect, enhanced surface roughness and the presence of Ehrlich-Schwoebel barriers.

Finally, the key findings of this dissertation are summarized in Chapter 7. We also propose potential future directions for this work. These directions include the influence of incidence angle on reversible stress evolution, the effects of substrate topography and chemistry on stress and structure evolution, stress evolution in films of controlled microstructure or of very low melting temperatures, and the use of laser scattering techniques for *in situ* measurement of surface roughness during deposition and growth interruptions.

REFERENCES

[1] M. Li, H. X. Tang, and M. L. Roukes, Nature Nanotechnology **2**, pp. 114 (2007).

[2] S. M. Spearing, Acta Materialia **48**, pp. 179 (2000).

[3] J. E. Gray, and B. Luan, Journal of Alloys and Compounds **336**, pp. 88 (2002).

[4] N. P. Padture, M. Gell, and E. H. Jordan, Science **296**, pp. 280 (2002).

[5] C. de Haro, R. Mas, G. Abadal, J. Munoz, F. Perez-Murano, and C. Dominguez, Biomaterials **23**, pp. 4515 (2002).

[6] M. T. Johnson, P. J. H. Bloemen, F. J. A. denBroeder, and J. J. deVries, Reports on Progress in Physics **59**, pp. 1409 (1996).

[7] D. H. Kim *et al.*, Science **320**, pp. 507 (2008).

[8] S. A. Maier, and H. A. Atwater, Journal of Applied Physics **98** (2005).

[9] K. Nomura, H. Ohta, A. Takagi, T. Kamiya, M. Hirano, and H. Hosono, Nature **432**, pp. 488 (2004).

[10] K. Nunan, G. Ready, P. Garone, G. Sturdy, J. Sledziewski, and Ieee, in *2000 Ieee/Semi Advanced Semiconductor Manufacturing Conference and Workshop* (Ieee, New York, 2000), pp. 357.

[11] C. T. Leondes, *MEMS/NEMS : handbook techniques and applications* (Springer, New York, 2006).

[12] J. Venables, *Introduction to surface and thin film processes* (Cambridge University Press, Cambridge ; New York, 2000).

[13] H. L. Johnston, and A. L. Marshall, Journal of the American Chemical Society **62**, pp. 1382 (1940).

[14] M. Ohring, *The materials science of thin films* (Academic Press, Boston, 1992).

[15] T. Michely, and J. Krug, *Islands, mounds, and atoms : patterns and processes in crystal growth far from equilibrium* (Springer, Berlin ; New York, 2004), Springer series in surface sciences,, 42.

[16] C. V. Thompson, Annual Review of Materials Science **30**, pp. 159 (2000).

[17] W. D. Nix, and B. M. Clemens, Journal of Materials Research **14**, pp. 3467 (1999).

[18] C. Polop *et al.*, New Journal of Physics **9** (2007).

[19] M. Birkholz, P. F. Fewster, and C. Genzel, *Thin film analysis by X-ray scattering* (Wiley-VCH ;John Wiley, distributor, Weinheim Chichester, 2006).

[20] W. D. Nix, Lecture Notes (2005).

[21] W. D. Nix, Metallurgical Transactions a-Physical Metallurgy and Materials Science **20**, pp. 2217 (1989).

[22] G. G. Stoney, Proceedings of the Royal Society of London Series a-Containing Papers of a Mathematical and Physical Character **82**, pp. 172 (1909).

[23] J. A. Floro, E. Chason, R. C. Cammarata, and D. J. Srolovitz, Mrs Bulletin **27**, pp. 19 (2002).

[24] J. A. Floro *et al.*, Journal of Applied Physics **89**, pp. 4886 (2001).

[25] R. Koch, Journal of Physics-Condensed Matter **6**, pp. 9519 (1994).

[26] F. Spaepen, Acta Materialia **48**, pp. 31 (2000).

[27] C. Friesen, S. C. Seel, and C. V. Thompson, Journal of Applied Physics **95**, pp. 1011 (2004).

[28] C. Friesen, and C. V. Thompson, Physical Review Letters **89** (2002).

[29] R. C. Cammarata, T. M. Trimble, and D. J. Srolovitz, Journal of Materials Research **15**, pp. 2468 (2000).

[30] M. Laugier, Thin Solid Films **79**, pp. 15 (1981).

[31] J. Leib, R. Monig, and C. V. Thompson, Physical Review Letters **102** (2009).

[32] R. W. Hoffman, Thin Solid Films **34**, pp. 185 (1976).

CHAPTER 2

REVIEW OF PROPOSED STRESS MECHANISMS

2.1 SOURCES OF STRESS IN THIN FILMS

Because of traction at the substrate-film interface, the in-plane dimension of a film is fixed by the substrate. Stresses are developed in the film when its equilibrium dimension differs from that of the substrate. When the film is detached from the substrate, the stresses are relaxed. In this section, various sources of stress in thin films are discussed, including thermal stress, epitaxial stress, surface stress and the stresses associated with the defects in the film.

2.1.1 THERMAL STRESS

The linear thermal expansion coefficient of a film (α_f) is always different from that of the substrate (α_s). As a result, thermal stresses develop when the sample is annealed after deposition or cooled down from high temperature processing. The resultant thermal stress in the film is

$$\sigma_{thermal} = -M_f(\alpha_f - \alpha_s)\Delta T . \tag{2.1}$$

Here ΔT is the change of temperature and M_f is the biaxial modulus of the film. For metal films deposited on a silicon substrate, $\alpha_f > \alpha_s$ so that tensile stress develops when the sample

is cooled down from high temperature deposition. The magnitude of the thermal stress can be large under normal processing conditions. Take a Ni film as an example. At $20°C$, $\alpha_{Ni} = 13\times10^{-6}/°C$, $\alpha_{Si} = 3\times10^{-6}/°C$. If the deposition is carried out at $400°C$, the thermal stress in the film is $\sigma = -290GPa(13\times10^{-6}/°C - 3\times10^{-6}/°C)(25°C - 400°C) = 1.0875GPa$, when it is cooled down to room temperature. This number is larger than, or at least comparable to, the yield stress of Ni films. Therefore, thermal cycling often induces plastic deformation of a film [1, 2].

2.1.2 EPITAXIAL STRESS

Consider growth of a film on a dislocation-free single crystal substrate of dissimilar material. If the lattice mismatch between the film and substrate is small, the growth proceeds layer by layer, and the lattice mismatch is accommodated by a uniform strain in the film (pseudomorphic mode). The resultant biaxial stress is

$$\sigma_{epi} = M_f f ,$$

$$f = (\frac{a_s - a_f}{a_s}) , \tag{2.2a}$$

where a_s and a_f are the lattice constants of the substrate and the film. When the film is thick enough, misfit dislocations can form at the film-substrate interface to relax the stress in the film. This leads to a reduction of the total energy of the system.

For the misfit dislocations of Burgers vector b and the density ρ_{md}, the biaxial stress in the film reduces to

$$\sigma_{epi} = M_f(f - \rho_{md} b\cos\lambda). \tag{2.2b}$$

Here λ is the angle between the Burgers vector and the direction that is not only normal to the dislocation line but also lies within the plane of the interface [3]. For a film of thickness h, the strain energy due to formation of misfit dislocations is

$$E_{strain} = M_f h(f - \rho_{md} b\cos\lambda)^2. \tag{2.3a}$$

The dislocation energy per unit area can be derived [3] as

$$E_{misfit\_dislocation} = \rho_{md}\frac{Gb^2}{2\pi(1-\nu)}(1-\nu\cos^2\beta)\ln(\frac{4h}{b}), \tag{2.3b}$$

where G and ν are the shear modulus and Poisson's ratio of the film, and β is the angle between the Burgers vector and the dislocation line [3]. Therefore, the total energy per unit area is

$$E_{total} = M_f h(f - \rho_{md} b\cos\lambda)^2 + \rho_{md}\frac{Gb^2}{2\pi(1-\nu)}(1-\nu\cos^2\beta)\ln(\frac{4h}{b}). \tag{2.4}$$

The critical thickness h_c can be determined by setting $\frac{\partial E_{total}}{\partial \rho_{md}}\Big|_{\rho_{md}=0} = 0$. This leads to

$$\frac{h_c}{\ln(\frac{4h_c}{b})} = \frac{b}{8\pi\cos\lambda(\frac{a_s - a_f}{a_s})}\frac{1-\nu\cos^2\beta}{(1+\nu)}. \qquad (2.5)$$

For systems with large lattice mismatch (e.g. a Ag film on Cu substrate, the lattice mismatch is $\frac{4.09\text{Å}-3.61\text{Å}}{3.61\text{Å}} = 13.3\%$), the epitaxial stress relaxes before the first layer becomes continuous.

2.1.3 SURFACE STRESS

The electronic structure of the surface differs from that of the bulk of the material. As a result, the equilibrium lattice spacing of the surface atoms differs from the bulk lattice spacing. The epitaxial constraint imposed on the surface atoms from the bulk atoms causes a strain in the surface layer. This is the origin of the surface stress.

The surface stress f is defined as the reversible work per unit area to elastically stretch a surface, while the surface energy γ is defined as the reversible work per unit area used to form a surface [4]. For liquids, the two are identical because the concentration of surface

atoms remains constant as the surface is stretched. For solids, the two are different. The Shuttleworth [5] equation states that

$$f_{ij} = \frac{d(\gamma A)}{dA} = \frac{\gamma dA + A d\gamma}{dA} = \gamma \delta_{ij} + A \frac{\partial \gamma}{\partial \varepsilon_{ij}}. \tag{2.6}$$

Here, A, δ_{ij} and ε_{ij} are the surface area, Kronecker delta and surface strain, respectively. The surface stress of a liquid is positive by definition. Semi-empirical potentials and first principles calculations show the majority of the surface stresses of solids are positive and of the same order of magnitude as the surface energy [4]. Having said that, it should be noted that the surface reconstructions observed on clean surfaces of Pt (111) and Au (111) cause compression of the surface layer relative to the underlying crystal [4].

The tensile surface stress on a convex curved surface leads to compression in the bulk of the material, known as the Laplace pressure. A solid particle (radius r) with an isotropic surface stress of f represents the simplest case of this effect, in which the Laplace pressure is $P = -2f / r$. With good adhesion at the interface, therefore, the surface stress can lead to a compressive stress in the islands before coalescence. A detailed discussion of this mechanism is presented in Section 2.2.

2.1.4 STRESS CAUSED BY DIFFUSION PROCESSES

Excess vacancies and dislocations can be generated during the far-from-equilibrium growth process. For polycrystalline films, surfaces and grain boundaries are sinks for vacancies.

Vacancy annihilation at the surface does not significantly affect the biaxial stress, whereas vacancy annihilation in the grain boundaries causes tensile stress in the film. Doerner and Nix [6] analyzed the vacancy diffusion problem from the bulk to the grain boundaries and concluded that the stress caused by this mechanism increases linearly with the square root of time. However, because the activation energy for vacancy diffusion is high, this effect is not significant except for depositions at very high substrate temperatures.

In addition, grain boundary voids [6] might be generated during the far-from-equilibrium growth process. Shrinkage of the voids by diffusion processes can cause tensile stress in the film. The magnitude of the resultant stress strongly depends on the initial void size. The larger the initial void size, the larger the resultant tensile stress. This mechanism requires grain boundary diffusion and may not be important at room temperature.

Another mechanism associated with grain boundary diffusion is the diffusion from the grain boundaries to the free surface. This mechanism can help to relax the compressive stress in the film. The chemical potential of the surface is a function of the surface curvature, while the chemical potential of the grain boundary is a function of the bulk stress. A continuum model requires that the flux of atoms along the grain boundary be equal to the flux along the surface. The detailed analysis by Thouless [7] concluded that the relaxation rate for a grain-boundary diffusion controlled process is

$$\frac{d\sigma}{dt} \simeq -3D_{gb}\delta_{gb}\Omega\frac{\sigma}{k_B T h^2 d}. \qquad (2.7)$$

Here $D_{gb}\delta_{gb}$ is the grain boundary diffusivity, Ω is the atomic volume, d is the grain size and h is the film thickness. From Equation (2.7), the relaxation rate is higher in thinner films, with smaller grains and at higher temperatures. There are some similarities between this mechanism and the mechanism proposed by Chason *et al.*[8], who attributed the stress change during a growth interruption to the flow of atoms from grain boundaries to the surface. However, the model by Chason *et al.* assumes the rate-limiting step is the transition from the grain boundary to the surface rather than grain boundary diffusion. That model will be discussed in detail in Section 2.4.

2.1.5 GRAIN GROWTH

As first pointed out by Chaudhari [9], grain growth in thin films can make the stress in the film less compressive or more tensile because grain boundaries are less dense than the crystal lattice. Δa is defined as the excess volume per unit area of grain boundary. It can be viewed as the separation distance between two ideal crystals, so it is also called the grain boundary width. Consider a spherical grain of initial grain size d_0. The ratio of the volume of grain boundary to the volume of the grain is

$$\frac{V_{gb}}{V_{grain}} = \frac{\pi d_0^{\,2}(\frac{\Delta a}{2})}{\frac{1}{6}\pi d_0^{\,3}} = \frac{3\Delta a}{d_0}. \tag{2.8}$$

If the total volume of the film is V_{film}, then the total volume of grain boundary at time zero is $\frac{3\Delta a}{d_0}V_{film}$. Assume that at time t, the grain size in the film increases to d owing to grain growth. For this reason, at time t the total volume of grain boundary is $\frac{3\Delta a}{d}V_{film}$. The reduction of grain boundary volume is $\frac{3\Delta a}{d_0}V_{film}-\frac{3\Delta a}{d}V_{film}$. Therefore, the volume strain caused by grain growth is

$$\varepsilon_v=\frac{\frac{3\Delta a}{d_0}V_{film}-\frac{3\Delta a}{d}V_{film}}{V_{film}}=3\Delta a(\frac{1}{d_0}-\frac{1}{d}). \tag{2.9}$$

If the strain caused by grain growth is isotropic, the consequential in-plane stress is

$$\sigma_{gg}=M_f\Delta a(\frac{1}{d_0}-\frac{1}{d}). \tag{2.10}$$

It should be noted that the grain boundaries act as sinks for vacancies and dislocations. During grain growth, excess vacancies and dislocations can be absorbed by the moving grain boundaries. This will lead to an additional tensile stress in the film.

2.1.6 STRESS CAUSED BY SURFACE DEFECTS

The long-range effective interactions between adatoms, ledges and other defects can cause stress in the surface layer. Based on elasticity theory, in an infinite solid, the displacement field ($\vec{u}(\vec{r})$) produced by a point impurity satisfies the basic equation[10]:

$$(\lambda+G)\nabla(\nabla\bullet\vec{u})+G\nabla^2\vec{u}=0. \tag{2.11}$$

Here, G is the shear modulus, given by $G=\frac{E}{2(1+\nu)}$, $\lambda=\frac{E\nu}{(1+\nu)(1-2\nu)}$. An analogy between Equation (2.11) and the Poisson equation of electrostatics [11] suggests the solution should have a form $\vec{u}(\vec{r})=C\frac{\vec{r}}{r^3}$ or in the scalar form, $u(r)=C\frac{1}{r^2}$, where C is a constant. Alternatively, the elastic field of an adatom can be described as a force dipole. Lau and Kohn [12, 13] have shown that the displacement field can be written as

$$u(r)=\frac{1-\nu^2}{\pi E}\frac{A}{r^2}. \tag{2.12}$$

Here A is the magnitude of the force dipole associated with the adatom-surface couple.

Both methods conclude that the magnitude of the displacement field decays with r^{-2}. Further analyses show that the elastic interaction between two identical adatoms is repulsive, and the adatom-adatom interaction is proportional to r^{-3} [10]. Similarly, the interaction between an adatom and a row of adatoms is proportional to r^{-2}, and the interaction between two half-

layers is proportional to $\ln r$. These interactions are also repulsive. Therefore, the adatom-adatom, adatom-ledge and ledge-ledge interactions may cause compressive stress in the surface layer during growth.

2.2 MODELS FOR THE INITIAL COMPRESSIVE STRESS

As shown in Figure 1.6, systems of low atomic mobility develop tensile stress before coalescence, while systems of high atomic mobility often start from an initial compressive stress, followed by development of a tensile stress until the film is fully continuous. It should be noted that in this growth stage, an *in situ* measurement gives the deflection of the cantilever caused by the stress in a discontinuous film. It is thus incorrect to calculate the 'average stress' using Stoney's equation. In this section, we review models for the initial compressive stress. Models for the tensile stress that develops during and after coalescence will be discussed in the next section.

2.2.1 LAPLACE PRESSURE MODEL

As stated in Subsection 2.1.3, the tensile surface stress on a convex curved surface leads to compression in the bulk of the material. It is thus straightforward to link the initial compressive stress in the islands to the Laplace pressure caused by the surface stress. Based on this idea, Laugier[14] presented a qualitative argument for the origin of the precoalescence compressive stress and argued that the equilibrium lattice parameter in the island depends on its size.

Cammarata *et al.* [15] agreed to Laugier's argument and further argued that when the islands grow larger than a critical size, they become firmly attached to the substrate and are unable to change the in-plane lattice spacing during further growth. Subsequent epitaxial growth on these islands leads to a compressive stress before coalescence because of the 'locked-in' lattice spacing.

Assume there is a cylindrical island of the critical size attached on the substrate, with a height of h_0 and a radius of r_0. When this island grows to a height of h and a radius of r, the biaxial stress caused by this mechanism is [15, 16]

$$\sigma = [\frac{(f_1 + f_2)}{h} - \frac{(f_1 + f_2)}{h_0}] + [\frac{1-3\nu}{1-\nu}\frac{f_3}{r} - \frac{1-3\nu}{1-\nu}\frac{f_3}{r_0}], \tag{2.13}$$

where f_1, f_2 and f_3 are the surface stress of the top surface of the cylindrical island, the interface stress and the surface stress associated with the perimeter of the cylindrical island, respectively.

2.2.2 ADATOM-SUBSTRATE INTERACTION MODEL

Friesen *et al.* [17, 18] deposited Cu films on borosilicate glass substrates and studied the stress evolution during growth, interruptions of growth and upon resumption of growth in the precoalescence regime. The initial compressive stress shifts towards the tensile direction during an interruption and back to compressive upon growth resumption (see Figure 2.1). In this stage of growth, the coverage of the film is low. Therefore, the decay of the compressive

stress during growth interruptions is likely associated with island coarsening rather than coalescence, which should occur at a larger film thickness.

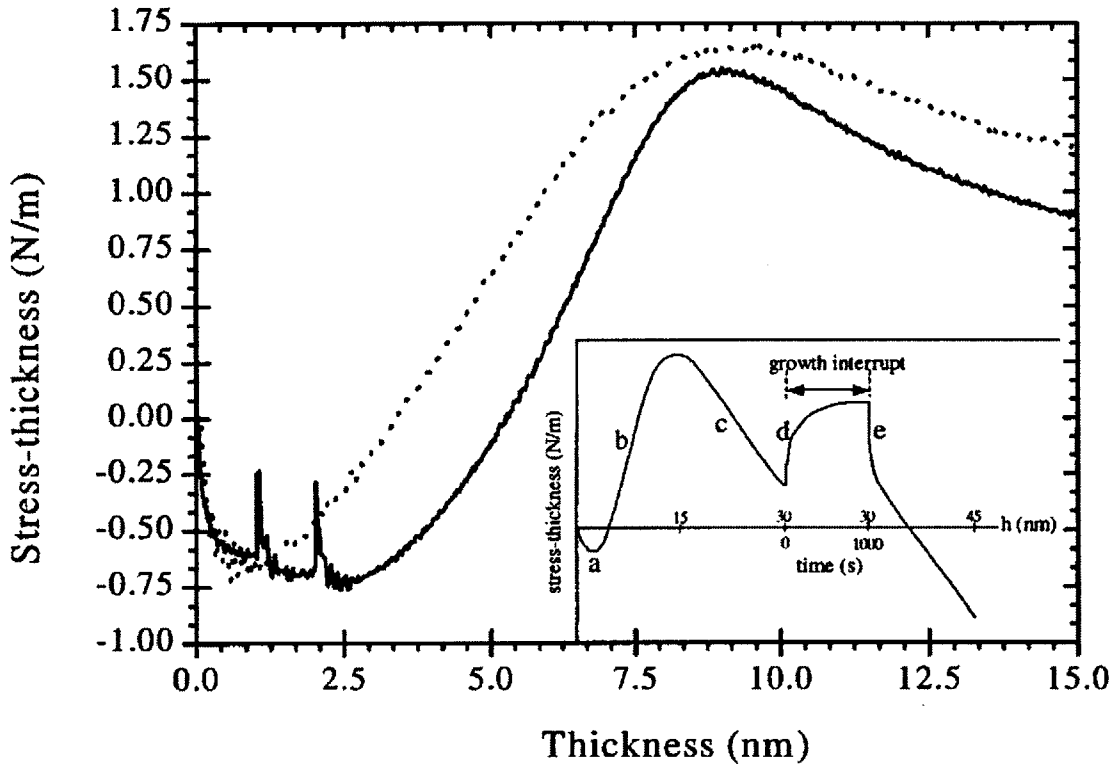

Figure 2.1. Reversible stress in the precoalescence regime of Cu film growth[17].

The instantaneous stress (defined as the slope in the $(\frac{F}{w})$ vs. h plot) observed at the onset of growth is high, on the order of -1GPa. The authors suggested this stress is associated with the effects of adatoms, the concentration of which increases rapidly when the growth is started. During growth, the adatom concentration exceeds the equilibrium concentration and increases more rapidly with increasing deposition rate. As a result, the change of the reversible stress

during a growth interruption should increase with the deposition rate. This trend was observed in experiments on Cu films.

Specifically, the authors suggested that the initial compressive stress originates from the interaction between adatoms and the substrate. As discussed in Subsection 2.1.6, the displacement field of an adatom can be described as a field caused by a force dipole normal to the surface. The parameter A in Equation (2.12) characterizes the energy associated with the adatom-substrate force dipole. If we view the adatoms and the substrate as an ensemble, the surface stress of this ensemble can be written as [18]

$$f(\rho, A, C) = \gamma(\rho, C) + \frac{\partial \gamma}{\partial \varepsilon}(\rho, A). \tag{2.14}$$

Here, ρ is the adatom density and C is the chemical component of the interaction energy that is associated with the modification of the surface energy due to chemical differences between the adatoms and the underlying substrate. If the chemical differences are small, the instantaneous stress can be derived as

$$\frac{\partial f}{\partial h} = \frac{\partial f}{\partial \rho}\frac{\partial \rho}{\partial h} \simeq -A\Omega, \tag{2.15}$$

where Ω is the atomic volume. Based on Equation (2.15), the instantaneous stress can be estimated using the value of the parameter A, which can be calculated using molecular dynamics simulations. The magnitude of the stress measured *in situ* was shown to be comparable to that based on the force-dipole calculation for the Cu-Cu (111) system.

2.3 MODELS FOR THE TENSILE STRESSES DURING AND AFTER COALESCENCE

2.3.1 HOFFMAN-NIX-CLEMENS MODEL

To explain the tensile stress generated during coalescence, Hoffman [19] first proposed a mechanism of grain boundary relaxation. According to his model, when the crystallites are close enough, they snap together to minimize the total energy. Here the surfaces of high energy are converted to the grain boundaries of low energy. Nix and Clemens [20] further developed this idea by analyzing the case of rounded-shaped crystallites, the attractive force between which leads to elastic stretching and grain boundary formation. The stretching is limited by the elastic strain in the film. As a result, grain boundary formation stops near the top region of the crystallites. Known as the 'zipping process', this leads to sharp and crack-like features on the surface of the film (Figure 2.2).

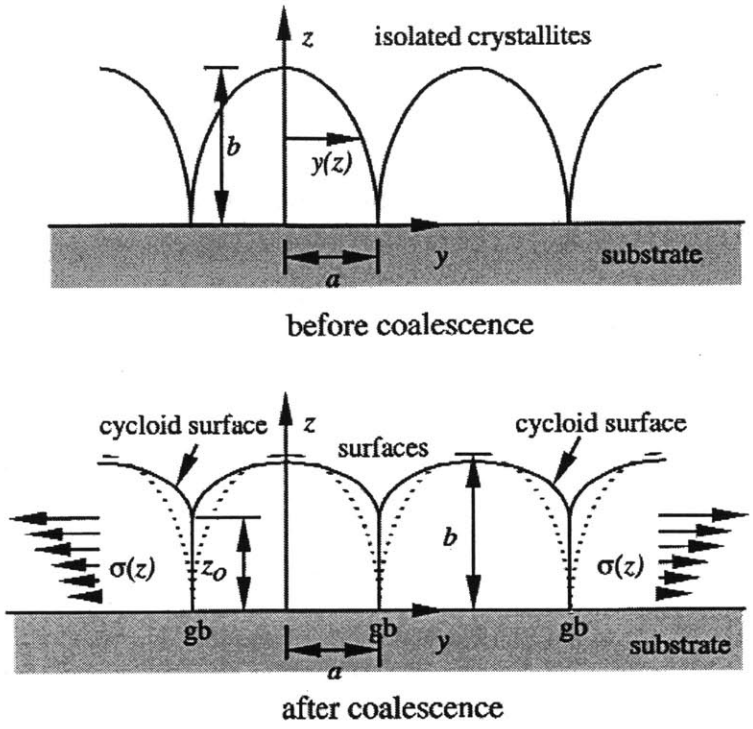

Figure 2.2. Nix and Clemens: Zipping process during crystallite coalescence[20].

Viewed as similar to a reverse crack initiation process, the stress generation during crystallite coalescence can be estimated using the Griffith criteria [21]. Nix and Clemens concluded that the average stress caused by the zipping process is

$$<\sigma>=[(\frac{1+\nu}{1-\nu})E\frac{(2\gamma_s-\gamma_{gb})}{d_{coal}}]^{1/2}. \qquad (2.16)$$

Here γ_s and γ_{gb} are the surface energy and the grain boundary energy, d_{coal} is the coalescence grain size. Using typical parameter values for gold films, the coalescence stress based on

Equation (2.16) is ~2-6GPa, an order of magnitude higher than that determined in *in situ* measurements.

Using the same geometry, Seel [22] calculated the coalescence stress based on global energy minimization. The equilibrium average stress is shown to be

$$<\sigma>=[\frac{1}{9}(\frac{E}{1-\nu^2})\frac{(2\gamma_s-\gamma_{gb})}{d_{coal}}]^{1/2} . \quad (2.17)$$

Compared to the result using Griffith criteria, this method gives a stress magnitude closer to the experimental results. Based on the plane strain model, Seel and Thompson [23] further treated this problem using finite element method (FEM) calculations and obtained a result more consistent with the experiments and Equation 2.17.

The magnitude of the coalescence stress strongly depends on the grain size at coalescence. Generally, it can be written as $<\sigma>\propto(\frac{1}{d_{coal}})^C$. The analytical methods by Hoffman, Nix and Clemens, and Seel all conclude that $C=1/2$. In contrast, Freund and Chason [24] treated this problem using Hertzian contact theory. They concluded that $C=1/2$ for a 1D model, $C=2/3$ for contact between cylindrical islands, and $C=1$ for contact between hemispheres. Moreover, fitting the FEM data of Seel and Thompson [20] for the case of cylindrical islands leads to $C=0.814$. Bhandari, Sheldon and Hearne [25] measured the coalescence stress in Ni films that were electrodeposited on patterned substrates. The initial grain size can be controlled by varying the periodicity of the trenches, to create an experimental analog for the

case of coalescence of cylindrical islands. The log-log plot of the stress as a function of the initial grain size indicates that $C = 0.6$.

2.3.2 POSTCOALESCENCE TENSILE STRESS

For low mobility materials, Nix and Clemens[20] suggested that the epitaxial inheritance of the coalescence stress could lead to a constant tensile stress during film thickening. This is consistent with experimental results in Type I systems. Sheldon *et al.* [26] measured the intrinsic stress in diamond films grown by chemical vapor deposition and found an increase of the average stress during film thickening. Cross sectional SEM images (Figure 2.3) showed that the surface of the diamond film was very rough. The authors argued that the rough surface facilitates grain boundary formation during continuing growth, leading to additional tensile stresses after film coalescence. In other words, rather than zipping between 3D islands, atomic zipping occurs in the surface layer of the film during subsequent thickening.

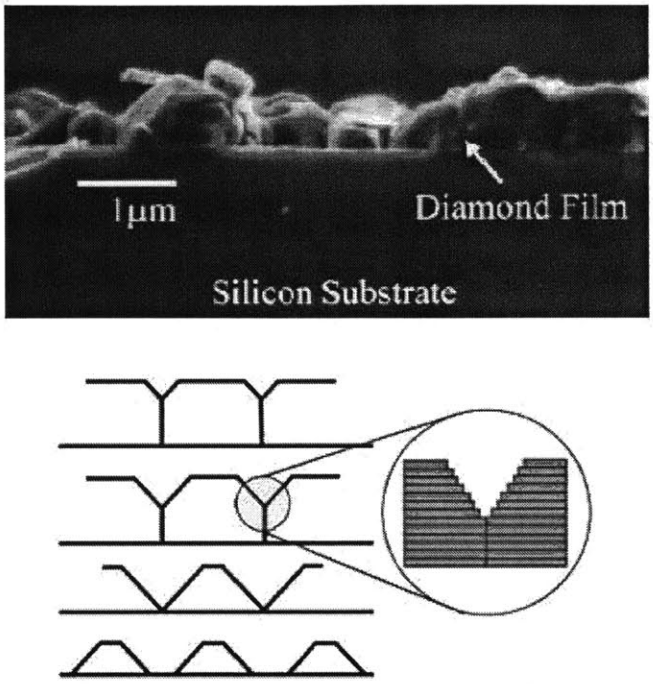

Figure 2.3. Top: a cross-sectional SEM image of a diamond film grown by chemical vapor deposition. Bottom: schematics of the step edge zipping model [26].

Moreover, they proposed a model for materials with faceted grain surfaces, in which atomic zipping occurs when step edges in adjacent grains get close together. This process is caused by a short-range attractive interaction between the steps. According to this model, a steady-state tensile stress is reached when a steady-state surface morphology is achieved. Similar to the coalescence tensile stress, the magnitude of the stress caused by atomic zipping can be calculated using a global energy analysis and should be a function of the grain size during growth.

2.4. MODELS FOR THE REVERSIBLE COMPRESSIVE STRESS AFTER COALESCENCE

At high homologous temperatures, the intrinsic stress turns to become less tensile and then compressive after the film becomes continuous. When the deposition is interrupted, a change of the stress is always seen in the tensile direction. Upon resumption of growth, the stress rapidly returns to the pre-interruption stress evolution trajectory and continues as if the growth had never been interrupted. The underlying mechanisms for this reversible compressive stress have been debated for more than a decade, but no agreement has been reached so far. In this section, a few representative models are reviewed.

2.4.1 SPAEPEN MODEL

Spaepen [27] proposed that the reversible behavior corresponds to trapping and untrapping of excess atoms between surface ledges in the presence and absence of a deposition flux. During growth, numerous surface ledges are formed and the adatoms trapped between coalescing ledges can cause compressive stress. During growth interruptions, the surface becomes flatter by surface diffusion so that the number of the ledges decreases. As a result, the compressive stress is reduced.

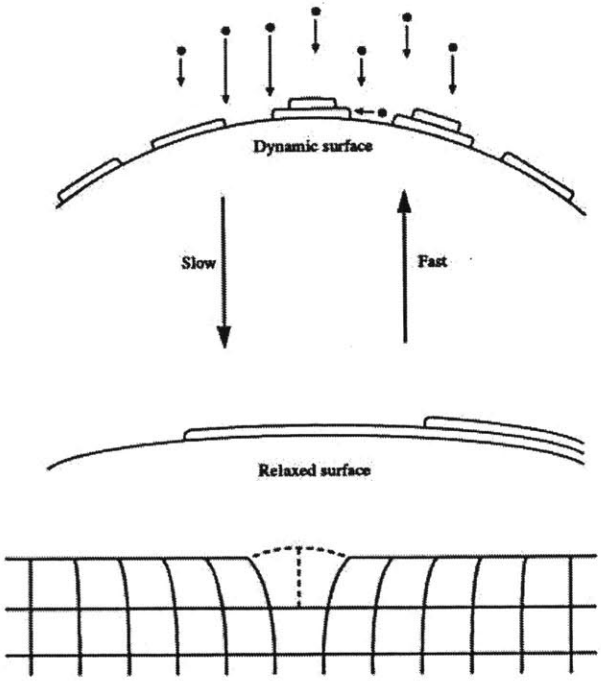

Figure 2.4. Spaepen model: Schematics of a dynamic surface during growth and a relaxed surface during an interruption of growth [27].

The reversibility results from the different stress states of the dynamic and relaxed surfaces. The dynamic surface during growth is associated with nucleation of new layers from the vapor phase, while the relaxed surface during interruptions is associated with the elimination of compressive ledges that requires long-range surface diffusion. The nucleation process is considerably faster than the surface diffusion process. This explains the different time scales of the growth and interruption behaviors observed in *in situ* measurements. The model is illustrated in Figure 2.4.

2.4.2 FRIESEN-THOMPSON MODEL

Friesen and Thompson [17] also attributed the reversible stress to processes on the surface. In analogy their explanation for reversible compressive stresses in the precoalescence and postcoalescence regimes, they proposed that adatom-film interactions are the origin of the compressive stress during film thickening. The observed reversibility can be explained as the reversible change of the adatom population on the surface. In the absence of a deposition flux, the total number of adatoms decreases during growth interruptions. Since the adatom elastic field is compressive for high mobility materials, this results in a decrease of the compressive stress. This model is illustrated in Figure 2.5.

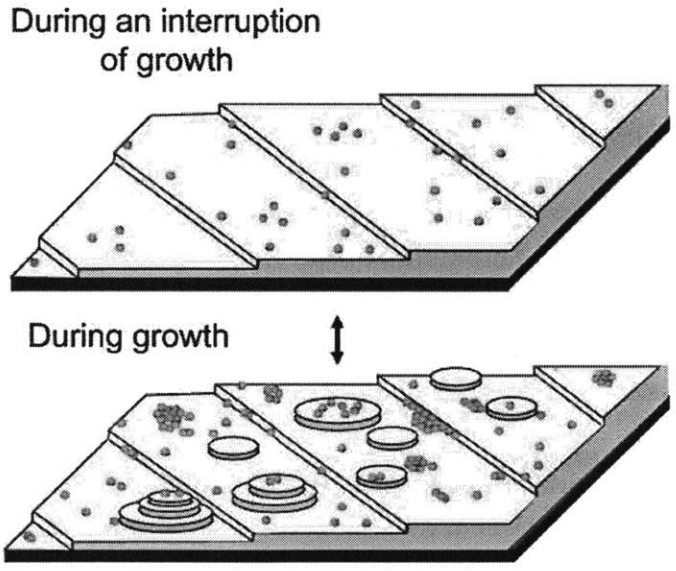

Figure 2.5. Friesen-Thompson model: the reversibility is associated with the change of adatom population during deposition and growth interruptions [28].

2.4.3 MODEL BY CHASON AND COWORKERS

In the discussion of the zipping process, Nix and Clemens[20] suggested that the tensile strain generated during crystallite coalescence could be relaxed by preferential attachment of atoms at the grain boundaries. They argued that the large elastic strains near the grain boundary cusp could distort the ledges at grain boundaries. This provides an atomic mechanism for extra atoms to be incorporated into the grain boundaries (see Figure 2.6). For high mobility materials, diffusion along the growing surface and into grain boundaries is likely to be another mechanism of strain relaxation.

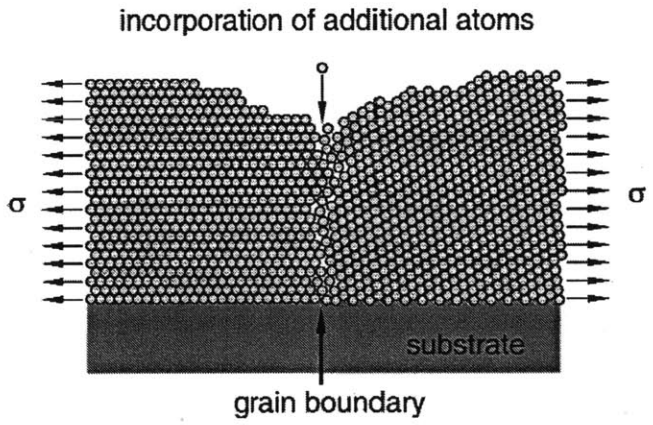

Figure 2.6. Nix and Clemens: preferential attachment of atoms at the grain boundaries [17].

Chason and coworkers [8, 29, 30] also recognized the role of grain boundaries in generating the compressive stress. They proposed that the reversible compressive stress arises from adatom diffusion from the surface to grain boundaries, and that during interruptions of growth,

excess atoms in the grain boundaries are removed by diffusion. This model is illustrated in Figure 2.7. There are three steps in the diffusion of adatoms from the surface to the grain boundary: surface diffusion, the surface-grain boundary transition and grain boundary diffusion. The model assumes that the surface diffusion and the grain boundary diffusion processes are so fast that the whole process is limited by the surface-grain boundary transition step. Based on rate theory, the rate of adatom-grain boundary incorporation can be derived as

$$\frac{\partial N_{gb}}{\partial t} = 2C_s\Gamma[1-e^{-\Delta\mu/k_BT}] \simeq 2C_s\Gamma\frac{\Delta\mu}{k_BT}, \tag{2.18}$$

where N_{gb} is the number of extra atoms added to the grain boundary due to the flux, C_s is the concentration of mobile adatoms on the surface, Γ is a kinetic parameter for the transition rate between the surface and the grain boundary, and $\Delta\mu$ is the difference of the chemical potentials between surface and grain boundary.

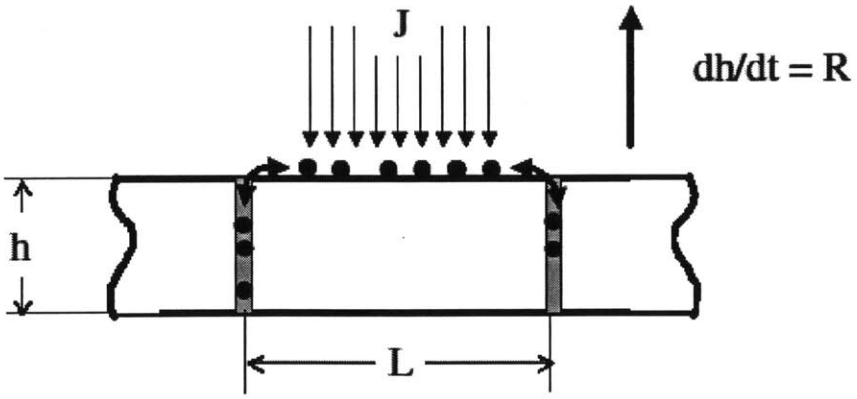

Figure 2.7. Illustration of the model proposed by Chason et al. [6]

They argued that during growth the chemical potential of the surface is higher than that of the grain boundary because of the impinging deposition flux: $\Delta\mu(growth) > 0$. During interruption, the chemical potential of the surface is lower than that of the grain boundary and extra atoms diffuse out of the grain boundary to the surface: $\Delta\mu(\text{interruption}) < 0$. In other words, the reversibility is a result of the change of the chemical potential difference between the grain boundary and the surface.

Based on the model by Nix and Clemens [17], Chason and coworkers assumed a constant tensile stress σ_i caused by grain boundary formation during film thickening. If σ_0 is the compressive stress caused by adding an additional atom to each of the atomic planes in the grain boundary, the average stress in the film is

$$\sigma = \sigma_i - \sigma_0 N_{gb}(\frac{a}{h}), \tag{2.19}$$

where a is the atomic spacing. Equation (2.18) and (2.19) lead to a rate equation for the average stress,

$$\frac{\partial\sigma}{\partial t} = -(\frac{\sigma_0}{h}a)2C_s\Gamma(\frac{\Delta\mu_0 + \delta\mu_s + \sigma\Omega}{k_B T}) + (\sigma_i - \sigma)\frac{R}{h} . \tag{2.20}$$

Here $\Delta\mu_0$ is the chemical potential difference between the surface and grain boundary in the absence of deposition flux, $\delta\mu_s$ is the increase in chemical potential of the surface due to the impinging deposition flux, and R is the deposition rate. Solving Equation (2.20) gives the

steady state compressive stress: $\sigma_{ss} = \sigma_i - \frac{\sigma_i \sigma_0 \Omega + \sigma_0(\Delta\mu_0 + \delta\mu_s)}{Rk_BT / 2aC_s\Gamma + \sigma_0\Omega}$. According to this equation, an increase of R would lead to a smaller compressive stress as long as other parameters stayed constant. This trend is generally found in *in situ* experiments. However, as pointed out by Del Vecchio and Spaepen [31], an increase of the deposition rate could also lead to an increase of the adatom concentration on the surface. As a result, $\delta\mu_s$ increases and the steady state compressive stress does not necessarily decrease.

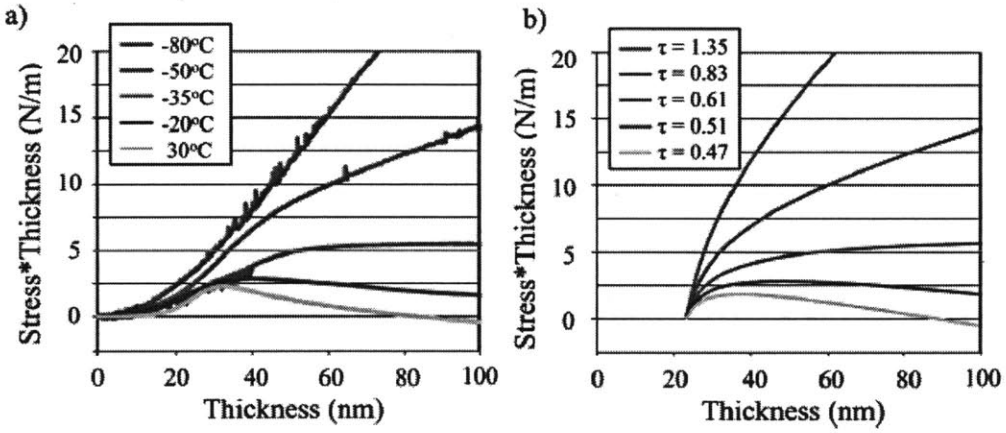

Figure 2.8. Comparison of the experimental data to the modeling results by Chason et al. [30] (a) In situ stress measurements for Ag films deposited at -80,-50,-35,-20 and 30 $^{\circ}C$. (b) Stress curves by modeling with the kinetic parameter τ equal to 1.35, 0.83, 0.61, 0.51 and 0.47.

In a recent paper by Chason and coworkers[30], the modeling result was compared to experimental data for Ag films, see Figure 2.8. Here, the parameter $\tau = \frac{k_B a L}{4 C_s \Omega M_f}(\frac{T}{D})$, where L is the grain size and D is a kinetic parameter describing the hopping rate from the surface to the grain boundary. From the figure, the model best fits the experimental data with $\tau = 1.35, 0.83, 0.61, 0.57, 0.47$ at $T = 193, 223, 238, 253, 303K$, respectively. The effective activation energy for the parameter D can be determined by the plot $\ln(\frac{T}{\tau})$ vs. $(\frac{1}{T})$. I did this calculation and found the effective activation energy to be $\sim 0.07eV$. If the surface-grain boundary transition is the kinetic limiting step, the activation energy of surface diffusion or grain boundary diffusion should be even smaller than $0.07eV$. However, this is generally not the case.

2.4.4 MODEL BY KOCH AND COWORKERS

From a much different point of view, Koch *et al.*[32, 33] suggested that the seeming reversibility of the stress evolution is the result of symmetric but irreversible processes. They argued that some or all of the stress evolution during a growth interruption is associated with recrystallization of the film, citing evidence for recrystallization occurring during growth interruptions. According to this model, at least some component of the stress evolution that occurs during an interruption of growth is linked to an irreversible recrystallization process.

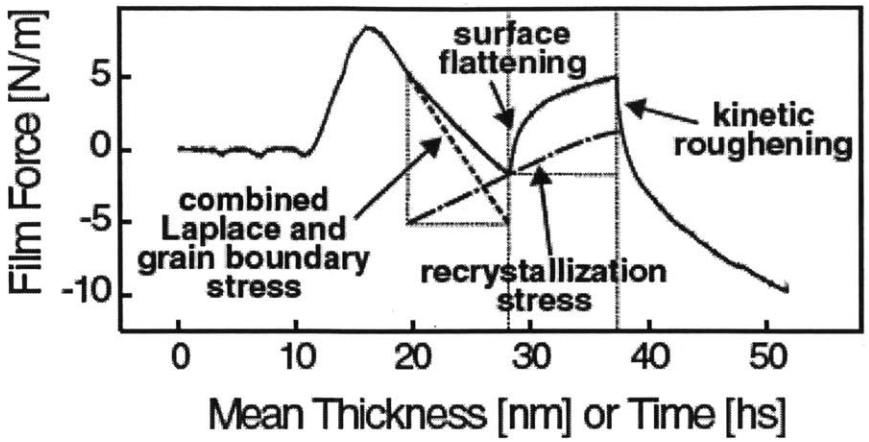

Figure 2.9. The understanding of the stress evolution curve proposed by Koch and coworkers [32, 33].

The authors believed that in the precoalescence stage, the Laplace pressure causes a compressive stress and shrinks the lattice constant. The smaller equilibrium lattice spacing is 'locked in' during coalescence and subsequent thickening. As a result, the central region of the grains is compressively strained while the region near grain boundaries is tensilely strained due to the zipping process.

During an interruption of growth, surface smoothing initiates mass transport from the central region to the region near grain boundaries, so the compressive stress is partially relieved. Moreover, recrystallization occurs as the deposition is stopped, which also leads to a relaxation of the compressive stress (see Figure 2.9). The rough surface morphology is recovered as the deposition resumes. The compressive stress is thus resumed by the preferential attachment of atoms in the central region of the grain surface.

2.4.5 DISCUSSION

The major difference between the surface models [17, 27] and the model by Chason and coworkers [6,26,27] is whether the grain boundary plays an important role in the development of the postcoalescence compressive stress. The latter model is supported by a recent experiment by Leib *et al.* [34], who found that the change of the reversible stress is proportional to the inverse of the grain size. However, when formulating the problem, Chason and coworkers made several unrealistic assumptions. First, to explain the reversible behavior, the model requires the grain boundary diffusivity be comparable to the surface diffusivity. Second, the model assumes the surface diffusion and grain boundary diffusion are much faster than the surface-grain boundary transition. Compared with the experimental data, this indicates that the activation energy for surface diffusion or grain boundary diffusion in Ag films is smaller than $0.07eV$.

The model by Koch and coworkers [29,30] provides new ideas about the stress evolution during an interruption of growth. As pointed out by the authors, the stress during growth interruptions may not originate from a single process. However, it is questionable to argue that the postcoalescence compressive stress originates from the Laplace pressure in the precoalescence regime. First, the initial compressive stress is not always seen in Volmer-Weber films with Type II stress behavior. For example, it was not observed in Ag and Al films grown at room temperature by Floro *et al.* [16]. It was also not observed in Au films deposited on SiNx substrates by Leib *et al.* [34]. However, the postcoalescence compressive stress is observed in all these systems. Second, if the postcoalescence compressive stress were

determined before coalescence, its magnitude would be weakly affected by the subsequent growth conditions. This is contradictory to the experimental observations.

While none of the proposed models is perfect in explaining the reversible compressive stress, they enlighten us about ways of thinking about the problem. For example, future study should take account of the microstructure evolution in the film, because grain boundaries have been shown to be important for the generation of the compressive stress. It is also important to quantify the contributions of the proposed mechanisms so that the dominant mechanism can be identified under certain conditions. This requires detailed characterizations of the grain structure and the surface of the film both during growth and during growth interruptions.

REFERENCES

[1] E. Arzt, G. Dehm, P. Gumbsch, O. Kraft, and D. Weiss, Progress in Materials Science 46, pp. 283 (2001).

[2] M. J. Kobrinsky, and C. V. Thompson, Acta Materialia 48, pp. 625 (2000).

[3] J. Y. Tsao, *Materials fundamentals of molecular beam epitaxy* (Academic Press, Boston, 1993).

[4] R. C. Cammarata, and K. Sieradzki, Annual Review of Materials Science 24, pp. 215 (1994).

[5] R. Shuttleworth, Proceedings of the Physical Society of London Section A 63, pp. 444 (1950).

[6] M. F. Doerner, and W. D. Nix, Crc Critical Reviews in Solid State and Materials Sciences 14, pp. 225 (1988).

[7] M. D. Thouless, Annual Review of Materials Science 25, pp. 69 (1995).

[8] E. Chason, B. W. Sheldon, L. B. Freund, J. A. Floro, and S. J. Hearne, Physical Review Letters 88 (2002).

[9] Chaudhar.P, Journal of Vacuum Science & Technology 9, pp. 520 (1972).

[10] A. Pimpinelli, and J. Villain, *Physics of crystal growth* (Cambridge University Press, Cambridge, U.K. ; New York, 1998), Collection Aléa-Saclay, 4.

[11] J. D. Jackson, *Classical electrodynamics* (Wiley, New York, 1999), 3rd edn.

[12] K. H. Lau, and W. Kohn, Surface Science 65, pp. 607 (1977).

[13] K. H. Lau, and W. Kohn, Surface Science 75, pp. 69 (1978).

[14] M. Laugier, Thin Solid Films 79, pp. 15 (1981).

[15] R. C. Cammarata, T. M. Trimble, and D. J. Srolovitz, Journal of Materials Research 15, pp. 2468 (2000).

[16] J. A. Floro, E. Chason, R. C. Cammarata, and D. J. Srolovitz, Mrs Bulletin 27, pp. 19 (2002).

[17] C. Friesen, and C. V. Thompson, Physical Review Letters 89 (2002).

[18] C. Friesen, S. C. Seel, and C. V. Thompson, Journal of Applied Physics 95, pp. 1011 (2004).

[19] R. W. Hoffman, Thin Solid Films 34, pp. 185 (1976).

[20] W. D. Nix, and B. M. Clemens, Journal of Materials Research 14, pp. 3467 (1999).

[21] M. A. Meyers, K. K. Chawla, and Books24x7 Inc., (Cambridge University Press, Cambridge ; New York, 2009).

[22] S. C. Seel, (Massachusetts Institute of Technology, 2002), p. 2 v. (294 leaves).

[23] S. C. Seel, and C. V. Thompson, Journal of Applied Physics 93, pp. 9038 (2003).

[24] L. B. Freund, and E. Chason, Journal of Applied Physics 89, pp. 4866 (2001).

[25] S. J. Hearne, S. C. Seel, J. A. Floro, C. W. Dyck, W. Fan, and S. R. J. Brueck, Journal of Applied Physics 97 (2005).

[26] B. W. Sheldon, A. Rajamani, A. Bhandari, E. Chason, S. K. Hong, and R. Beresford, Journal of Applied Physics 98 (2005).

[27] F. Spaepen, Acta Materialia 48, pp. 31 (2000).

[28] C. V. Thompson, Leib, J, Yu, H. Z., in *International Symposium on Plasticity*Puerto Vallarta, 2011).

[29] J. S. Tello, A. F. Bower, E. Chason, and B. W. Sheldon, Physical Review Letters 98 (2007).

[30] E. Chason, J. W. Shin, S. J. Hearne, and L. B. Freund, Journal of Applied Physics 111 (2012).

[31] A. L. Del Vecchio, and F. Spaepen, Journal of Applied Physics 101 (2007).

[32] R. Koch, D. Z. Hu, and A. K. Das, Physical Review Letters 95 (2005).

[33] R. Koch, D. Z. Hu, and A. K. Das, Physical Review Letters 94 (2005).

[34] J. Leib, R. Monig, and C. V. Thompson, Physical Review Letters 102 (2009).

CHAPTER 3

EXPERIMENTAL TECHNIQUES AND PROCEDURES

Here we introduce the experimental techniques used in the thesis work. The first half of the chapter is devoted to the deposition technique and the method for *in situ* stress measurement. The features and capabilities of our deposition system are discussed in detail, followed by a discussion of the stress sensor that enables stress measurement for oblique angle deposition. As pointed out in the last section of Chapter 2, characterizations of the surface evolution and grain structure evolution are critical to understand the measured stress curves. Therefore, various characterization methods are discussed in the second half of the chapter, including plan -view and cross-sectional Transmission Electron Microscopy (TEM), Atomic Force Microscopy (AFM) and pole figure measurements using X-ray diffraction (XRD). The chapter is concluded with the procedures for heating and quenching the sample inside the vacuum chamber.

3.1 DEPOSITION TECHNIQUE

Physical vapor deposition (PVD) has been widely used in fundamental research and in the semiconductor industry. As a versatile method, it enables thin film growth for most engineering materials by purely physical processes, e.g. thermal or e-beam evaporation, ion beam sputtering, and laser ablation [1]. One exception is reactive sputtering, e.g. to grow SiO_2, Si_3N_4, in which chemical reactions may happen before the molecules arrive at the substrate. Because of the geometry limitation, a few issues have to be taken into account for

thin film growth by physical vapor deposition, including step coverage, thickness uniformity, and shadowing [1, 2]. However, the effects of these issues are minimal when the sample is small and the distance from the source to the sample is long enough.

Evaporative deposition and sputter deposition and are the most used techniques of physical vapor deposition. Compared to evaporative deposition, sputter deposition is not favored for studying the co-evolution of stress and structure during thin film growth. First, the atom flux of high kinetic energy could increase the effective temperature of the substrate in a poorly understood way. In addition, these atoms could cause shot peening [3], thereby affecting the structure and stress evolution processes. The structure evolution process is also significantly influenced by the presence of impurities. Therefore, a high vacuum condition is desired. Overall, for the purpose of this work, the deposition should be carried out in a high vacuum system using the method of evaporative deposition.

In this work, the deposition and stress measurements were carried out in an Ultra-High Vacuum (UHV) e-beam evaporation system. The system, manufactured by Perkin-Elmer, consists of a load/lock, a chamber for deposition, and three e-guns (from *Thermionics).* The system is pumped down by one *Varian* rotary pump, serving as the roughing pump, and two *CTI* cryopumps. During operation of the cryopumps, the temperature of the cold head is maintained below 15K by liquid helium, which is supplied by a *CTI* compressor that compresses the helium gas of ultra-high purity to form a liquid phase. The water in the chamber is baked out using a transformer controlled high power lamp (100V, 1000W). The base pressure of the Perkin-Elmer system is $\sim 5\times10^{-9} Torr$, monitored by an ion gauge that is interlocked with the switch of the e-beam filament.

The sample is loaded in the load/lock with the chamber gate closed. As a result, the chamber is in an ultra-high vacuum condition all the time. When the load/lock is pumped down to the range of 10^{-6}*Torr* or below, we open the chamber gate and transfer the sample to the chamber using a transfer arm. The sample is then mounted on a stage with heating and cooling capabilities. The height of this stage can be manually controlled. After that, the transfer arm is pulled back to the load/lock and the chamber gate is closed. Finally, the sample is in an ultra-high vacuum condition and the deposition process can be carried out.

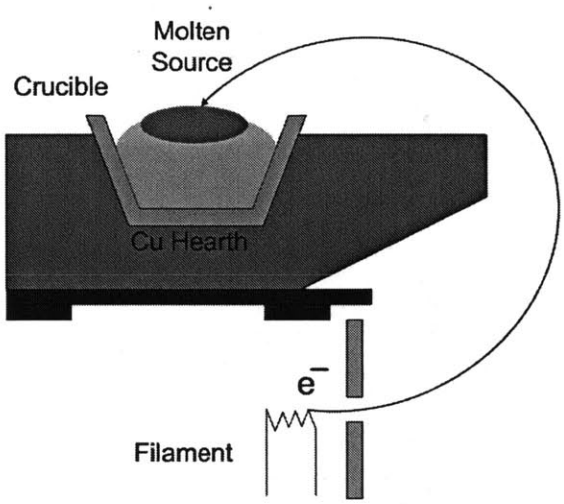

Figure 3.1. Drawing illustrating the principle of e-beam evaporation.

When running an experiment, a 10kV voltage is applied to the tungsten filament in the e-gun. As the filament current increases, electrons start to emit from the filament. Guided by hearth magnets, the emitted electrons travel into the crucible and transfer energy to the source material, eventually making it melt and evaporate (see Figure 3.1). The deposition rate is monitored using a quartz crystal monitor and an *Inficon* rate controller, and is calibrated by

thickness measurements made using an Atomic Force Microscope. Other features of the system include a source and a sample shutter, residual gases analysis and a leak valve on the chamber surface, which allows for *in situ* manipulation of the vacuum condition by flowing extra gases. Figure 3.2 shows a picture of the whole system along with pictures of a few parts of the system.

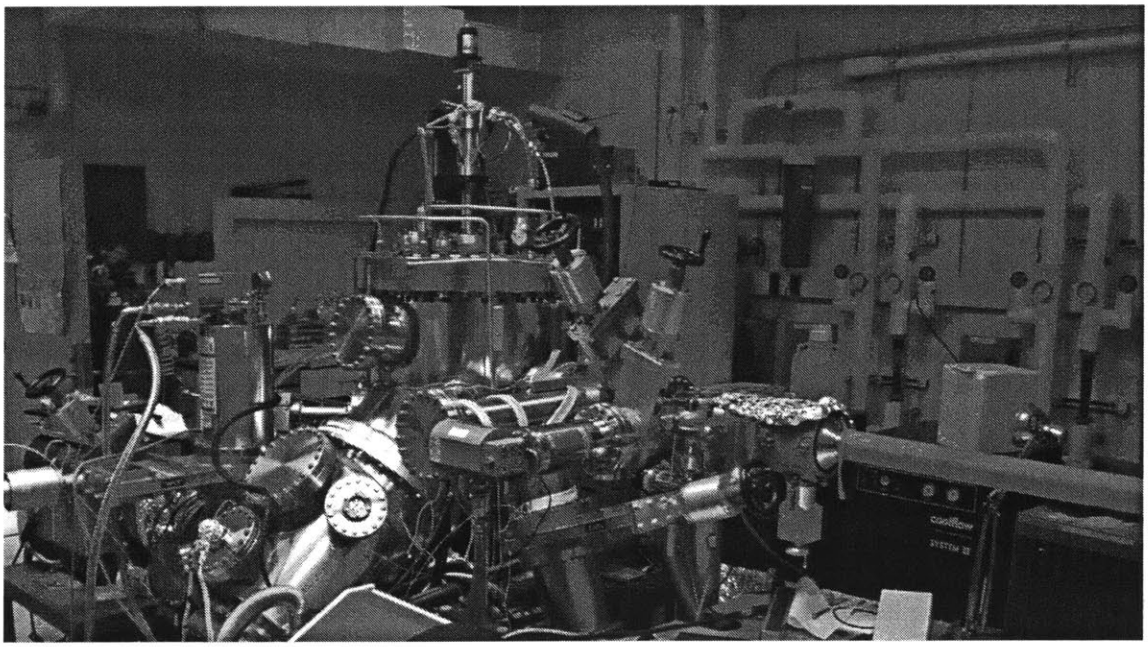

(a)

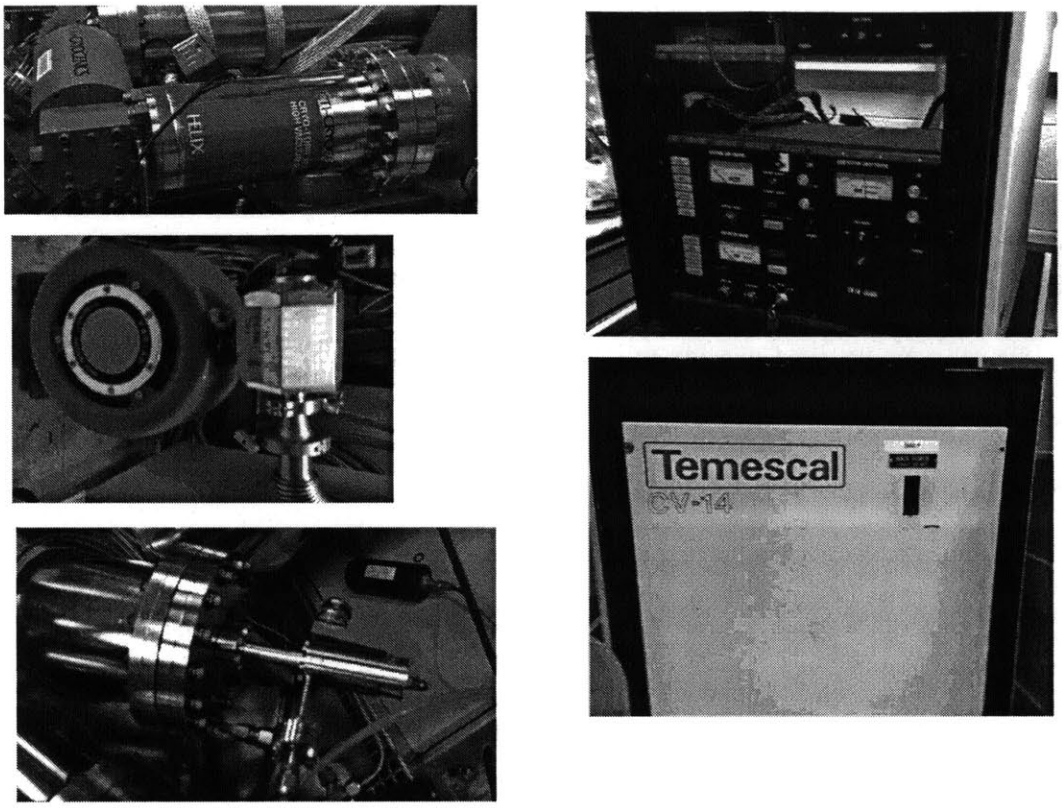

(b)

Figure 3.2 (a) A picture of the Perkin-Elmer system. (b) Left column: the CTI cryopump, the Varian rotary pump and the leak valve. Right Column: Control panel for the high voltage and filament current of the e-beam evaporator, and power supply of the e-beam evaporator.

3.2 *IN SITU* STRESS MEASUREMENT

3.2.1 SENSOR BASED ON CAPACITANCE MEASUREMENT

Various methods for *in situ* stress measurement have been discussed in the introduction chapter. In this work, we use the capacitance-based method. Specifically, we deposit films on a cantilever. The deflection of the cantilever can be determined by measuring the capacitance between it and another electrode. Because here the cantilever serves as an electrode, its backside needs to be conductive. In practice, the cantilever can be made from thin ($\leq 200\mu m$) doped Si wafers or from a piece of thin glass. For the latter case, one side of the glass is coated with a metal film to ensure conductivity. During deposition, films are deposited on the other side of the glass for stress measurements.

For the cantilever configuration, the Stoney Equation [4] is modified as

$$(\frac{F}{w}) = M_s \frac{\delta \times h_s^2}{3l^2}, \tag{3.1}$$

where δ, M_s, l and h_s are the deflection, the biaxial modulus , the thickness and the length of the cantilever, respectively. It should be noted that the validity of this method is not affected when the film undergoes plastic deformation as long as the substrate is bent elastically, because the calculation is based on the properties of the substrate only.

The key component of the sensing system is a Russian-doll like sensor plate (see Figure 3.3). It consists of three stainless steel cylindrical rings surrounded one by one, called sense, guard and ground, respectively. They are all conductive but are electronically isolated from each other by 25μm thick Kapton strips. *In situ* stress measurement is implemented by measuring the capacitance change between the grounded cantilever and the sense electrode in the sensor plate.

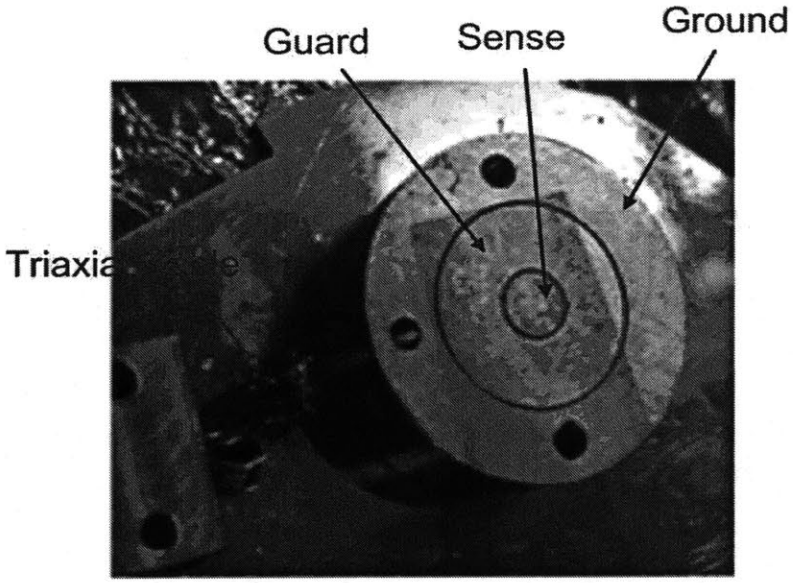

Figure 3.3. A picture of the stress sensor.

Through a triaxal cable inside the vacuum chamber, the sense, guard and ground electrodes are connected to an electrical feedthrough at the vacuum-ambient interface. Outside the vacuum chamber, this electrical feedthrough is connected to an *ADE* electronic system (designed by *ADE Corporation*), which converts the capacitance signal to a voltage signal

recorded by a Labview program. A change of 1V in the voltage signal corresponds to a deflection of $10\mu m$. The spatial and time resolutions for the system are on the order of 10 nm of deflection recorded at $100Hz$. The effective length of the cantilever is the distance between the fixed end of the cantilever and the center of the sense electrode. In our set-up, this length is 0.03425m. The parameters above determine the minimum detectable force per unit width to be $\sim 5\times10^{-3} N/m$. It is important to note that the design of the triaxial shielding effectively eliminates the noise from the e-guns and cryopumps.

3.2.2 TILTABLE PLATFORM

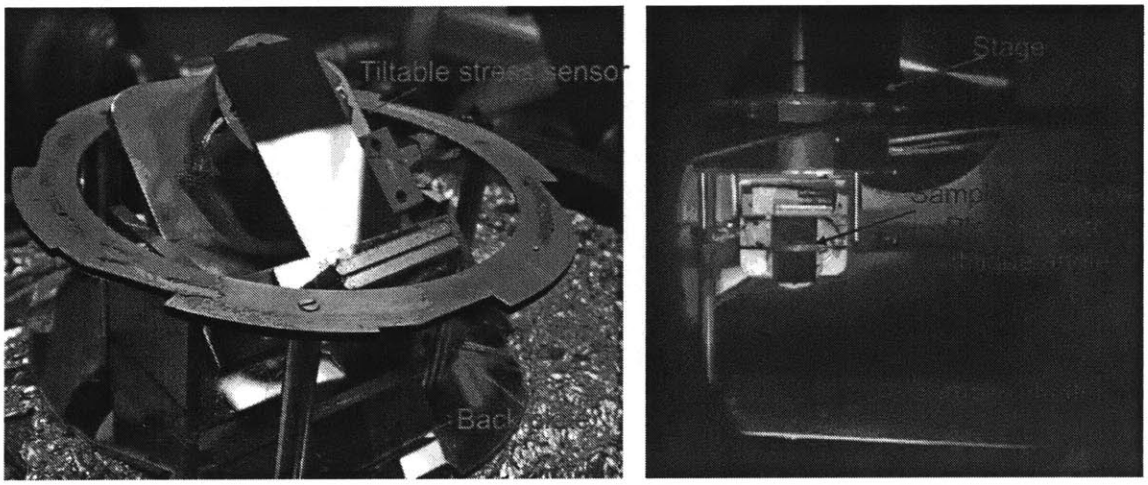

Figure 3.4. Left: sample mounted on the tiltable stress sensor. Right: the whole ensemble in the vacuum chamber.

The angle of the incident evaporant flux would significantly influences the surface morphology and grain structure in polycrystalline films. We therefore expected that the angle

of incidence would affect the intrinsic stress in polycrystalline films. To enable *in situ* stress measurements for deposition at various angles, we designed and fabricated a tiltable stress sensor set-up (shown in Figure 3.4). In this set-up, the sensor plate is mounted on a square plate, the inclination of which can be varied from 0 to 90 degree and locked using a side screw. Geometric limitations of the load/lock was taken into account when designing this tiltable platform. As a result, the effective length of the cantilever was reduced to 0.02925m. All the other parameters of the stress sensor remain unchanged. Stress evolution in Ni and Au films measured using this set-up is discussed in Chapter 6.

3.3 MATERIALS CHARACTERIZATION

3.3.1 MICROSTRUCTURE CHARACTERIZATION

The thickness of the polycrystalline films studied in this work was on the order of 10-100nm. Within this range, the grain size is on the order of 10nm or less. It is thus necessary to use Transmission Electron Microscopy (TEM) to investigate the microstructure evolution during growth and growth interruptions.

TEM imaging is essentially a 2D projection of the sample formed by high-energy electrons that transmit through the sample or are elastically scattered by the sample. The electrons that are inelastically scattered by the sample can result in X-rays, Auger electrons or cathodoluminescence [5], which provide a lot of analytical information. The resolution of a TEM can be very high; it is determined by the wavelength of the electrons, spherical aberration, chromatic aberration and astigmatism [5]. The former two factors dominate in

regular cases, in which the minimum detectable distance in TEM imaging can be approximated as $r_{min} = 0.91[C_{SA}\lambda^3]^{1/4}$, where λ is the wavelength of the electrons and C_{SA} is a parameter for spherical aberration.

The sample for TEM imaging has to be very thin, less than 100nm for most cases. For conventional TEM, the sample has to be vacuum compatible too. Recently, commercialized Environmental Transmission Electron Microscopy has become available for chemical research at the atomic scale. In that case, high-resolution imaging can be done with the gas pressure as high as a few percent of atmospheric pressure [6].

Both the bright field (BF) mode and dark field (DF) mode of TEM imaging have been used in this work. In the bright field mode, only the direct beam is allowed to pass through the objective aperture so that the images result from the interaction of the direct beam with the sample. Consequently, the areas of heavy atoms, high crystallinity and large thickness appear in dark contrast. On the other hand, in the dark field mode the direct beam is blocked by the objective aperture, but the beam scattered in a specific direction is allowed to pass through. By adjusting the sample tilt angle in dark field imaging, grains with specific crystallographic orientations are imaged as bright. This mode of imaging can provide useful information about the microstructure of the sample, such as grain size, twins, planar defects and so on.

As another useful tool in the TEM, electron diffraction patterns give structural details related to the orientation, phase, and defect morphology of the sample. In the Selected Area Diffraction (SAD) mode, such information can be obtained for a specific small region in the sample using the SAD aperture. Figure 3.5 shows examples of a bright field image, a dark

field image and an image of an electron diffraction pattern for a 7nm thick polycrystalline Ni film.

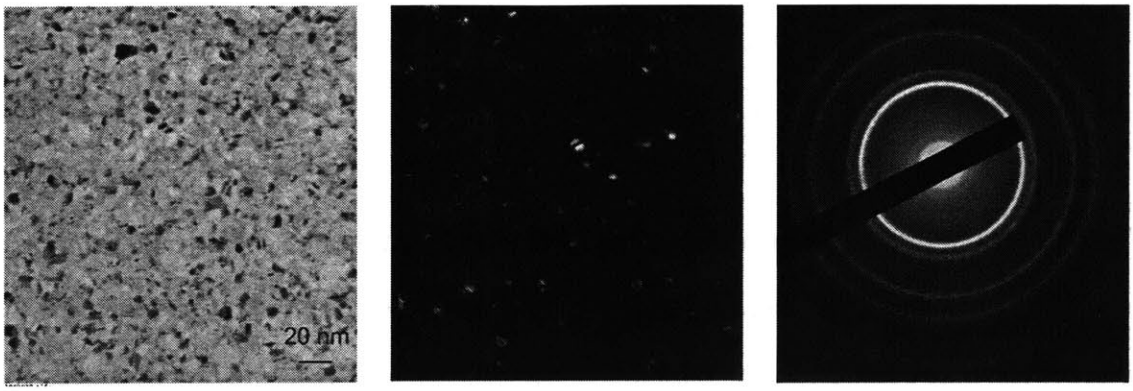

Figure 3.5. TEM characterization of a 7nm thick Ni film. From left to right: a bright field image, a dark field image and an image of an electron diffraction pattern. The scale bar is 20nm.

JEOL 200CX, JEOL 2010, JEOL2011, and JEOL 2010F microscopes were used to perform TEM charcterization in this work. The accelerating voltage is 200KV in all the cases. For plan view TEM, silicon-nitride membrane windows [7] have been used so that no sample thinning is needed after deposition. The membrane is 20nm thick and the window size is $100\mu m \times 100\mu m$. The substrate here is consistent with the one used in stress measurement, in which the cantilever is cleaved from thin silicon wafers coated with 33nm-thick low-stress $SiNi_x$ layers that were grown using low-pressure chemical vapor deposition.

Two methods were used to make cross sectional TEM samples. The first is the traditional mechanical polishing method. The sample is initially cut into two $5mm \times 5mm$ pieces of

rectangular shape. We bond these two pieces with the feature sides facing each other using AB epoxy. Another four pieces of Si substrates of the same size are then used to support the sample pieces. As the glue cures, the whole stack was mounted onto a piece of glass for mechanical polishing using sanding papers of 500, 1200, 4000 grit, followed by a suspension of $0.3\mu m$ alumina powders.

When one side of the stack becomes mirror smooth, we detach it from the glass, flip it over and reattach it on the glass piece. We then polish the other side of the stack and thin the sample to less than $50\mu m$ thick. The thickness of the stack can be monitored using an optical microscope. When the silicon looks red due to transmission of light, we glue the TEM copper grid on to the stack and place the whole ensemble in Acetone to dissolve the wax and remove the glass piece. After that, the sample is ready for ion milling, during which the energy of the argon ions is ~3-5keV, the ion current is ~15-30nA, and the angle of the ion beam is kept less than 10 degree. Finally, a hole can be formed in the center of the sample. The region near the hole is electron transparent and ready for TEM imaging.

The second method used to make cross sectional TEM samples is to use a Focused Ion Beam (FIB). An *FEI* Helios dual beam (FIB/SEM) instrument has been used in this study. During operation, the voltage of the Ga ion is kept at 30KV. We first deposit a platinum protection layer of $\sim 3-5\mu m$ thick onto the interested region before milling trenches on two sides of the platinum layer to make an H-bar. The angle of the ion beam is $52°$ and the ion current is ~2.8nA. After cutting the bottom and the left side of the bar, we insert the manipulation probe until it approaches the Pt layer. We then weld the probe with the protection layer and do

the final cut so that the lamella beneath the protection layer is detached from the whole sample. After that, we lift out the probe and weld the lamella on to a TEM half grid. Finally, the lamella is thinned to less than 100nm using an ion current of ~95pA. The procedures of this method are shown in Figure 3.6.

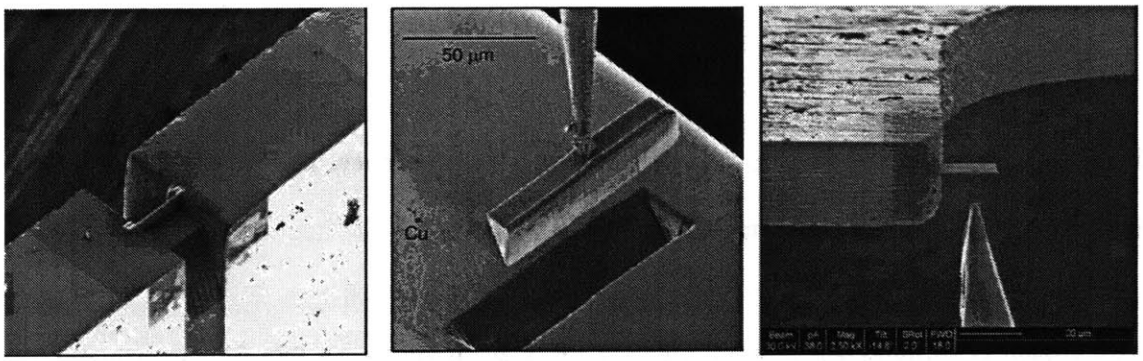

Figure 3.6. SEM images of the steps of TEM sample preparation using an FIB. From left to right: formation of the H-bar, lift-out process, and transfer of the lamella onto the TEM grid [8].

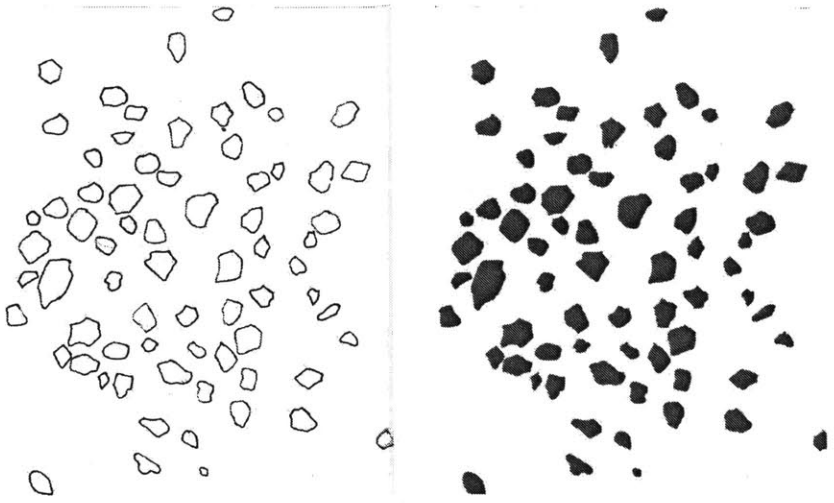

Figure 3.7. Left: an image of grains traced on a transparency. Right: the resultant binary image processed using ImageJ.

Grain growth is an important process affecting stress evolution during thin film growth and growth interruptions. Therefore, it is critical to determine the average grain size and grain size distribution in the films based on TEM imaging. One commonly used method is the Line-intercept method [9], in which the average grain size is estimated by counting the number of the grains intercepted by a straight line. For statistical reasons, the line has to be sufficiently long to yield at least 50 intercepts. Alternatively, the average area of each grain can be estimated by counting the number of grains in a known area. This is often called the planimetric method. These two methods only give the average value of the grain size, but do not provide any information about the distribution of the grain size. To determine the average grain size and the grain size distribution in a polycrystalline film, we can trace the boundaries of grains using transparencies on top of TEM micrographs. In this work, both bright field and dark field TEM images have been used for grain boundary location determination. The traces

on the transparencies are scanned into computer and analyzed using *ImageJ* software. For each sample, hundreds of grains are measured in multiple micrographs. Figure 3.7 shows illustrational images of a 20nm Ni film obtained using this method.

3.3.2 SURFACE TOPOGRAPHY CHARACTERIZATION

We postulated that stress evolution correlated with an evolution of the surface topography of polycrystalline films. To investigate this, we used a Veeco Nanoscope IV AFM for characterization. The microscope is operated in tapping mode, in which the cantilever is driven to oscillate up and down near its resonance frequency. The amplitude of this oscillation decreases when the tip gets closer to the sample surface because of the interaction forces between the cantilever and the sample surface. These interaction forces include Van der Waals forces, electrostatic forces, and so on [10]. When scanning over the sample surface, a piezoelectric actuator is used to adjust the height of the AFM probe so that the oscillation amplitude is maintained to a constant level. For a homogeneous sample surface, the electrical signals are directly related to the topographic information. Because metal films are stiff (e.g., compared to polymers), the AFM probe used in our experiments is the RTESP type, with a spring constant of ~40N/m and a resonant frequency of ~300kHz. The length and width of the cantilever are $125\mu m$ and $35\mu m$, respectively. The tip height is $20\mu m$ and the tip radius is 8nm. In our study, the surface domain of the polycrystalline films is quite small, <50nm. Therefore, the scan area is limited to $0.5\mu m \times 0.5\mu m$ or $1\mu m \times 1\mu m$.

Root mean square (RMS) roughness is the most widely used parameter for surface characterization. It gives an overall estimation of the surface roughness:

$$S_q = \sqrt{\frac{1}{MN}\sum_{j=1}^{M}\sum_{i=1}^{N} z^2(x_i, y_j)}\,. \tag{3.2}$$

Here, M is the number of points per scan line and N is the number of scan lines. $z(x_i, y_j)$ is the height of the (x_i, y_j) point. Another important parameter is the Power Spectral Density (PSD), which characterizes the spatial frequencies of the roughness on a surface. The 2D PSD function can be written in terms of the Fourier transform of the autocorrelation function [11]:

$$W(K_x, K_y) = \frac{1}{4\pi}\iint G(\tau_x, \tau_y) e^{-i(K_x\tau_x + K_y\tau_y)} d\tau_x d\tau_y, \tag{3.3}$$

where the autocorrelation function is defined as

$$G(m,n) = \frac{1}{(N-n)(M-m)}\sum_{l=1}^{N-n}\sum_{k=1}^{M-m} z_{k+m,l+n} z_{k,l}\,. \tag{3.4}$$

Here $\tau_x = x_1 - x_2$, $\tau_y = y_1 - y_2$ and $m = \tau_x / \Delta x, n = \tau_y / \Delta y$. Other useful parameters characterizing surface roughness include 1D and radial power spectral density function (1D and radial PSDF), the radial autocorrelation function (radial ACF), the height-height correlation function (HHCF) and Minkowski Functionals (volume, surface and connectivity). All these parameters effectively describe the overall roughness of the whole surface. However, the topographic information at the local scale has been lost.

The topography at the local scale can be characterized using the inclination angle θ, which is defined as the angle between the normal of a local surface and the normal of the horizontal surface (see Figure 3.8(a)). In an AFM image, the inclination angle of a local plane can be

measured by fitting the local plane through the neighborhood of each point and using its gradient. We can define the region that has an inclination angle θ smaller than the threshold angle θ^* as the smooth region. By marking the smooth region in color, local topographic information can be visualized in the modified AFM images.

The overall steepness of the surface can be described using a plot of the inclination angle distribution. Here the horizontal axis is the inclination angle and the vertical axis is the area fraction, or the probability, of a region having that angle. As examples, Figure 3.8 (b) and (c) show an AFM image of 115nm gold films and a modified image in which the region with an inclination angle $<10^{\circ}$ has been colored in green. Also shown is the inclination angle distribution of the surface (see Figure 3.8 (d)).

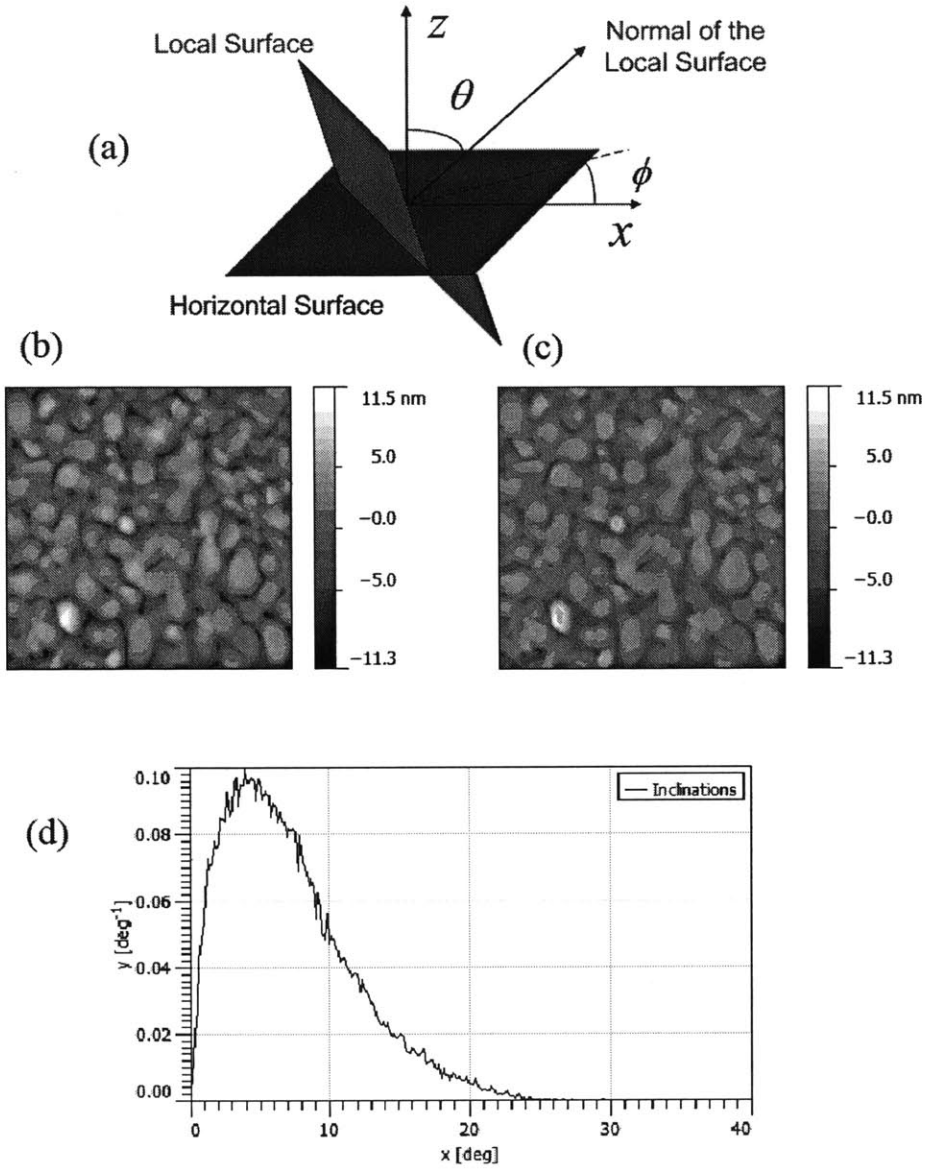

Figure 3.8. (a) Illustration of the inclination angle concept. (b) and (c): An AFM image and a modified AFM image of 115nm-thick gold films. Image size: $1\mu m \times 1\mu m$. (d) Plot of the inclination angle distribution of the film surface.

3.3.3 TEXTURE CHARACTERIZATION

Using X-ray diffraction (XRD), crystallographic orientation information of a crystalline material can be obtained by measuring the angle and intensity of the diffracted X-ray beams. The Bragg Diffraction Equation states that $2d\sin\theta = n\lambda$, where d is the distance between atomic planes, λ is the X-ray wavelength, n is an integer, and θ describes the relative positions of the source and detector (see Figure 3.9(a)). The X-ray is usually generated from an X-ray tube, in which the cathode electrons collide with the target anode and a beam of characteristic wavelength is produced due to the photoelectric effect. Consequently, the wavelength of X-ray is a characteristic of the anode material.

In polycrystalline films, a certain crystallographic direction may be preferentially oriented with respect to the normal to the substrate surfaces. This anisotropy of crystallite orientation is called texture. To understand the co-evolution of the structure and stress in polycrystalline films, it is useful to characterize the texture evolution during growth and during growth interruptions. The texture of a film is best characterized using pole figures, which display the orientation distribution of a specific atomic plane in the material. To fully understand the texture of a polycrystalline film, at least two pole figures are needed.

In this work, we perform the pole figure measurement using a *Bruker D8* diffractometer with a 2D area detector (GADDS). Here the X-ray is produced by a Cu $K\alpha$ source with a wavelength of 1.54Å. The size of the spot collimator we use is 0.3mm. The sample is mounted onto a goniometer system so that it can rotate along multiple axes, as shown schematically in Figure 3.9 (a).

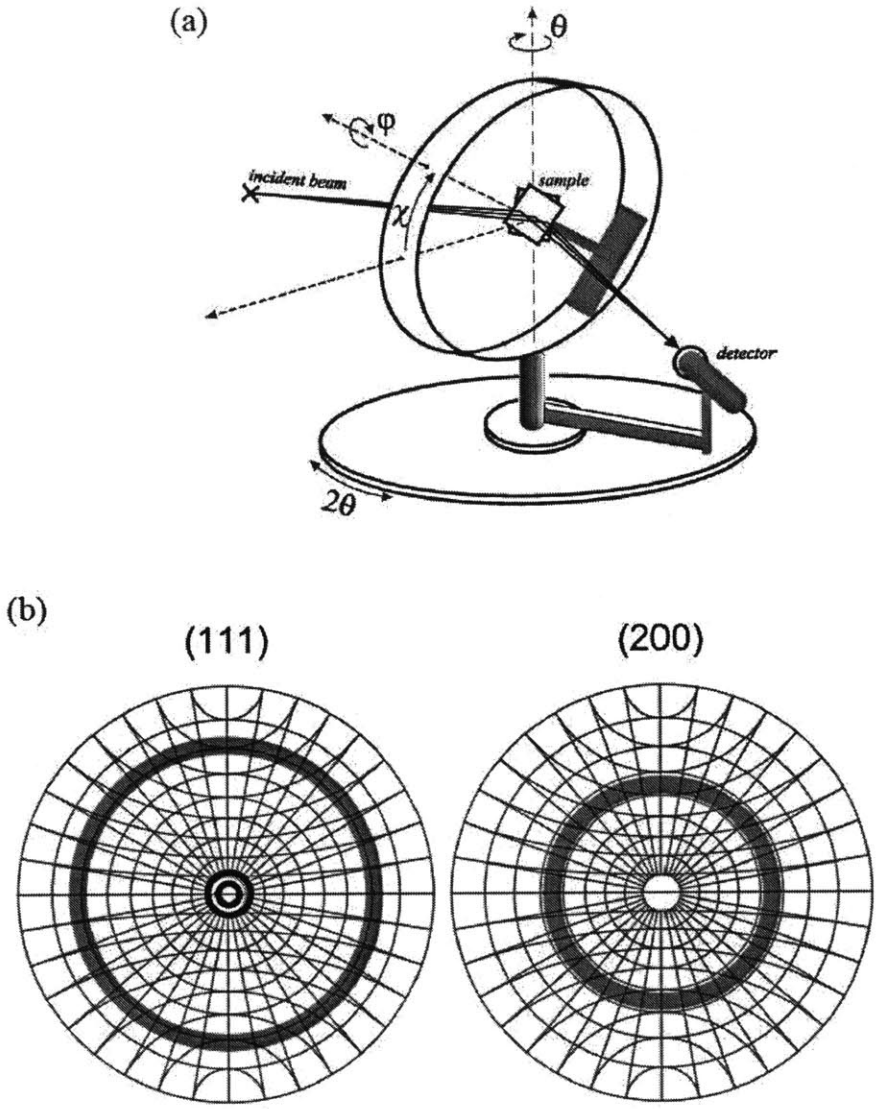

Figure 3.9. (a) Geometry of the goniometer system[12]. (b) (111) and (200) pole figures of a film with ideal (111) fiber texture [13].

During measurement, the incident beam and the 2D detector are positioned at 2θ, corresponding to the (hkl) diffraction peak of the material for $2d_{hkl}\sin\theta = n\lambda$. Therefore, this measurement gives the orientation distribution of the (hkl) plane in the films. The sample rotates along the φ and χ directions, in which both angles are measured with a step of $5°$. At each step, one data frame of the diffracted intensity is collected. With the frames collected at all the steps, a pole figure can be finally generated and analyzed using *MulTex* software. Other details of such pole figure measurements can be found in reference 13.

In this study, the texture of Ni and Au films has been investigated using (111) and (200) pole figures. In Au, the (111) peak is at $2\theta = 38.2°$, and the (200) peak is at $2\theta = 44.4°$. In Ni, the (111) peak is at $2\theta = 44.5°$, and the (200) peak is at $2\theta = 51.9°$. As mentioned in Chapter 1, FCC polycrystalline films often develop (111) texture during growth. Figure 3.9 (b) shows the (111) and (200) pole figures obtained from a film with an ideal (111) fiber texture.

3.4 TEMPERATURE CONTROL

Temperature is one of the most important parameters in the co-evolution of structure and stress in polycrystalline films. In our experiments, a thermocouple and a temperature controller are used to monitor and control the temperature of the sample stage. The sample plate is mounted on the stage with three copper hooks. As a result, there is a very small gap between the sample plate and the stage. To ensure that the sample and the stage are at the same temperature, we monitor the deflection of the cantilever caused by the thermal expansion of the sensor and the cantilever during heating. When the deflection does not change with time, the sample can be considered to be in thermal equilibrium with the stage.

Empirically, we wait for another three hours to do the deposition and stress measurement after the stage has reached the target temperature. Because the Kapton used in the stress sensor has a low melting point, the maximum temperature of the substrate is limited to 573K.

When high temperature deposition is finished, the sample can be cooled down using cooling water. The cooling water line is very thin (1/8" in diameter) and is not fully in contact with the bottom side of the stage, on which the sample plate is mounted. Considering the gap between the stage and sample plate, therefore, the cooling water is insufficient to cool the sample to room temperature in a short time. However, when studying the surface evolution during a growth interruption, it is desirable to quench the sample surface so that the surface structure at elevated temperatures can be recorded as a function of the interruption time (see Chapter 4).

To solve this problem, we have installed a nozzle close to the sample stage and used cold nitrogen gas to cool the sample surface. Inside the vacuum chamber, the nozzle is connected via a feedthrough to the leak valve. Outside the vacuum chamber, the leak value is connected to a tank of cold nitrogen gas. By doing this, the temperature of the stage can be cooled down at a cooling rate of $15°C/\min$. The actual cooling rate of the sample surface should be even higher. However, this method destroys the vacuum and the system has to be pumped down again after each experiment. To protect the e-gun and the cryopump, a standard operation procedure has been developed for this case:

(1) When the deposition is finished, close the sample shutter, close the source shutter and turn off the heater.

(2) Drop the filament current to zero. Turn off the high voltage, the filament current, and the power to the e-beam gun.

(3) Close the cryogate located between the cryopump and the chamber. Open the chamber gate so that the load/lock and chamber are connected. Turn off the Ion gauge.

(4) Lower the sample stage to ~2.5"so that the nozzle is in the closet position relative to the sample. Open the valve of the cold nitrogen tank. Open the leak value. Use a lamp to monitor the things going on inside the chamber. Monitor the change of the stage temperature.

(5) After a few minutes, the top cover of the load/lock should pop up and the whole chamber is exposed to the atmosphere. When the stage temperature drops to $50°C$ or below, unmount the sample from the stage and transfer it back to the load/lock. Doing this at a higher temperature may damage the rotation system of the stage. The sample is now ready for immediate surface and grain structure characterization.

So far, we have discussed the experimental techniques and procedures used in this thesis work, including the deposition technique, *in situ* stress measurement, characterization methods and control of the sample temperature. Combing these experimental methods with analytical modeling, we will investigate the mechanisms of stress evolution during and after polycrystalline film growth in the following chapters.

REFERENCES

[1] D. M. Mattox, *Handbook of physical vapor deposition (PVD) processing* (William Andrew, Oxford, UK, 2010), 2nd edn.

[2] J. D. Plummer, M. D. Deal, and P. B. Griffin, *Silicon VLSI technology : fundamentals, practice, and modeling* (Prentice Hall, Upper Saddle River, NJ, 2000), Prentice Hall electronics and VLSI series.

[3] M. Ohring, *The materials science of thin films* (Academic Press, Boston, 1992).

[4] G. G. Stoney, Proceedings of the Royal Society of London Series a-Containing Papers of a Mathematical and Physical Character 82, pp. 172 (1909).

[5] D. B. Williams, and C. B. Carter, *Transmission electron microscopy : a textbook for materials science* (Springer, New York ; London, 2008), 2nd edn.

[6] R. Sharma, Journal of Materials Research 20, pp. 1695 (2005).

[7] R. Dannenberg, E. A. Stach, J. R. Groza, and B. J. Dresser, Thin Solid Films 370, pp. 54 (2000).

[8] J. Mayer, L. A. Giannuzzi, T. Kamino, and J. Michael, Mrs Bulletin 32, pp. 400 (2007).

[9] J. C. Wurst, and J. A. Nelson, Journal of the American Ceramic Society 55, pp. 109 (1972).

[10] D. Sarid, *Scanning force microscopy : with applications to electric, magnetic, and atomic forces* (Oxford University Press, New York, 1994), Rev. edn., Oxford series in optical and imaging sciences, 5.

[11] D. Necas, and P. Klapetek, Central European Journal of Physics 10, pp. 181 (2012).

[12] J. T. Bonarski, Progress in Materials Science 51, pp. 61 (2006).

[13] A. L. Giermann, (Massachusetts Institute of Technology, 2009), p. 190 p.

CHAPTER 4

FAST AND SLOW PROCESSES DURING INTERRUPTIONS OF POLYCRYSTALLINE FILM GROWTH

4.1 INTRODUCTION

After deposition, thin films can be in a residual state of highly tensile or compressive mechanical stress, depending on the material, film thickness, deposition technique, and deposition conditions[1]. Control of the evolution of residual stresses in thin films and patterned nanostructures is critical in many important applications, including micro-and nano-electromechanical devices and systems[2-4], energy harvesting and storage devices [5], and devices operated at elevated temperatures or in harsh environments [6, 7].

As introduced in Chapter 1, most polycrystalline and many epitaxial films form through the Volmer-Weber mechanism, in which individual single-crystal islands nucleate on the substrate and grow to impinge on other islands before coalescing to form a continuous film. Island coalescence and grain boundary formation [8] lead to the development of a tensile stress. Under conditions of high atomic mobility, a compressive stress develops after coalescence during continued deposition [9, 10]. When the growth is stopped, a change in the stress is always observed in the tensile direction. Intriguingly, upon resumption of growth, the

stress rapidly returns to the pre-interruption stress evolution trajectory and continues as if the growth had never been interrupted. This is the so-called reversible stress [11, 12].

The underlying mechanism for stress evolution during growth interruptions has been debated for more than a decade [10-16]. Several proposed models have been reviewed in detail in Chapter 2. Spaepen [11] proposed that the reversible behavior corresponds to trapping and untrapping of excess atoms between surface ledges in the presence and absence of a deposition flux. Friesen and Thompson [12] further attributed the reversible stress to changes in the adatom population. Chason and coworkers [13-14] recognized the role of grain boundaries and proposed that the compressive stress arises from adatom diffusion from the surface to grain boundaries, and that during interruptions of growth, excess atoms in the grain boundaries are removed by diffusion. Most recently, Koch *et al.* [15-16] argued that some or all of the stress evolution during a growth interruption is associated with recrystallization of the film, citing evidence for recrystallization during growth interruptions. According to this model, at least some component of the stress evolution that occurs during an interruption of growth is linked to an irreversible recrystallization process.

In this chapter, we address this problem by investigating the interruption process at different time scales, at different substrate temperatures and for different film thicknesses. Our experimental observations indicate the existence of multiple stress evolution mechanisms during growth interruptions, distinguished by different time constants, thickness dependencies, temperature dependencies and reversibility. We model these mechanisms as a fast reversible process occurring on the surface plus a slow irreversible process occurring in the bulk of the film. These results are presented in Section 4.2. We discuss the correlation between the slow

process and the microstructure evolution in thin films in Section 4.3. Here characterization of grain structure evolution during growth interruptions confirms the observation of Koch *et al.* [15-16], but the observed time dependence and magnitude of the associated stress change suggest that grain growth contributes to the slow nonreversible stress evolution. In Section 4.4, we propose and show evidence that the fast reversible process is associated with a change of the shape of grain surfaces. The key findings in this chapter are summarized in Section 4.5.

4.2 THE FAST REVERSIBLE PROCESS AND THE SLOW IRREVERSIBLE PROCESS

4.2.1 REVERSIBILITY

Previous research on the reversible stress has focused on the stress behavior during and after a very short interruption (e.g. a few minutes). To gain a comprehensive understanding of the stress evolution process during a growth interruption, it is necessary to extend studies to long-time interruptions. Figure 4.1 and 4.2 show typical stress curves during both short and long-term interruptions of deposition of polycrystalline gold films. The films were deposited at 300K, with a deposition rate of 0.5Å/s. In Figure 4.1, the stress is seen to rise during a 5min interruption and is almost fully recovered upon resumption of growth. This reversible behavior is repeated during subsequent short interruptions of deposition.

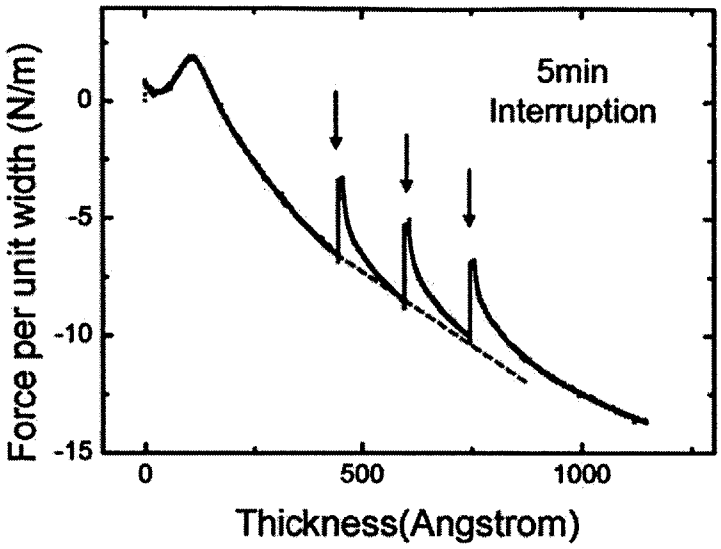

Figure 4.1. Reversible stress evolution in polycrystalline gold films: 300-second interruptions.

For 24-hour interruptions (Figure 4.2), however, a significant amount of the stress change is not recovered after the growth is resumed for several hundred seconds. In addition, the stress trajectory after growth resumption is different from the trajectory before the interruption. These observations indicate the involvement of an irreversible evolution process during the long interruption. The results in Figure 4.1 and 4.2 indicate that multiple stress evolution mechanisms are involved during long growth interruptions. While a reversible mechanism dominates in the short term, an irreversible mechanism has to be taken into account in the long term.

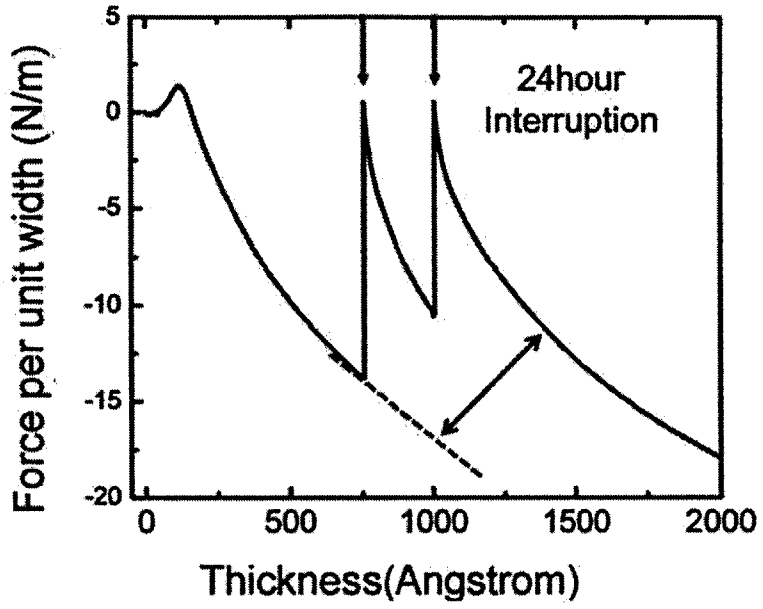

Figure 4.2. Stress evolution during long growth interruptions of polycrystalline gold films.

4.2.2 THICKNESS DEPENDENCE

The thickness dependence of stress evolution during long interruptions of gold is shown in Figure 4.3. For each film thickness, a rapid rise is seen during the first several hundred seconds, followed by a slow evolution that is also in the tensile direction. Two important features should be noted. The first is that the long-term change of force per unit width increases substantially with film thickness, suggesting an important role for a stress evolution process in the bulk of the film. The second feature is that the curves in Figure 4.3 do not have shapes that are consistent with a simple single exponential decay. Instead, these data can be well fit to a double exponential decay function:

$$y = y_0 - y_1 e^{-t/\tau_1} - y_2 e^{-t/\tau_2} \tag{4.1}$$

where τ_1 and τ_2 are the time constants, and y_1 and y_2 are the decay pre-factors of the two processes.

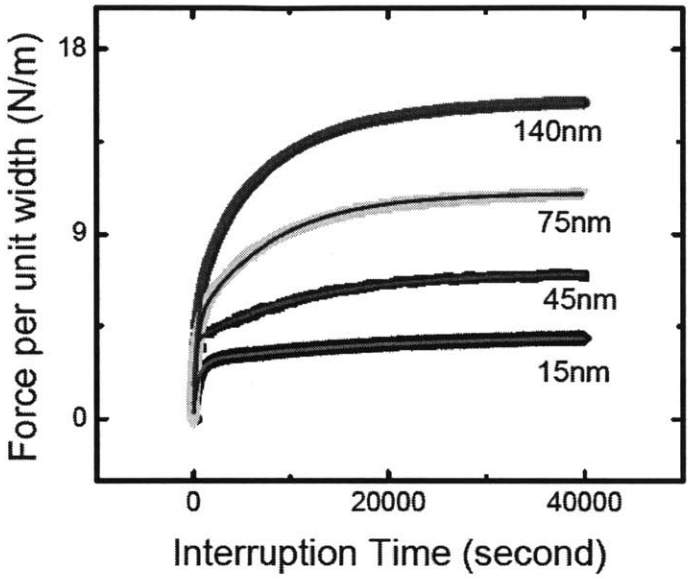

Figure 4.3. Thickness dependence of stress evolution during growth interruptions of gold films.

The thickness dependences of the time constants τ_1 and τ_2 as well as the decay pre-factors y_1 and y_2, are plotted in Figure 4.4(a) and (b). For all the film thicknesses, the time constant for the fast process τ_1 ranges from 150 to 700 seconds, while for the slow process τ_2 ranges from 7000 to 11000 seconds. The decay pre-factor of the fast process y_1 increases slightly in thicker films but is generally weakly dependent on the film thickness. In contrast, the decay

pre-factor of the slow process y_2 is strongly dependent on the film thickness, with a roughly linear dependence.

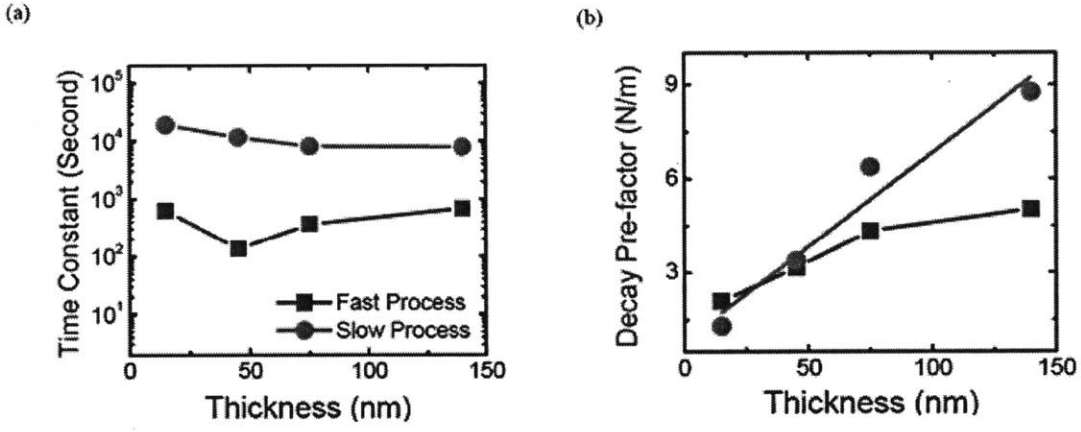

Figure 4.4. The thickness dependencies of the time constant and the decay pre-factor of gold films.

We can interpret the total change of force per unit width as a sum of the change associated with the surface and bulk of the film [11]: $\Delta(\frac{F}{w}) = \Delta S + H_f \Delta\sigma$. Here ΔS is the change of force per unit width associated with the surface, $\Delta\sigma$ is the change of the bulk stress, and H_f is the film thickness. The results in Figure 4.4(b) thus imply that the fast process occurs on the film surface and the slow process occurs in the bulk of the film.

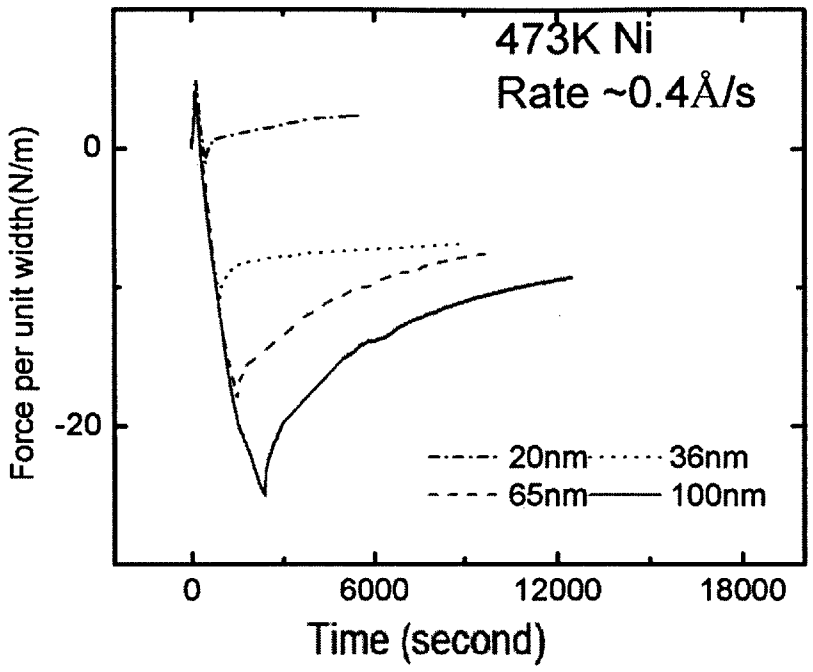

Figure 4.5. Stress evolution during growth of Ni films deposited at 473K with the growth interruption starting at different film thicknesses.

Similar phenomena have been observed in Ni films deposited at 473K. Up to a thickness of 100-150nm, such Ni films display a stress behavior similar to Type II intrinsic stress. During long growth interruptions, the change of force per unit width increases substantially with the film thickness, as shown in Figure 4.5. The stress curves during growth interruptions can be fit to double exponential decay functions. In Figure 4.6, we plot the thickness dependencies of the time constants and decay prefactors of the two processes. Again, it can be seen that the fast process is weakly dependent on film thickness and the slow process is strongly dependent on film thickness.

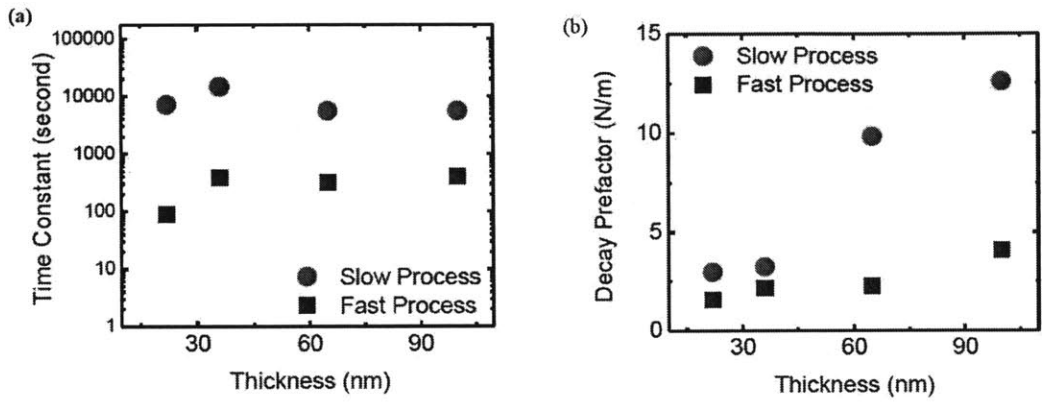

Figure 4.6. The thickness dependencies of the (a) time constant and (b) the decay pre-factor of nickel films deposited at 473K.

The results in Figure 4.3 to Figure 4.6 suggest that in both Ni and Au films, the stress evolution in the long-term growth interruption can be interpreted as a fast reversible surface process and a slow irreversible bulk process. To further understand the mechanisms of the two processes, it is useful to study their dependencies on the substrate temperature.

4.2.3 TEMPERATURE DEPENDENCE

In Figure 4.7, we compare the stress evolution during growth interruptions of 100nm-thick Ni films deposited at 300K and 473K, in which the long-term changes of the stresses differ significantly. From t=300 to 4500 seconds, the change of force per unit width is 5.6N/m for the film deposited at 473K but is negligible for the film deposited 300K. Therefore, the slow

process strongly depends on substrate temperature. However, as shown in the inset in Figure 4.7, the short-term stress change in Ni films has very weak temperature dependence. This is consistent with the fact that the kinetic processes occurring on the film surface usually have lower activation energy than those occurring in the bulk of the film. For example, the activation energy for surface diffusion is ~0.1-0.2eV, whereas the activation energy for grain boundary diffusion is ~0.5eV and for lattice diffusion is ~1eV [17].

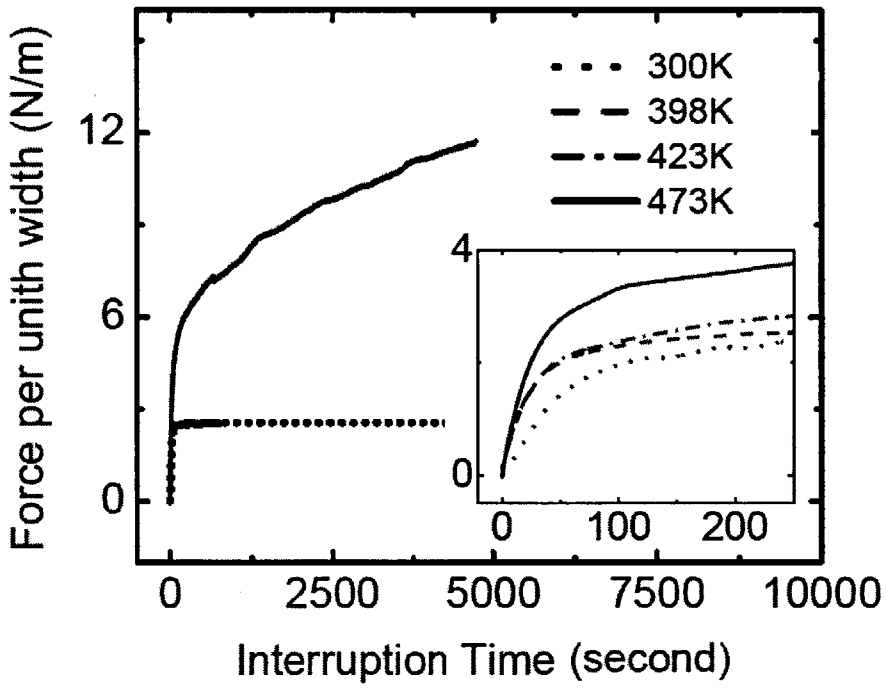

Figure 4.7. Temperature dependence of stress evolution during short and long interruptions in Ni films.

To summarize, two types of evolution processes are involved during growth interruptions. One is a fast reversible surface process, with a time constant of $\sim 10^2$ seconds. The other is a slow bulk irreversible process, with a time constant of $\sim 10^4$ seconds. The fast process is weakly dependent on substrate temperature, whereas the slow process is strongly dependent on substrate temperature. Chason *et al.* [13] have studied stress relaxation in a 100nm thick Ag film during an 800-second interruption. They determined the time constant as 108seconds, consistent with the fast process found here. The slow process has not been quantitatively characterized previously. We use the next section to study the slow bulk process.

4.3. GRAIN GROWTH AND THE SLOW PROCESS

The slow bulk process can include structure evolution, such as elimination of point, line or planar defects generated during deposition, as long as the evolution occurs throughout the bulk of the film, not just at the film's surface. In particular, grain growth could give rise to a substantial tensile rise in the bulk stress, as traction with the substrate constrains the densification caused by elimination of the excess free volume associated with grain boundaries.

4.3.1 GRAIN GROWTH AND TEXTURE EVOLUTION IN NICKEL FILMS

We used Transmission Electron Microscopy (TEM) to investigate the correlation between the microstructures and stress evolution in nickel and gold films. In the last section, we have compared the stress evolution during growth interruptions of 100nm-thick Ni films deposited at 473K and 300K. In the long term, the change of stress is 56MPa in the 473K-deposited film,

but is negligible in the 300K-deposited film (see Figure 4.7). Figure 4.8 shows the grain structure evolution during a growth interruption of the 473K-deposited film. Clearly, substantial grain growth occurs in the film as matrix grains grow into abnormal large grains during the growth interruption. As discussed in Subsection 2.1.5, grain growth in thin films can lead to a less compressive stress or a more tensile stress, consistent with what has been seen in the stress change in Figure 4.7. In contrast, no grain growth has been observed during growth interruptions of the 300K-deposited Ni films. The TEM analysis and stress measurement thus suggest that grain growth plays an important role in the slow bulk process of stress evolution in Ni films.

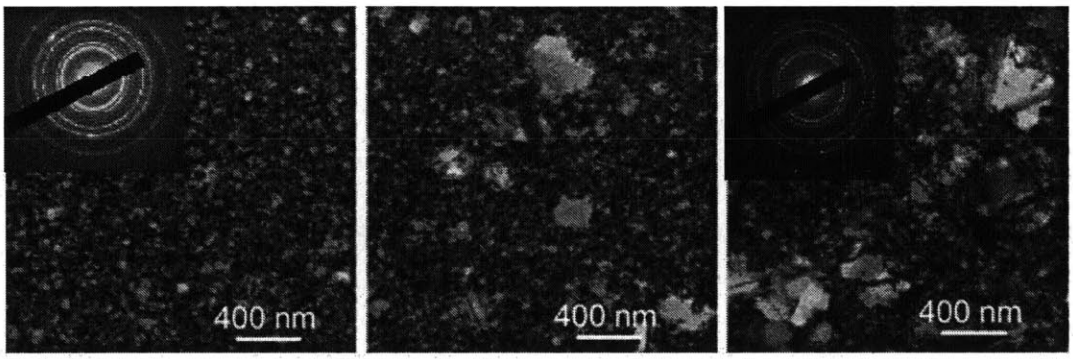

Figure 4.8. TEM micrographs of 100 nm Ni films deposited at 473K with interruption times of 0, 15 and 60min.

Grain growth is known as a thermally activated process. The weak temperature dependence of the stress change during short interruptions (inset of Figure 4.7) thus precludes the possibility of grain growth as a major mechanism for stress evolution in the short term. Another reason

that grain growth cannot be the dominant process for short interruptions is that grain growth is an irreversible process that cannot lead to the reversible stress change.

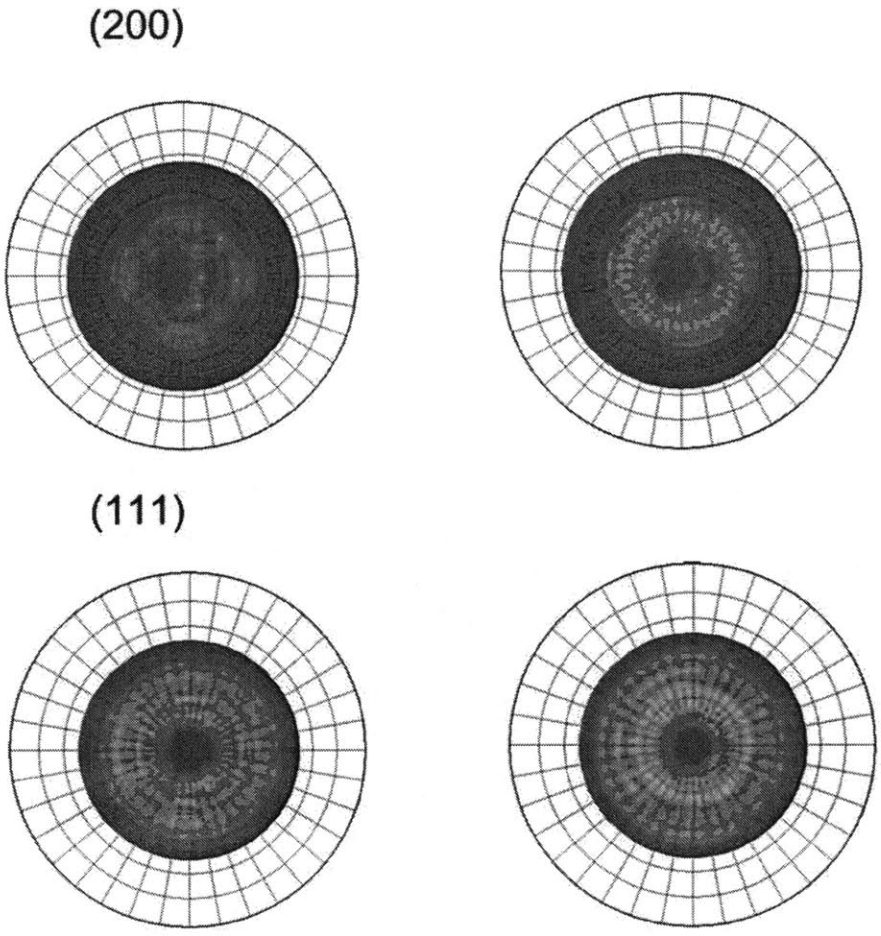

Figure 4.9. (200) and (111) pole figures of 100 nm Ni deposited at 473K with interruption times of 0min (left column) and 180min (right column).

Grain growth is also known as the origin of texture evolution [8]. In Figure 4.9, we compare the (111) and (200) pole figures of the 473K-deposited Ni films with interruption times of 0 and 180min. Here due to the geometry limitation of the equipment, the measurement was limited to $\sim 65°$ in the χ direction. It can be seen that the as-deposited film is strongly (111) textured. Although further annealing leads to a profound increase of the grain size, it only leads to a slight tightening of the (111) texture. As will be shown in Chapter 5, the grain size scales with film thickness in such Ni films because grain growth occurs during film thickening. Therefore, the alignment of crystallographic orientation is probably caused by the grain growth during film coalescence and film thickening.

In the literature, abnormal grain growth has been explained by particular grain boundaries possessing an advantage of mobility or energy [18], or driven by preferred crystallographic orientation with respect to the surface [19-21]. Because here the abnormal grain growth does not lead to a significant texture evolution, it might originate from specific grain boundaries of higher mobility or with lower kinetic barriers for migration.

4.3.2 GRAIN GROWTH AND THE ASSOCIATED DENSIFICATION STRESS IN GOLD FILMS

We have also studied the evolution of grain structure in polycrystalline gold films. Based on TEM analysis, we found that abnormal grain growth happens even if the gold film is deposited and annealed at room temperature. Figure 4.10 shows bright field TEM images of 45nm-thick gold films deposited at 300K after a growth interruption of 0.5hr, 8 and 26hr, The

grain structures are featured by the bimodal distribution of grain sizes: a few large grains with diameters ~100-500nm are embedded in a matrix of small grains with diameters ~20-30nm.

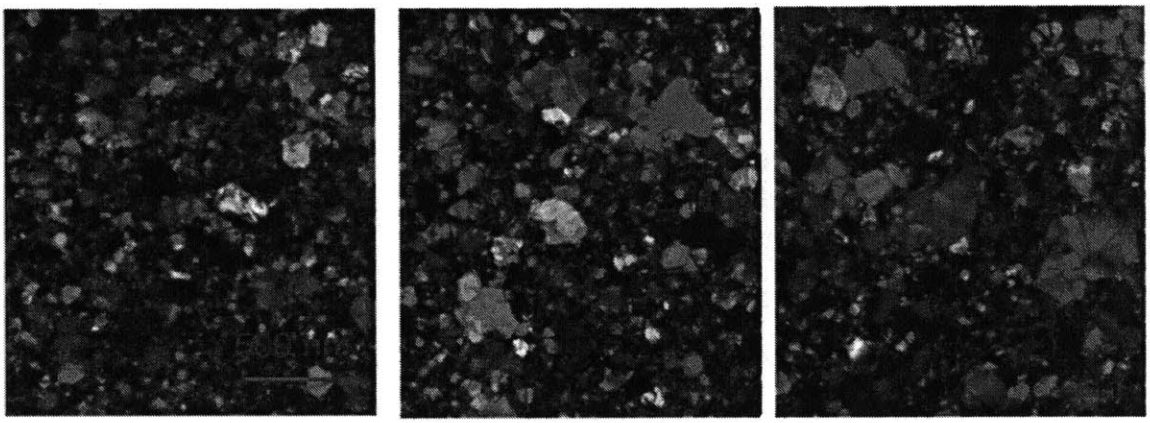

Figure 4.10. Grain structure of 45nm gold films with interruption times of 0.5, 8 and 26hours.

To understand the contribution of grain growth to the slow process, it is necessary to quantitatively characterize the evolution of the average grain size and the resultant densification stress. In theory, normal grain growth follows a parabolic law: $\bar{d}^n - \bar{d}_0^n \propto t$ with $n=2$, where t is time and $\bar{d}$ and $\bar{d}_0$ are the average grain size at time t and time zero. If the size of matrix grains remains unchanged, the average size of abnormally growing large grains should increase linearly with time ($n=1$) [19]. However, grain growth in nickel and gold films here is more complicated than these two cases. During a growth interruption for gold, large abnormal grains grow at the expense of matrix grains while the size of the latter also slightly increases. The average grain size is determined by the size and population of both the

abnormal large grains and matrix grains. Therefore, evolution of the average grain size during an interruption may not be well described by the simple models outlined above.

We quantified the average grain size using image analysis of grain boundaries that were manually traced from TEM micrographs onto transparencies. Each data point was determined from measurements of hundreds of grains in multiple micrographs. Figure 4.11 shows the grain size distribution and the average grain size as a function of the interruption time obtained using this method.

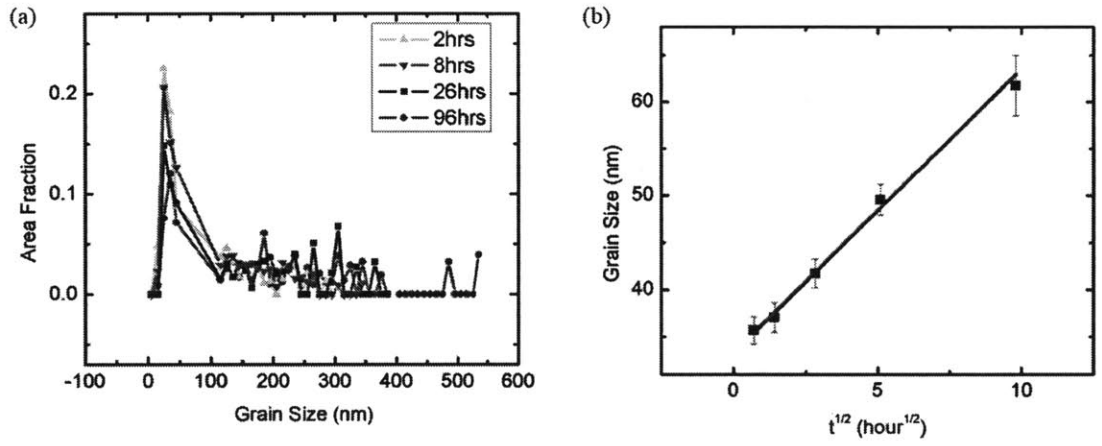

Figure 4.11. (a) The evolution of grain size distribution in gold films. The vertical axis is the area fraction occupied by the grains within a certain range of grain size. (b) Average grain size as a function of the square root of interruption time.

Figure 4.11 (b) shows that the average grain size in the 45nm thick gold films empirically follows a linear relationship with the square root of the interruption time:

$$\bar{d} - \bar{d}_0 = (kt)^{1/2} \quad . \tag{4.2}$$

Fitting this relationship gives $\bar{d}_0 = 33.31 \pm 0.50\,\text{nm}$ and $k = 9.145 \pm 0.841\,\text{nm/hr}$. The change in force per unit width caused by densification [21] is:

$$\Delta(\frac{F}{w})_{densification} = H_f \Delta\sigma_{gg} = H_f \frac{E}{1-\nu} \Delta a (\frac{1}{\bar{d}_0} - \frac{1}{\bar{d}}) \ , \tag{4.3}$$

Here $\Delta\sigma_{gg}$ is the change in the bulk stress caused by grain growth, E is the Young's modulus of the gold film, ν is the film's Poisson's ratio, and Δa is the average excess volume per area of grain boundary.

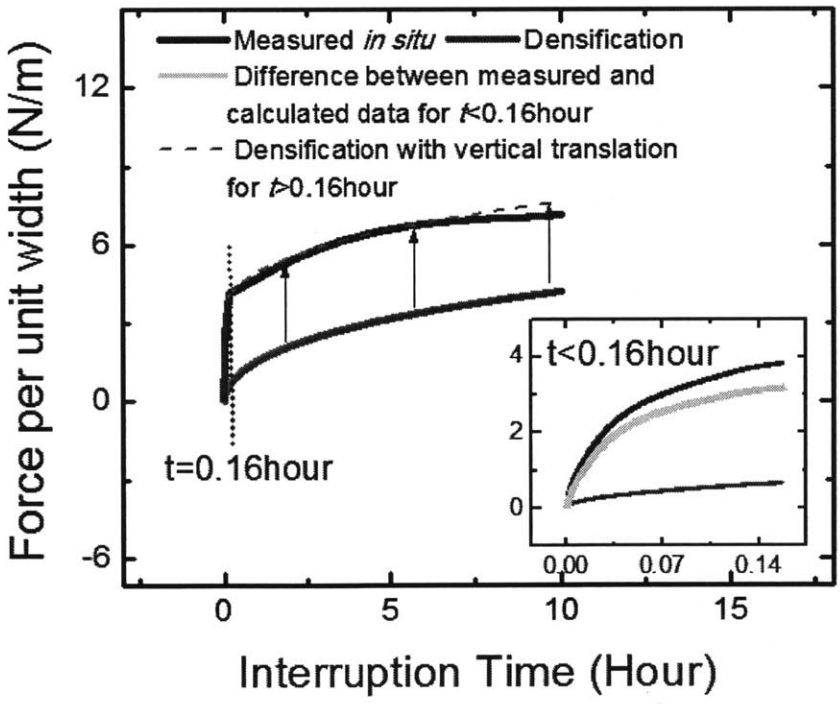

Figure 4.12. Stress evolution during a growth interruption of a 45nm gold film: comparison between the measured data and the contribution from grain growth.

Combing Equation (4.2) and (4.3) gives the stress evolution due to grain growth during a growth interruption. Figure 4.12 shows the stress evolution observed during an interruption of growth of a 45nm-thick film, along with the calculated stress due to grain growth, using $E = 78GPa$, $\nu = 0.44$, and $\Delta a = 1\mathring{A}$ [22]. It can be clearly seen that grain growth does not significantly contribute to the measured stress evolution up to t =0.16hr, during which the change of force per unit width is 3.4N/m, of which only 0.3N/m can be attributed to grain growth. During this period (see the inset of Figure 4.12), the difference between the measured and grain growth stress is large and can be well fit to a single exponential decay function, with pre-factor of 3.13N/m and a time constant of 158 seconds. These numbers are very similar to the results of the 45nm gold film shown in Figure 4.4, for which the fast process has a pre-factor of 3.16N/m and a time constant of 135 seconds. Clearly, there is an additional stress evolution process operating at short times. As also seen in Figure 4.12, after 0.16 hrs. both the magnitude and time evolution of the stress match what are expected from grain growth.

To summarize, by measuring the grain size as a function of the interruption time, we can estimate the stress evolution caused by film densification associated with the elimination of the excess volume in the grain boundaries. The analysis for gold films quantitatively shows that a significant portion of the stress change during long interruptions can be explained by the increase of the average grain size. This is a step further from the discussion in Subsection 4.3.1, where analysis for nickel films qualitatively shows that grain growth is an important mechanism for stress evolution in the long term.

4.4 EVOLUTION OF SURFACE TOPOGRAPHY AND THE FAST PROCESS

4.4.1 PROPOSAL FOR THE FAST PROCESS

The results in Section 4.3 strongly suggest that grain growth is an important mechanism for the slow irreversible process of stress evolution in Ni and Au films, and that there is an additional stress evolution process operating at short times. We propose that this fast process is associated with the change of surface structure facilitated by surface diffusion during growth interruptions. For polycrystalline films, this process is most likely related to a change in the shape of surfaces of individual grains. During coalescence, grain boundary formation ('zipping') leads to a relatively flat surface with shallow grooves at grain boundaries [23]. Under the deposition conditions used here, there will be copious nucleation of new ledges so that the growth surface remains flat, and minimal uphill diffusion occurs so that the grooves remain shallow, with a dihedral angle during growth θ_{growth}. The equilibrium dihedral angle of a grain boundary groove θ_{eq} is determined by the ratio of grain boundary energy to the energy of the surfaces of the grains [24]. During growth, the dihedral angle is larger than the equilibrium angle $\theta_{growth} > \theta_{eq}$. During a growth interruption, surface diffusion allows the groove to deepen to evolve to the equilibrium angle. This process is schematically shown in Figure 4.13.

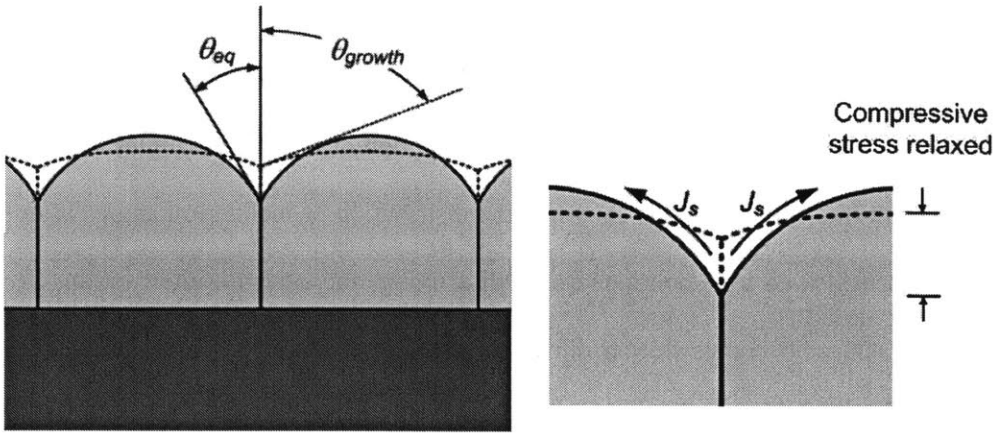

Figure 4.13. Illustration of the grooving process. The surface profile of individual grains is flatter with shallower grain boundary grooves during growth (dashed line), but relaxes toward an equilibrium shape during growth interruptions (solid line).

4.4.2 EVIDENCE FROM AFM AND CROSS-SECTIONAL TEM CHARACTERIZATION

Characterization of a Ni film's surface structure during growth interruptions supports this proposal. In this study, 100nm thick nickel films were deposited at 473K with a deposition rate of 5.0Å/s. After deposition, the films were kept in the vacuum chamber at 473K for a certain amount of time before they were quickly cooled to room temperature using cold nitrogen gas. Figure 4.14 (a), (b) and (c) show decorated AFM images ($0.5\mu m \times 0.5\mu m$) of the surfaces of films after growth interruptions of 0, 15 and 60 minutes, in which the local surface with an inclination angle <10°has been colored green. Here we define the inclination angle as the angle between the normal of the local surface and the normal of the horizontal

surface. A higher inclination angle thus means a steeper local surface. As the interruption time increases, more area becomes steeper than 10° and deep grooves develop along the edges of each surface domain. In Figure 4.15, we show the distribution of inclination angles after 0, 15, and 60min growth interruptions. Also shown is the distribution of inclination angles after a 60min interruption, followed by a continued growth of 40nm and a 15min interruption. It can be seen that the surface becomes steeper during a growth interruption but becomes flatter when the deposition is resumed.

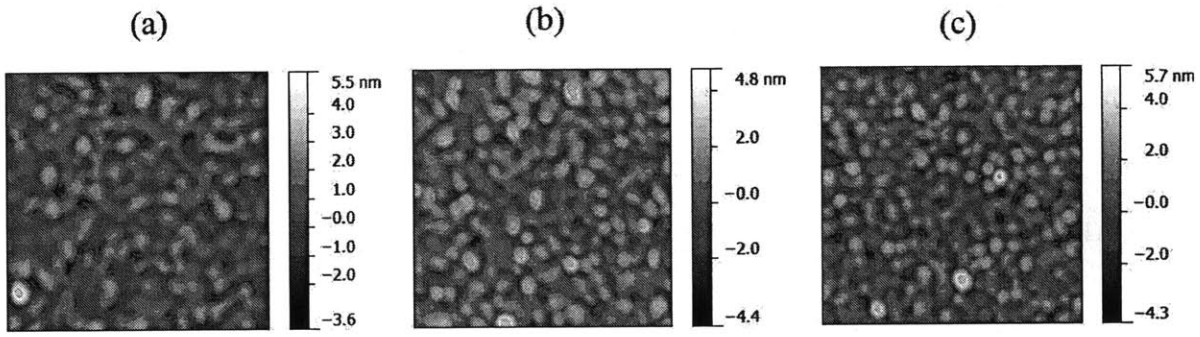

Figure 4.14. AFM images ($0.5\mu m \times 0.5\mu m$) of the surfaces of 100nm Ni films after growth interruptions of 0, 15 and 60 minutes at 473K. Here the local surface with an inclination angle <10°has been colored green.

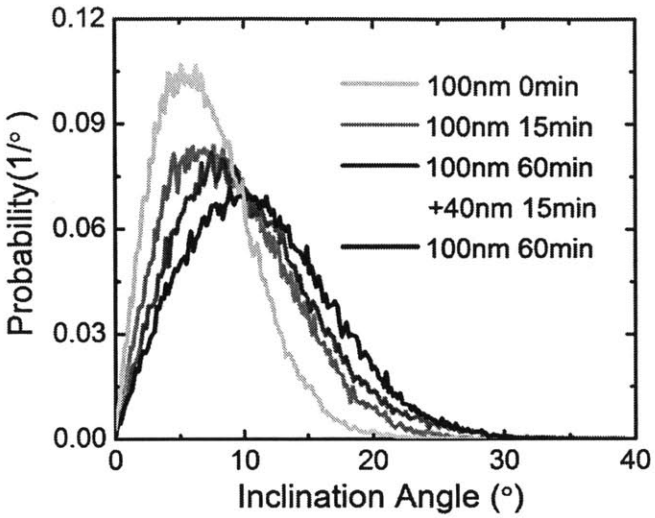

Figure 4.15. The inclination angle distribution of 100nm-thick films after growth interuptions of 0, 15, 60min and of an initially 100nm-thick film after an interruption of 60min followed by a depositon of 40nm and an interruption of 15min.

We define the region with an inclination angle $\theta > \theta^*$ as the deep grooving region, where θ^* is a threshold angle. By plotting the area of deep grooving regions as a function of the interruption time, we can estimate the time constant for the grooving process. Doing this we find that the time constant ranges from 396 to 420 seconds (see Figure 4.16) when setting the threshold angle $\theta^* = 8$, 12, 10, 15 or 18°. This is consistent with the time constant determined for the fast surface-related reversible stress relaxation process.

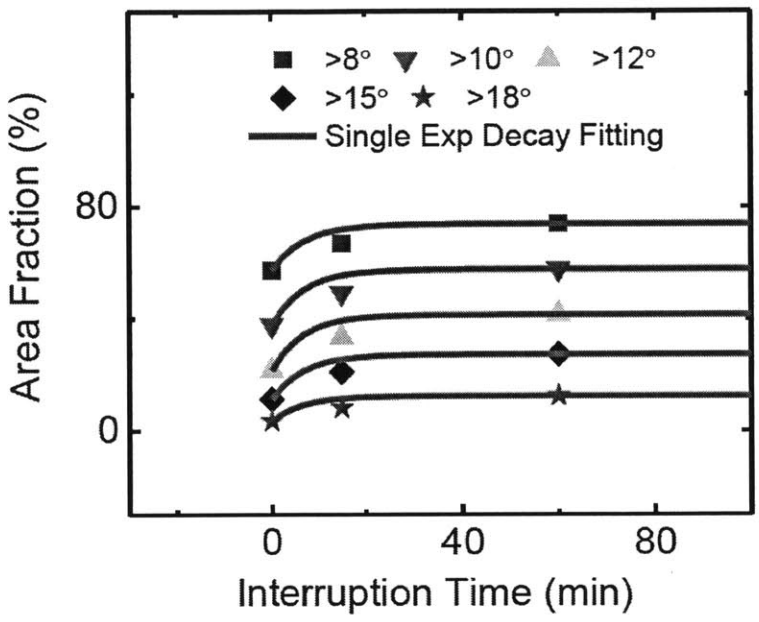

Figure 4.16. Area fraction of the deep grooving region as a function of the interruption time. The threshold angle is set as $\theta^* = 8,10,12,15,$ or 18°.

The surface profiles of these films have also been characterized using cross-sectional TEM. Figure 4.17 (a) and (b) show typical cross-sectional TEM images of Ni films after growth interruption of 0 and 60min. Here the surface profiles are highlighted in red. The former film surface is flatter than the latter, in which some deep grooves become visible. The high-magnification images in (c) and (d) highlight a shallow grain boundary groove in the film interrupted for 0min and a deep grain boundary groove in the film interrupted for 60min, respectively.

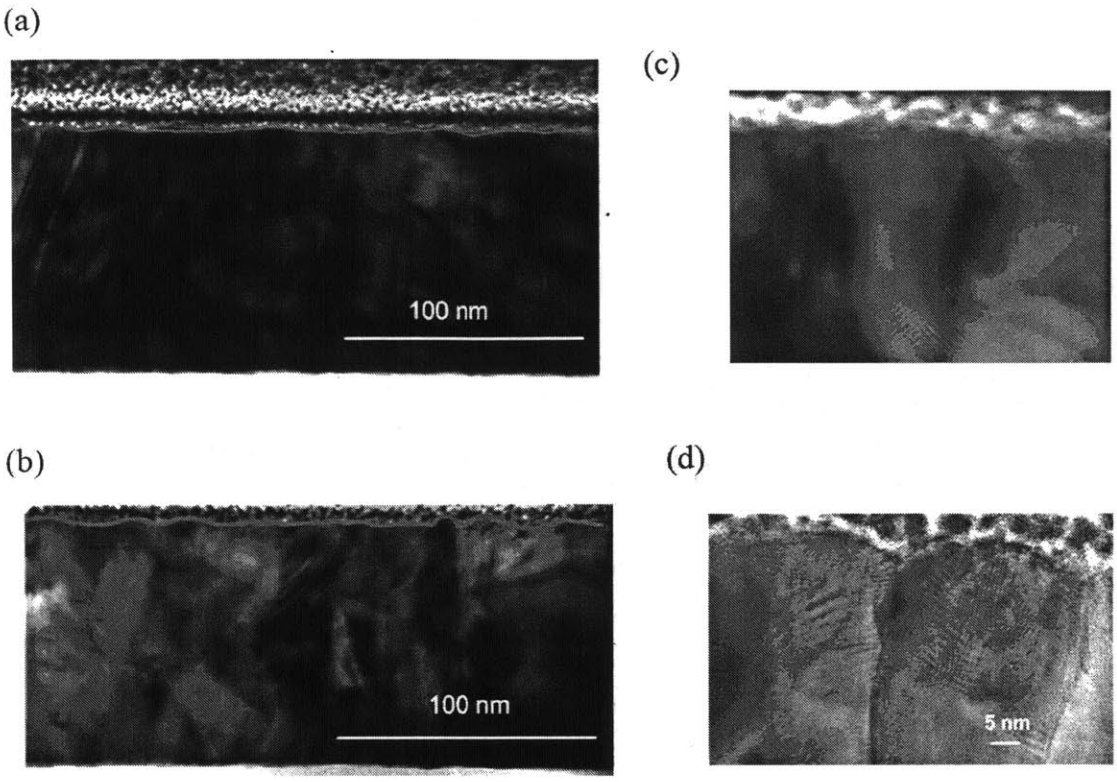

Figure 4.17. Cross-sectional TEM images of 100nm-thick Ni films after growth interruptions of (a) and (c) 0min, (b) and (d) 60min. The films were deposited and annealed at 473K during interruptions.

It is helpful to use cross-sectional TEM images to study the surface topography of abnormal large grains. Figure 4.18 shows a cross-sectional TEM image of an abnormal grain in Ni films. Rather than developing a perfect dome, we see a sinuate grain surface, which would be interpreted as multiple grains based on AFM analysis. Therefore, AFM images should not be used for grain size measurements in polycrystalline films--it provides topographic information about the film surface but not the information of crystallographic orientation. This sinuate surface may originate from the surface topography of multiple small grains eliminated during

grain growth. In addition, inside the abnormal large grain we see quite a few dislocation lines and other defects, many of which are not connected to grain boundaries or surface.

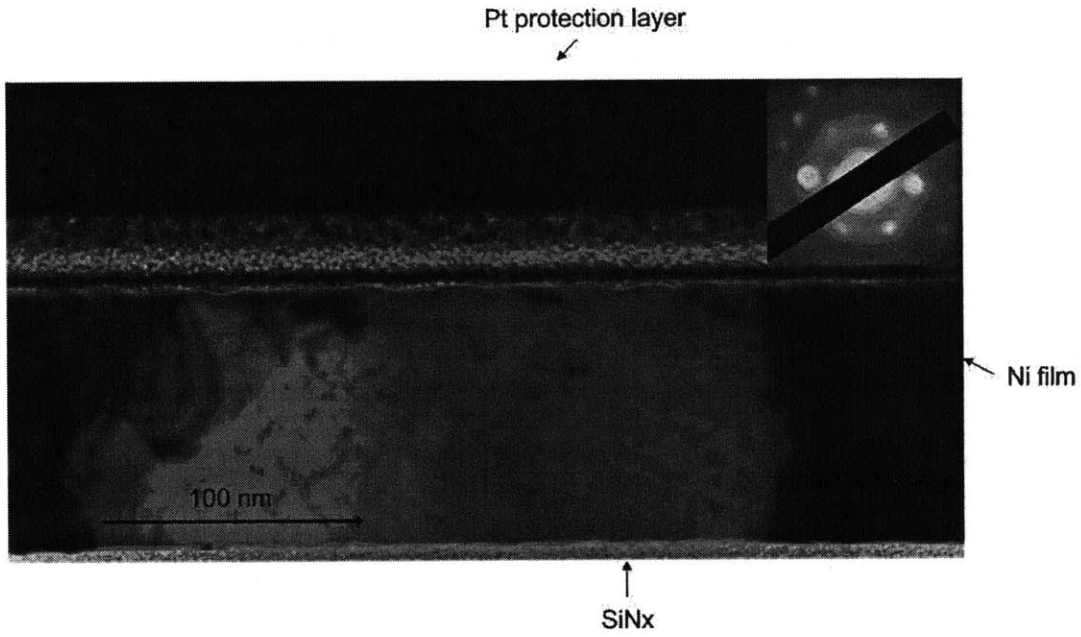

Figure 4.18. A cross-sectional TEM image of a 100nm Ni film. The surface profile of the large gain is highlighted in red.

Overall, the AFM and cross-sectional TEM results support the model proposed in Subsection 4.4.1, that the film surface right after deposition is largely flat, and shallow grooves at the grain boundary junction start to deepen during interruption of growth. It has been proposed that trapping of atoms at grain boundaries is likely to contribute to the observed compressive stress [13, 23]. According to the above model and experimental evidence, when growth is interrupted, surface diffusion will lead to grooves of equilibrium depth and will reduce the compressive stress associated with the excess atoms trapped at the grain boundaries (see

Figure 4. 13). AFM and TEM results show that the groove depth in the Ni film during a short interruption can be more than 5nm. *In situ* measurement shows that the compressive stress caused by trapped atoms at the grain boundary is ~500MPa in such Ni films (see Chapter 5). Therefore, this mechanism can lead to a change of (F/w) of around (0.5)(5nm)(500MPa)=1.25N/m, of the same order of magnitude as the initial tensile rise shown in the inset in Figure 4.7.

Once growth is resumed, flat surfaces and shallow grooves once again form, leading to the apparent reversibility of the process. This picture is consistent with the proposal by Chason *et al.* [13] that the post-coalescence compressive stress is associated with trapping of excess atoms at grain boundaries, and that the tensile rise during growth interruptions is associated with the removal of these trapped atoms. However, there is a critical difference in that here the removal process involves only surface diffusion, while Chason *et al.* proposed that the trapped atoms diffuse out of the grain boundaries, hence requiring that the grain boundary and surface diffusivities be similar in magnitude [25, 26].

4.4.3. ACTIVATION ENERGY OF THE FAST PROCESS

Leib and Thompson [27] have characterized the temperature dependence of stress evolution during growth interruptions and found that it is very weak. In establishing this, they considered a single decaying stress function and measured the relaxation constant at the beginning of the interruption. In the context of the analysis above, this would be a measurement relevant to the fast reversible process. Using a similar method, we can estimate

the activation energy for the fast process based on several short interruptions of growth of Ni films deposited at 300K, 398K, 423K and 473 (see Figure 4.19) K.

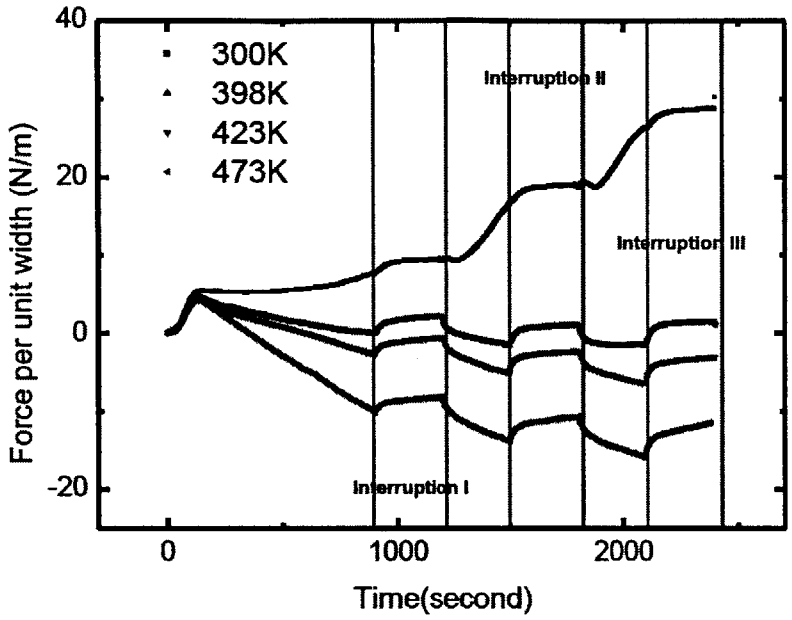

Figure 4.19. Stress evolution during growth and short interruptions of Ni films, with the substrate temperature ranging from 300K to 473K.

If we assume the strain rate fits a creep equation: $\frac{d\varepsilon}{dt} = A\sigma_i e^{-E_a/kT} + C_0$, then we have $Ae^{-E_a/kT} = \frac{\frac{d\varepsilon}{dt} - C_0}{\sigma_i}$, where σ_i is the stress right after interruption, C_0 is a constant. The activation energy E_a thus can be estimated by plotting $\ln(\frac{\frac{d\varepsilon}{dt} - C_0}{\sigma_i})$ vs $\frac{1}{T}$. Alternatively, if we

assume the rate of change of the force per unit width ($\frac{F}{w}$) fits a creep equation:

$\frac{d(\frac{F}{w})}{dt} = A(\frac{F}{w})_i e^{-E_a/kT} + C_0$, then $Ae^{-E_a/kT} = \frac{\frac{d(\frac{F}{w})}{dt} - C_0}{(\frac{F}{w})_i}$, where $(\frac{F}{w})_i$ is the force per unit width right after a growth interruption. The activation energy can be then estimated by plotting $\ln[\frac{\frac{d(\frac{F}{w})}{dt} - C_0}{(\frac{F}{w})_i}]$ vs $\frac{1}{T}$. Figure 4.20 (a) and (b) show these plots based on the stress curves in Figure 4.19.

We can also estimate the activation energy based on Mullins' analysis [28]. If we assume the compressive stresses in the surface layers are similar at various temperatures, the total released force per unit width during short interruptions should be proportional to the groove depth, i.e. $\Delta(\frac{F}{w}) \propto \Delta h \propto B^{1/4} \propto e^{-E_a/4kT}$. Here B is a function of surface diffusivity and E_a is the activation energy for surface diffusion. Therefore, we can plot $\ln(\Delta(\frac{F}{w}))$ vs $1/T$ to determine E_a. This result is shown in Figure 4.20(c).

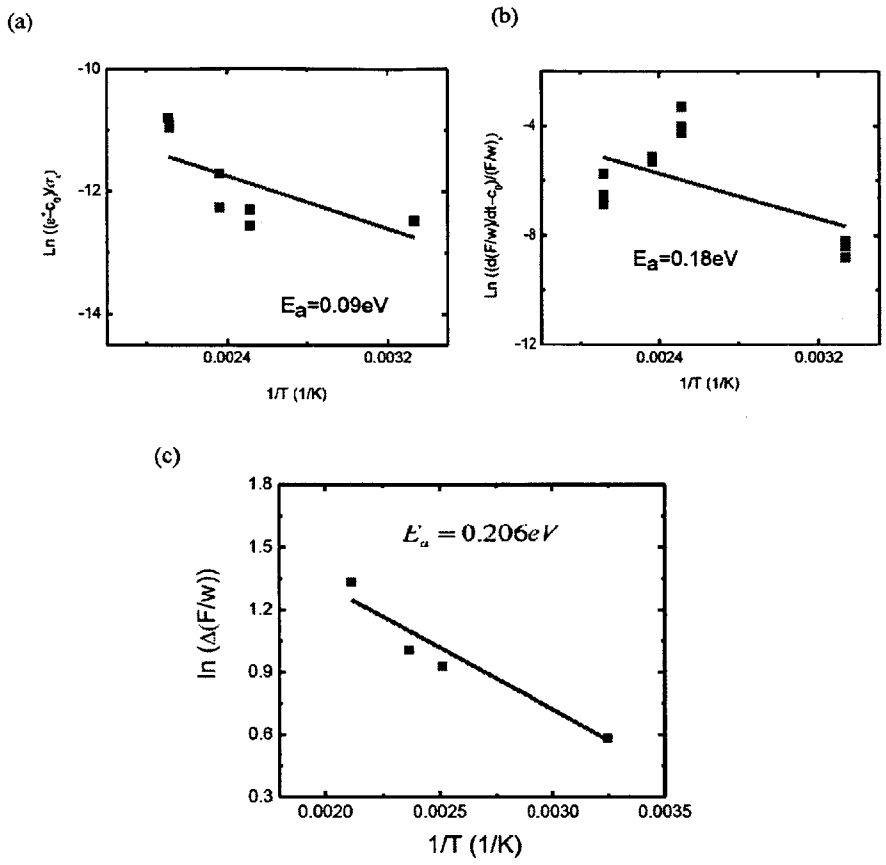

Figure 4.20. Activation energy of the fast process. (a) Fitting the strain rate to a creep equation. (b) Fitting the rate of change of the force per unit width to a creep equation. (c) Arrhenius plot based on Mullins' analysis.

The above methods generally give the activation energy for the fast process to be ~0.1-0.2eV.This low temperature dependence is consistent with the surface diffusion mechanism proposed here.

4.5 CONCLUSION

In conclusion, we have analyzed stress evolution during interruptions of growth of polycrystalline films, for different times, substrate temperatures and film thicknesses, and identified a fast and reversible surface process and a slow irreversible bulk process. We show that the slow irreversible process can be quantitatively explained to be a consequence of grain growth observed during interruptions of film growth, with stress evolution associated with the constrained densification caused by grain growth. We propose, and show evidence that, a change in the shape of the top surfaces of the grains is responsible for the fast surface-related 'reversible' change in stress. Specifically, we argue that during growth, the grain surfaces are flat, grain boundary grooves are shallow, and excess atoms are trapped at the grain boundaries. During growth interruptions, we show that grain boundary grooves deepen to approach their equilibrium depth and thereby relieve a component of the compressive stress associated with trapped atoms. This process occurs by surface diffusion and will hence be relatively weakly temperature dependent. Once growth is resumed, the steady state surface returns to one with relatively flat surfaces of individual grains and shallow grooves at grain boundaries, leading to the apparent reversibility associated with the fast stress evolution observed during growth interruptions.

REFERENCES

[1] M. Ohring, *The materials science of thin films* (Academic Press, Boston, 1992).

[2] T. Proulx, *Mems and nanotechnology, volume 2 : proceedings of the 2010 annual conference on experimental and applied mechanics* (Springer, New York, 2011).

[3] S. M. Spearing, Acta Materialia **48**, pp. 179 (2000).

[4] Z. Zhou, Zhongguo yi qi yi biao xue hui., and SPIE (Society), in *Proceedings of SPIE,* (SPIE, Bellingham, Wash., 2009).

[5] S. W. Lee, M. T. McDowell, L. A. Berla, W. D. Nix, and Y. Cui, Proceedings of the National Academy of Sciences of the United States of America **109**, pp. 4080 (2012).

[6] C. M. Suh, B. W. Hwang, and R. I. Murakami, Materials Science and Engineering a-Structural Materials Properties Microstructure and Processing **343**, pp. 1 (2003).

[7] A. Misra, S. Fayeulle, H. Kung, T. E. Mitchell, and M. Nastasi, Nuclear Instruments & Methods in Physics Research Section B-Beam Interactions with Materials and Atoms **148**, pp. 211 (1999).

[8] C. V. Thompson, Annual Review of Materials Science **30**, pp. 159 (2000).

[9] R. Koch, Journal of Physics-Condensed Matter **6**, pp. 9519 (1994).

[10] J. A. Floro, E. Chason, R. C. Cammarata, and D. J. Srolovitz, Mrs Bulletin **27**, pp. 19 (2002).

[11] F. Spaepen, Acta Materialia **48**, pp. 31 (2000).

[12] C. Friesen, and C. V. Thompson, Physical Review Letters **89** (2002).

[13] E. Chason, B. W. Sheldon, L. B. Freund, J. A. Floro, and S. J. Hearne, Physical Review Letters **88** (2002).

[14] E. Chason, J. W. Shin, S. J. Hearne, and L. B. Freund, Journal of Applied Physics **111** (2012).

[15] R. Koch, D. Z. Hu, and A. K. Das, Physical Review Letters **94** (2005).

[16] R. Koch, D. Z. Hu, and A. K. Das, Physical Review Letters **95** (2005).

[17] R. W. Balluffi, S. M. Allen, W. C. Carter, and R. A. Kemper, *Kinetics of materials* (Wiley-Interscience, Hoboken, N.J., 2005).

[18] F. J. Humphreys, and M. Hatherly, *Recrystallization and related annealing phenomena* (Elsevier, Amsterdam ; Boston, 2004), 2nd edn.

[19] C. V. Thompson, Journal of Applied Physics **58**, pp. 763 (1985).

[20] C. V. Thompson, and R. Carel, in *Grain Growth in Polycrystalline Materials Ii, Pts 1 and 2*, edited by H. Yoshinaga, T. Watanabe, and N. Takahashi1996), pp. 83.

[21] C. V. Thompson, and R. Carel, Journal of the Mechanics and Physics of Solids **44**, pp. 657 (1996).

[22] M. A. Meyers, K. K. Chawla, and Books24x7 Inc., (Cambridge University Press, Cambridge ; New York, 2009).

[23] W. D. Nix, and B. M. Clemens, Journal of Materials Research **14**, pp. 3467 (1999).

[24] G. L. J. Bailey, and H. C. Watkins, Proceedings of the Physical Society of London Section B **63**, pp. 350 (1950).

[25] P. R. Guduru, E. Chason, and L. B. Freund, Journal of the Mechanics and Physics of Solids **51**, pp. 2127 (2003).

[26] J. S. Tello, and A. F. Bower, Journal of the Mechanics and Physics of Solids **56**, pp. 2727 (2008).

[27] J. Leib, and C. V. Thompson, Physical Review B **82** (2010).

[28] W. W. Mullins, Acta Metallurgica **6**, pp. 414 (1958).

CHAPTER 5

MECHANISMS FOR STRESS EVOLUTION DURING POLYCRYSTALLINE FILM GROWTH IN ALL TEMPERATURE REGIMES

5.1 INTRODUCTION

Depending on the homologous temperature of the system (the deposition temperature divided by the film's melting temperature in ^{o}K), or the atomic mobility, two types of intrinsic stress behavios have been identified [1, 2] in polycrystalline systems. Type I behavior is observed in low atomic mobility systems, represented by refractory metals (e.g. Ti, Cr, and W) deposited at room temperature, and Type II behavior is observed in high atomic mobility systems, including metals with low melting points (e.g. Au, Ag, and Cu) deposited at room temperature and refractory metals deposited at elevated temperatures. Throughout the coalescence process, both Type I and Type II develop tensile stress, which has been well explained by the Hoffman-Nix-Clemens mechanism [3-6]. Postcoalescence tensile stress in Type I behavior has been attributed to epitaxial inheritance and low surface diffusion. Although several models [7-12] have been proposed, the origin of the postcoalescence compressive stress observed in Type II systems is not well understood.

In this chapter, we present a systematic study of the microstructure and intrinsic stress evolution in a range of materials and under a range of experimental conditions. In particular, a

stress turnaround phenomenon that strongly depends on substrate temperature and deposition rate has been investigated for systems at intermediate homologous temperatures. The fact that none of the previously proposed models [7-12] can explain this phenomenon calls for a better and more comprehensive understanding of the stress evolution processes during polycrystalline film growth. The results of *in situ* stress measurements are presented in Section 5.2. Also presented is the grain structure characterization of these films, showing that the grain size scales with film thickness.

In Section 5.3, we analyze the influence of grain growth during deposition on instantaneous stress. Taking into account the effect of strain gradient and yielding, we derive a series of equations to quantify the associated stress. We propose a new model for the compressive component of the intrinsic stress in Section 5.4. According to this model, the magnitude of the compressive component is controlled by a competition between adatom incorporation into 2D islands on the surface and adatom trapping at the boundaries. The increase of grain size not only leads to a tensile component of the intrinsic stress, but also alters the grain size dependence of the compressive component, from being independent of, to scaling with, the inverse of the grain size.

In Section 5.5, we compare the modeling results to the experimental data, and show that the analyses are applicable to systems at high (Type II) as well as low (Type I) homologous temperatures. We conclude that grain growth and excess adatoms trapped in the grain boundaries are two important mechanisms for stress evolution during Volmer-Weber growth at high and intermediate homologous temperatures. In Section 5.6, we discuss the stress evolution during a growth interruption and upon resumption at intermediate homologous

temperatures. The key findings of this chapter are summarized in Section 5.7, including an updated stress categorization scheme.

5.2 A NEW STRESS BEHAVIOR OBSERVED AT INTERMEDIATE HOMOLOGOUS TEMPERATURE

Materials have been divided into two categories based on their intrinsic stress behaviors. At room temperature, metals of high melting point (e.g. Pt, Cr and Ti) display Type I stress behavior, while metals of low melting point (e.g. Au, Ag, and Cu) display Type II. The melting points of commonly used metals are summarized in Table 5.1, which shows that the melting points of nickel and palladium are in the middle between the materials displaying Type I and Type II stress. The first question posed here is: how does the intrinsic stress evolve during deposition of nickel and palladium?

Metal	Cr	Pt	Ti	Pd	Ni	Cu	Au	Ag
Melting Point / K	2130	2045	1941	1827	1726	1356	1337	1235
Crystal Structure	BCC	FCC	HCP	FCC	FCC	FCC	FCC	FCC

Table 5.1. Melting point and crystal structure of commonly used metals.

5.2.1 STRESS TURNAROUND

Figure 5.1 shows the intrinsic stress behavior of polycrystalline palladium and nickel films at room temperature. Similar to Type II behavior, the tensile coalescence stress in these films decreases after the film becomes continuous. However, the slope of the stress curve at a given thickness, or the instantaneous stress σ_{in}, continues to evolve during film thickening, eventually turning around from compressive to tensile. In other words, the stress curve reaches a minimum at a certain film thickness. We will refer to this thickness as the turnaround thickness.

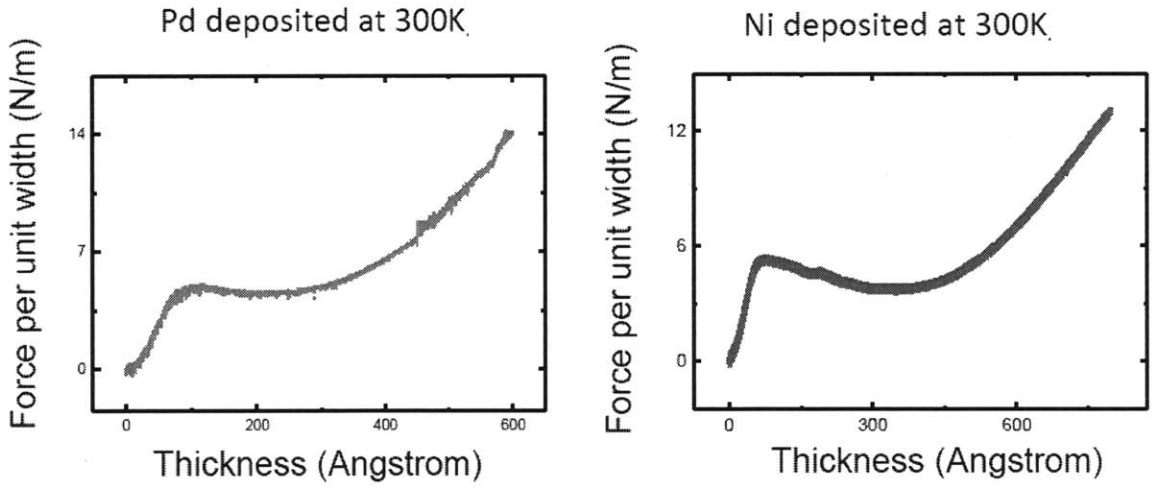

Figure 5.1. Stress evolution in Pd and Ni films deposited at 300K.

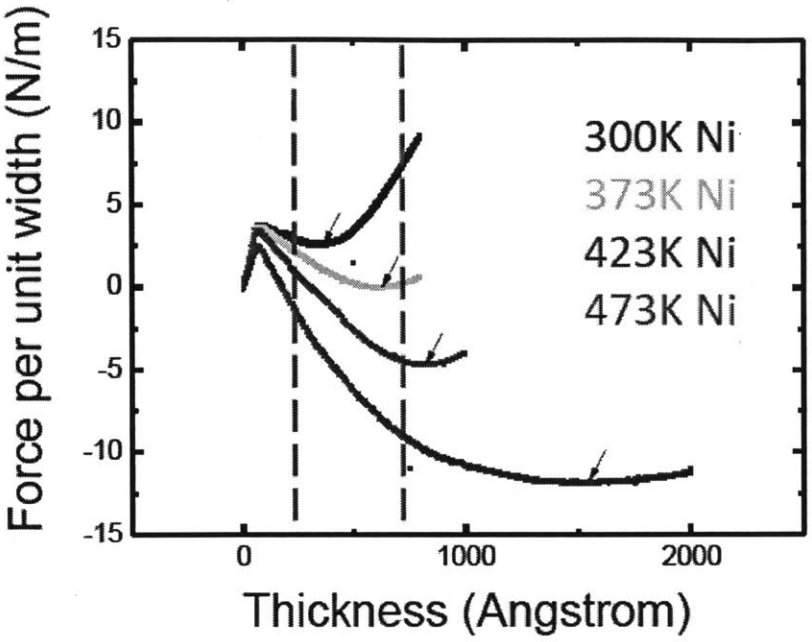

Figure 5.2. Stress turnaround in Ni films deposited at 300K, 373K, 423K and 473K.

The mechanisms that affect stress evolution strongly depend on homologous temperatures. Therefore, depositing the same material at different substrate temperatures may change the shape of the stress curve. Figure 5.2 compares the stress behaviors of Ni films deposited at different substrate temperatures ranging from 300K to 473K. A few points should be noted. First, stress turnaround occurs throughout this homologous temperature range. Second, the turnaround thickness increases with temperature. Third, for the same film thickness, the instantaneous stress is more compressive or less tensile at higher temperatures. For the Ni films deposited below 373K, the average stress of the films never becomes compressive because stress turnaround occurs early at lower temperatures.

We name the stress behavior associated with the stress turnaround phenomenon as the 'intermediate type', which is observed in films deposited at intermediate homologous temperatures. The postcoalescence stress is tensile in Type I, is compressive in Type II, and transits from compressive to tensile in the intermediate type behaviors. To compare Type I, Type II and the intermediate type stress behavior, in Figure 5.3 we show the stress evolution curves for a number of polycrystalline systems. Here at room temperature, Pt shows typical Type I behavior while Au shows behavior typical of Type II materials. The intermediate type behavior is observed in Ni deposited from 300K to 473K and in Pd deposited at 300K. The arrows in Figure 5.3(a) point out where stress turnaround happens during growth. Figure 5.3 (b) shows plots of average stress in these films.

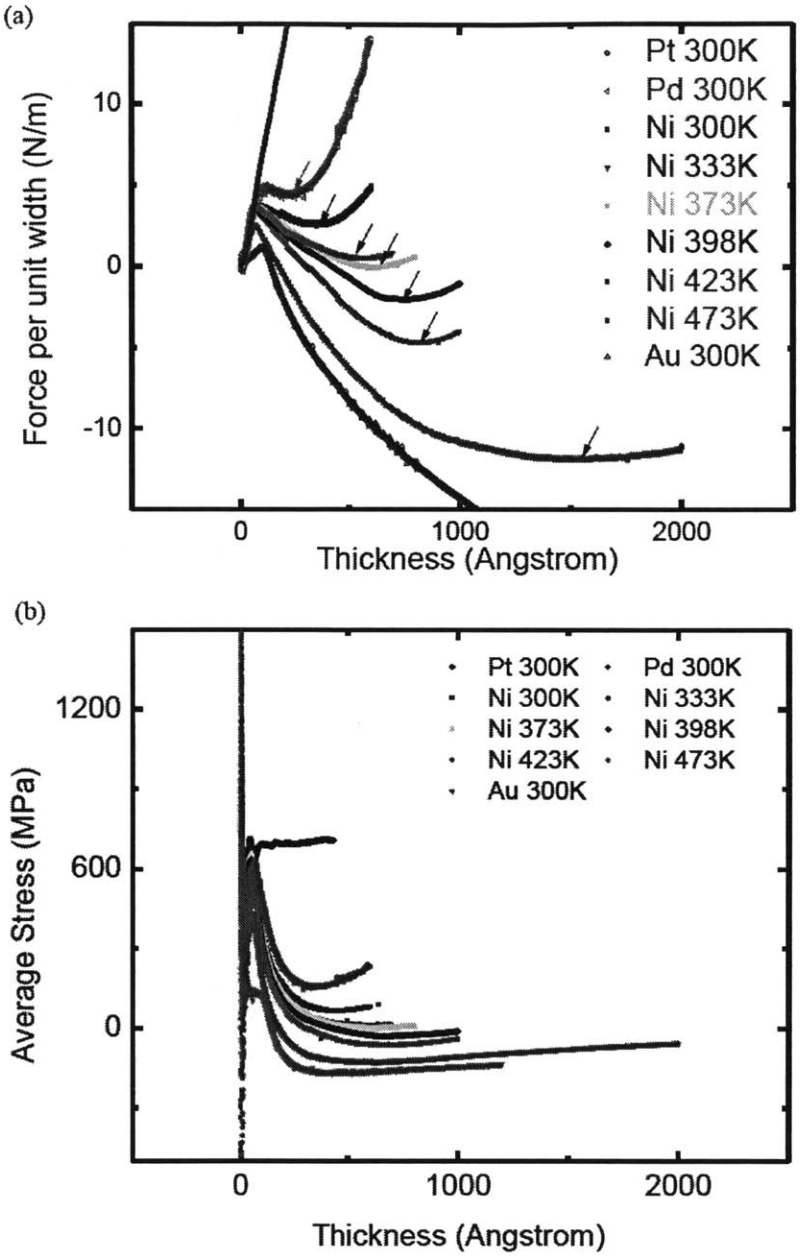

Figure 5.3. (a) Stress evolution in Pt, Pd and Au deposited at 300K, and Ni deposited at 300, 333, 373, 398, 423 and 473K, with the deposition rate fixed at 0.5 Å/s. (b) Plots of the average stress in these films.

We have also studied the deposition rate dependence of the turnaround behavior. Figure 5.4 shows stress evolution in Ni films deposited at 373K. The deposition rates were kept constant at 0.5 *Å*/s during the growth of the initial 15nm in all cases, to ensure that the films had similar grain structures right after coalescence. From 15nm to 100nm, deposition rates were 2.5, 1.3, 0.8, 0.5, and 0.3 *Å*/s. The plots clearly show that the turnaround thickness increases with lower deposition rates. In addition, it can be seen that for the same film thickness, the instantaneous stress is more compressive or less tensile with lower deposition rates.

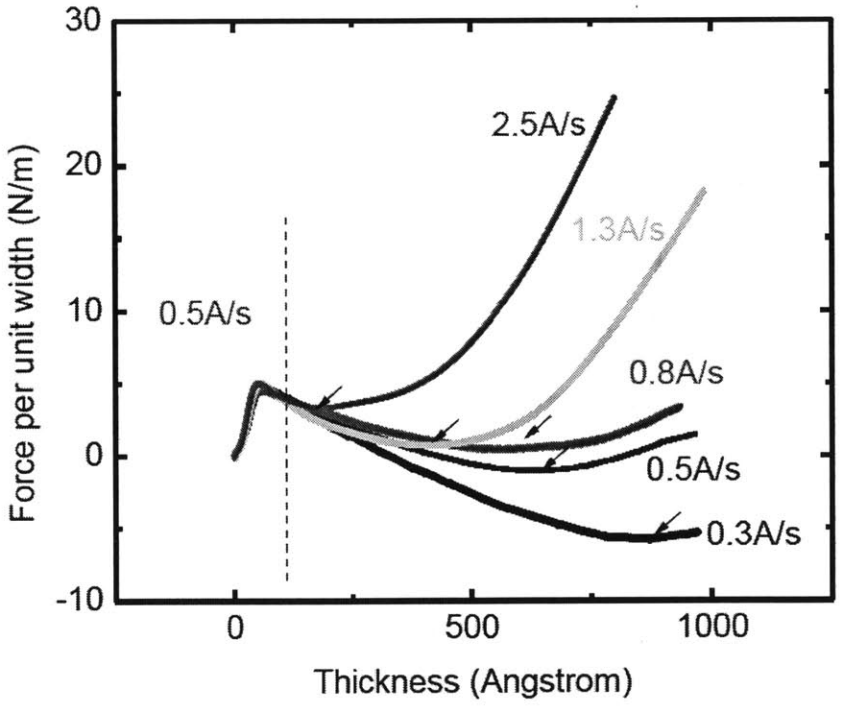

Figure 5.4. The deposition rate dependence of the stress turnaround phenomenon in Ni films deposited at 373K.

The findings from Figure 5.1 to Figure 5.4 indicate that at least two mechanisms operate during postcoalescence growth. One causes a tensile component of the intrinsic stress and the other causes a compressive component. The compressive component is favored at higher temperatures or at lower deposition rates.

5.2.2 MICROSTRUCTURE EVOLUTION

Evolution of a film's microstructure during deposition strongly influences the development and evolution of its intrinsic stress. However, this effect has not been taken into account in previous models. Transmission Electron Microscopy (TEM) was used to study the microstructures of films in this work. Figure 5.5 shows plan view, bright field TEM images of Ni films deposited from 300K to 473K, with thicknesses of 7nm, 20nm and 37nm. The grain size is clearly seen to increase with the film thickness at each temperature.

In Figure 5.6, we use image analysis to quantify the average grain size in Ni films deposited at various temperatures. The range of film thickness matches the plots in Figure 5.3. Each data point was determined by tracing the boundaries of hundreds of grains on transparencies followed by automated image analysis of the transparencies. Figure 5.6 shows that from 300K to 473K, the grain size scales with film thickness and the relationship is very weakly dependent on temperature. This behavior may be associated with the presence of a deposition flux during grain growth.

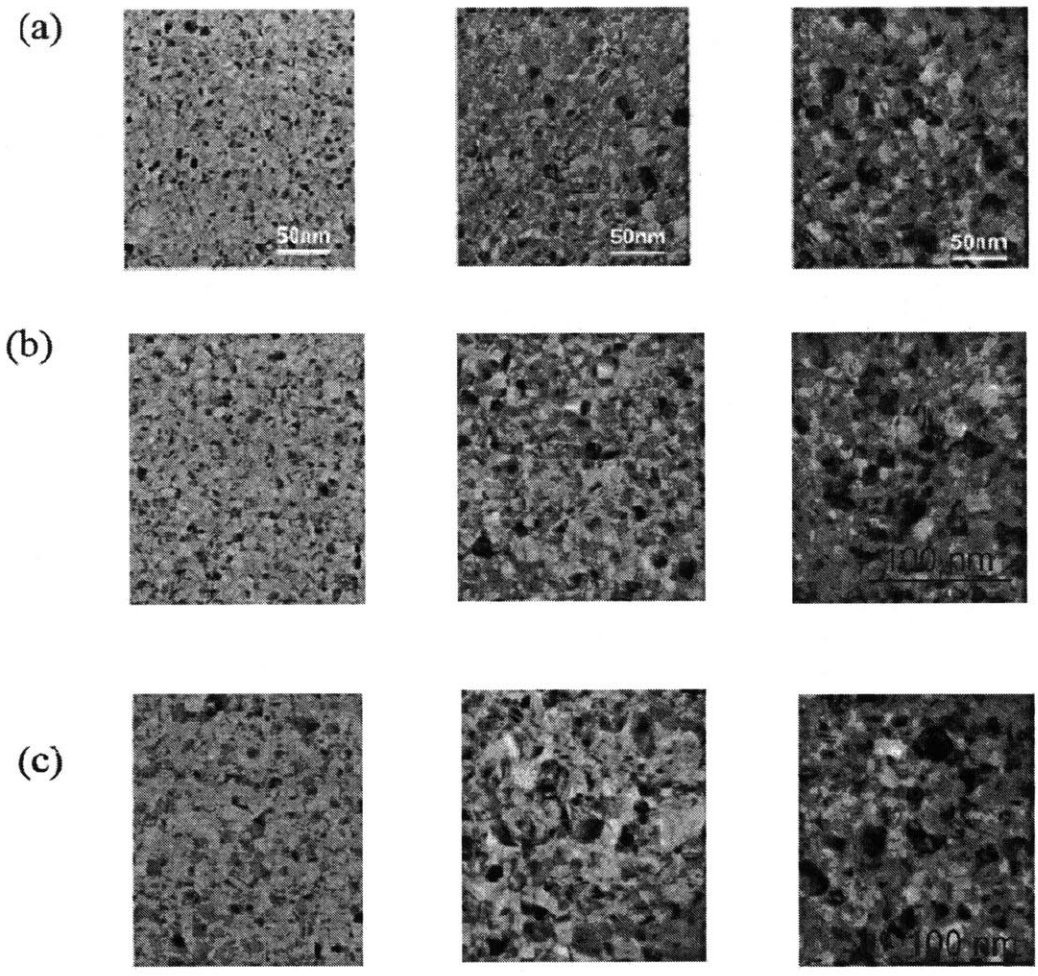

Figure 5.5. Grain structure of Ni films deposited at (a) 300K, (b) 373K, and (c) 473K. For each temperature, the film thicknesses are 7nm, 20nm and 37nm from the left to the right. Note the scale bar is 50nm in (a) and is 100nm in (b) and (c).

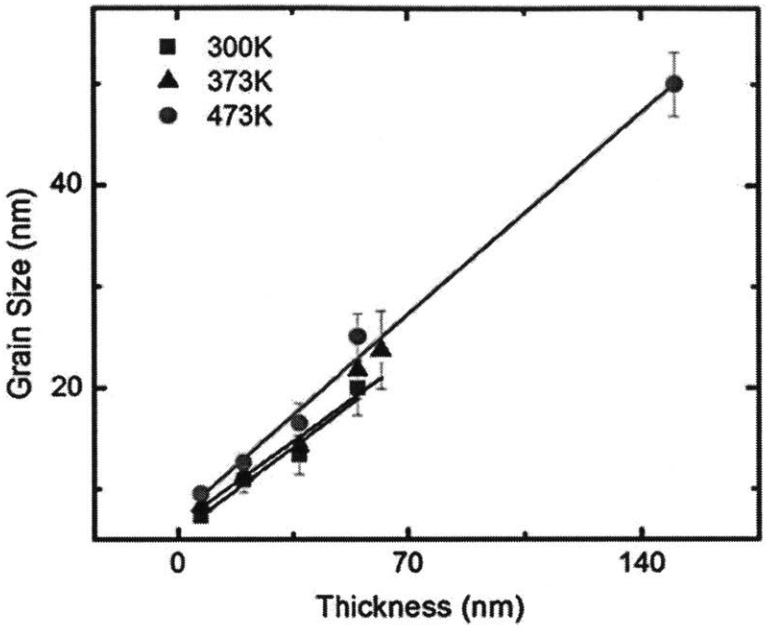

Figure 5.6. Grain size as a function of film thickness in Ni films deposited at intermediate homologous temperatures.

Grain growth leads to elimination or redistribution of the excess free volume associated with grain boundaries, and can lead to densification of freestanding materials. However, because of traction at the film-substrate interface, grain growth leads to a tensile stress [13]. During deposition, grain growth continuously changes the bulk stress in the film. This gives rise to a tensile component of the measured instantaneous stress, the magnitude of which will be discussed in detail in the next section.

5.3 INFLUENCE OF GRAIN GROWTH ON INSTANTANEOUS STRESS DURING DEPOSITION

5.3.1GENERAL EXPRESSION

The contribution of grain growth to the instantaneous stress (σ_{in}^{gg}) during deposition can be modeled based on the grain size-thickness plot in Figure 5.6. Consider a very small period during deposition ($t \to t+\Delta t$), during which the average grain size increases as $d \to d+\Delta d$ while the film thickness increases as $h \to h+\Delta h$. The increase of the average stress in the bulk of the film owing to redistribution of the excess free volume at grain boundaries is [14]

$$\Delta\bar{\sigma}(t \to t+\Delta t) = M\Delta a(\frac{1}{d} - \frac{1}{d+\Delta d}). \tag{5.1}$$

Here Δa is the grain boundary width and M is the biaxial modulus of the film. The measured force per unit width $(\frac{F}{w})$ increases by

$$\Delta(\frac{F}{w})(t \to t+\Delta t) = \Delta\bar{\sigma}(t \to t+\Delta t)h. \tag{5.2}$$

The linear relationship between the grain size and film thickness in Figure 5.6 leads to $\frac{\Delta d}{d} = \frac{\Delta h}{h}$. Therefore, the instantaneous stress caused by grain growth is

$$\sigma_{in}^{gg}(d) = \frac{\Delta(\frac{F}{w})(t \to t+\Delta t)}{\Delta h(t \to t+\Delta t)} = M\Delta a\frac{\Delta d}{d^2} \times \frac{h}{\Delta h} = M\frac{\Delta a}{d}. \tag{5.3}$$

5.3.2 STRAIN GRADIENT

Grain growth continues to occur during deposition so that more grain boundary area is eliminated in the bottom layers of the film than in the top layers during deposition. As a result, this mode of grain growth gives rise to a strain gradient throughout the film, with the top layers being less tensile than the bottom layers. Both the average intrinsic stress and the strain distribution in the film evolve during the deposition process.

To investigate how grain growth affects the strain distribution in the film, we first assume that the layers are stress-free when they are initially deposited on the film surface, and that grain growth is the only source of intrinsic stress. Assuming that the deposition starts at $t = 0$, then what is the densification strain in the layer of position z (the distance from this layer to the substrate-film interface) at any time t?

The grain size scales with film thickness during deposition, i.e. $\frac{d}{h} = k$ where k is a dimensionless constant. At time t, the film thickness is $h = Rt$ and the grain size is $d = kh$, where R is the deposition rate. The in-plane size in the layer positioned at z is also $d = kh = kRt$, as shown in Figure 5.7 (a). When this layer was first deposited on film surface (Figure 5.7 (b)), its in-plane size was $d' = kz$. Now the grain size increases to $d = kRt$. Therefore, the total densification strain in this layer at time t is $\varepsilon(z,t) = \Delta a(\frac{1}{d'} - \frac{1}{d})$, or

$$\varepsilon(z,t) = \frac{\Delta a}{k}(\frac{1}{z} - \frac{1}{Rt}). \tag{5.4}$$

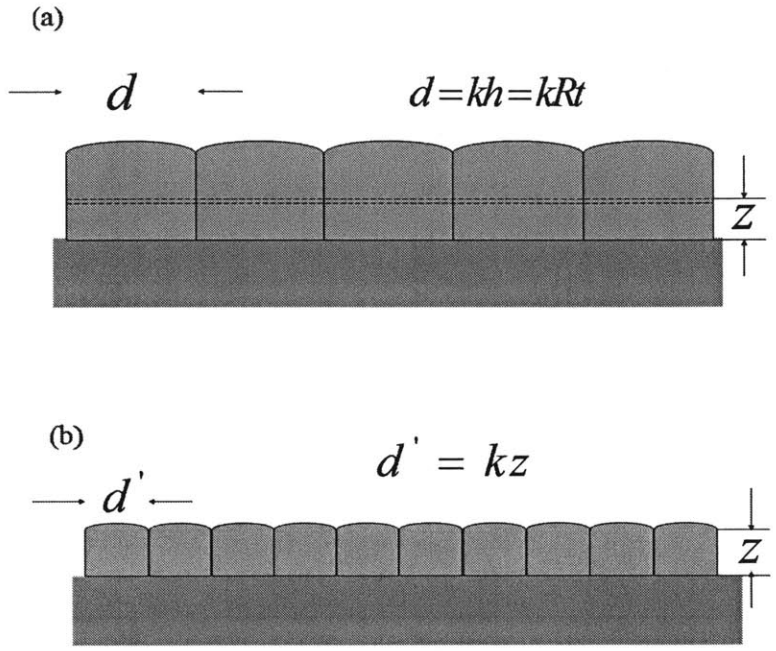

Figure 5.7. Illustration of how grain growth affects the strain in the film. (a) At time t, the film thickness is $h = Rt$, the grain size is $d = kh = kRt$. (b) The time when the layer at z was first deposited. The in-plane size was $d' = kz$.

Equation (5.4) describes how the strain distribution changes with time. Here z is the position of a certain layer. At any time, the layers close to the film surface (with larger z) are less tensile strained than those close to the substrate are (with smaller z). For a certain layer, as time increases, the strain becomes more tensile because densification continues to occur during deposition. Figure 5.8 illustrates how the strain distribution evolves in a film during deposition. Here we assume that the grain size equals the film thickness during deposition, with a deposition rate of $1\mathring{A}/s$.

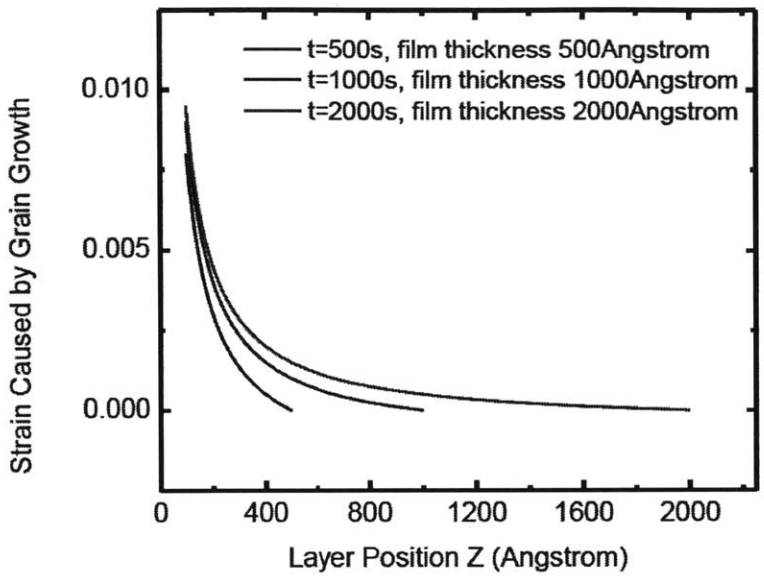

Figure 5.8. Evolution of the strain distribution caused by grain growth. Basic assumptions: deposition rate is $1\text{Å}/s$; the grain size to thickness ratio is $k=1$.

5.3.3 EFFECT OF YIELDING

If all the strains are accommodated elastically, the stress distribution evolves as $\sigma(z,t)=\frac{E}{1-\nu}\frac{\Delta a}{k}(\frac{1}{z}-\frac{1}{Rt})$. However, given that the initial grain size is only a few nanometers under normal experimental conditions, the total grain growth stress in the bottom layers can exceed the yield stress of the film during thickening. As shown in Figure 5.8, the tensile strain in the bottom layers (with smaller z) can be very large during deposition, e.g. larger than 0.5%. For polycrystalline metal films, the yield limit is always reached when $\varepsilon < 0.2\%$.

It is thus likely that during deposition the tensile strain in the bottom layers has reached the yield limit.

If the layer at z_y has reached the yield limit (this means layers under z_y have all reached the yield limit), then

$$\sigma_y = \frac{E}{1-\nu}\frac{\Delta a}{k}\left(\frac{1}{z_y} - \frac{1}{Rt}\right). \tag{5.5}$$

Therefore,
$$z_y(t) = Rt\frac{1}{1+\dfrac{\sigma_y(1-\nu)(kRt)}{E\Delta a}}, \tag{5.6a}$$

or
$$z_y(h) = h\frac{1}{1+\dfrac{\sigma_y(1-\nu)d}{E\Delta a}}. \tag{5.6b}$$

The stress distribution for any time t during deposition is

$$\sigma(z,t) = \sigma_y, \text{ when } z \le z_y \tag{5.7a}$$

and

$$\sigma(z,t) = \frac{E}{1-\nu}\frac{\Delta a}{k}\left(\frac{1}{z} - \frac{1}{Rt}\right). \text{ when } z > z_y. \tag{5.7b}$$

Evolution of the stress distribution is illustrated in Figure 5.9. Conditions here are similar to those in Figure 5.8. We additionally assume that the yield stress is 200MPa and the biaxial modulus is 140GPa.

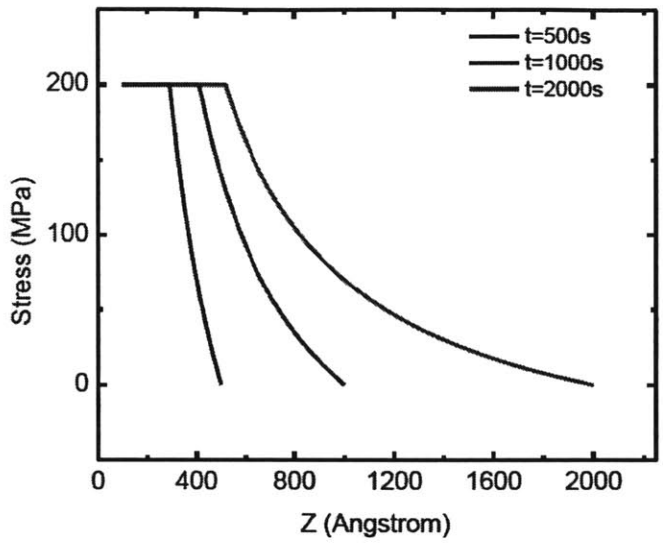

Figure 5.9. Evolution of stress distribution caused by grain growth. Basic assumptions: deposition rate is $1\mathring{A}/s$; the grain size to thickness ratio is $k=1$; yield stress is 200MPa; and biaxial modulus is 140GPa.

Because the stress level in the layers from $z=0$ to $z=z_y$ has reached the yield limit, the stresses in these layers will not increase due to grain growth. At any time t during deposition, only the layers from $z=z_y$ to $z=Rt$ become more tensile stressed and contribute to the change of the measured $(\frac{F}{w})$. Therefore, Equation (5.2) should be modified as

$$\Delta(\frac{F}{w})(t \to t+\Delta t) = \Delta\bar{\sigma}(t \to t+\Delta t)(h - z_y). \tag{5.8}$$

Combining Equation (5.1), (5.6b) and (5.8) gives rise to a modified expression for the instantaneous stress:

$$\sigma_{in}^{gg}(d) = \frac{E}{1-\nu}\frac{\Delta a}{d}(\frac{1}{1+\frac{E\Delta a}{(1-\nu)\sigma_y d}}). \tag{5.9}$$

Equation (5.9) is derived based on the assumption that $d \propto h$ during deposition. It can be proved that if the condition weakens to $d - d_0 \propto h$ (d_0 is a constant), the instantaneous stress caused by grain growth can still be described using Equation (5.9).

Let us discuss two scenarios for Equation (5.9). Scenario (1): the grain size is very small so that $d \ll \frac{E\Delta a}{(1-\nu)\sigma_y}$. Then Equation (5.9) can be simplified as

$$\sigma_{in}^{gg}(d) = \frac{E}{1-\nu}\frac{\Delta a}{d}(\frac{1}{1+\frac{E\Delta a}{(1-\nu)\sigma_y d}}) \approx \frac{E}{1-\nu}\frac{\Delta a}{d}(\frac{1}{\frac{E\Delta a}{(1-\nu)\sigma_y d}}) = \sigma_y. \tag{5.9*}$$

Scenario (2): the grain size is very large so that $d \gg \frac{E\Delta a}{(1-\nu)\sigma_y}$. Then Equation (5.9) can be simplified as

$$\sigma_{in}^{gg}(d) = \frac{E}{1-\nu}\frac{\Delta a}{d}\left(\frac{1}{1+\frac{E\Delta a}{(1-\nu)\sigma_y d}}\right) \approx \frac{E}{1-\nu}\frac{\Delta a}{d}\left(\frac{1}{1+0}\right) = \frac{E}{1-\nu}\frac{\Delta a}{d}. \qquad (5.9^{**})$$

For most metals, $\frac{E\Delta a}{(1-\nu)\sigma_y} \sim 50-100nm$. The above discussion shows that when the grain size is very small ($\ll 50nm$), the instantaneous stress caused by grain growth equals the yield stress of the film, and when the grain size is very large ($\gg 100nm$), Equation (5.9) is simplified to the general expression in Equation (5.3). This trend can be seen in Figure 5.10 (a), where we compare the instantaneous stresses caused by grain growth using Equation (5.3) and (5.9). When the film is thin, a significant portion of the layers in the film have yielded, so it is important to recognize the yielding effect on the stress distribution. As a result, Equation (5.9) should be employed. When the film becomes very thick, only the very bottom layers have reached the yield limit. These layers are negligible compared to the whole film, so the general (Equation (5.3)) and modified (Equation (5.9)) expressions become similar. Since we are studying the stress evolution in very thin films, we should use the modified expression rather than the general expression to estimate the instantaneous stress caused by grain growth during deposition.

The measured force per unit width at any film thickness H can be determined as

$$\frac{F}{w}(H) = \frac{F}{w}(H_c) + \int_{H_c}^{H} \sigma_{in}(h)dh. \qquad (5.10)$$

Here H_c is the coalescence thickness and $\frac{F}{w}(H_c)$ is the force per unit width at coalescence. In Figure 5.10 (b), we compare the resultant force per unit width based on Equation (5.3) and (5.9). Also shown is the *in situ* measured stress for a gold film.

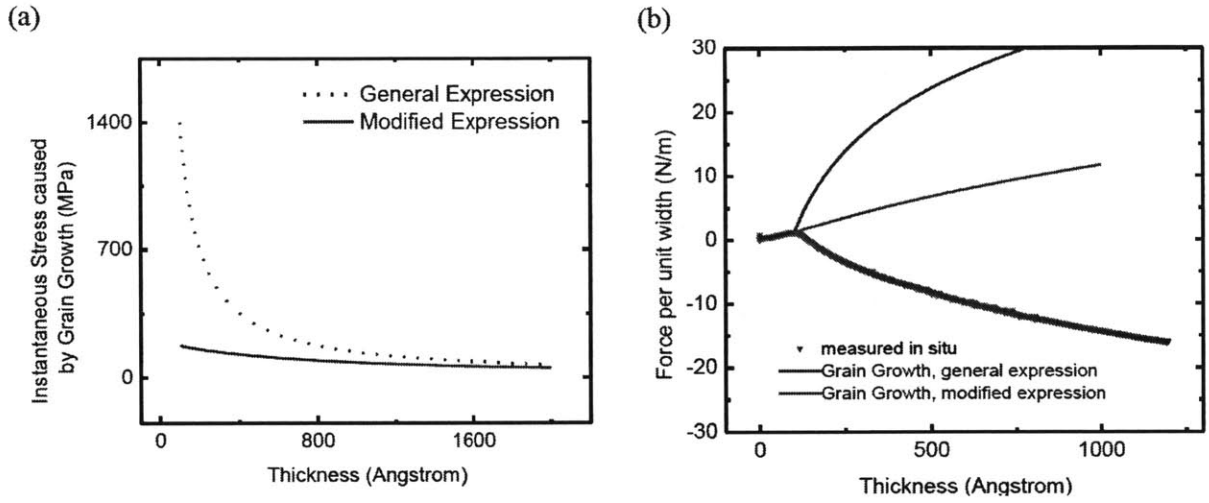

Figure 5.10. (a) Comparison of the instantaneous stresses caused by grain growth calculated using Equation (5.3) and (5.9). (b) Stress curve for a gold film deposited at 300K , along with the stress curves caused by grain growth during deposition using Equation (5.3) and (5.9).

Two important things should be noted. First, Figure 5.10 (b) shows that the deflection caused by grain growth is comparable to that measured *in situ.* It is thus of great importance to recognize the grain growth effect when modeling the compressive stress observed in Type II or the intermediate type behavior. In addition, we see the grain growth-related stress curves based on Equation (5.3) and Equation (5.9) differ significantly from each other. Because the

grain size right after coalescence is very small (~10nm or less), Equation (5.9) should be used in the modeling work.

5.3.4 CONSIDERATION OF OTHER STRESS SOURCES IN THE FILM

In Subsection 5.3.2 and 5.3.3, we discuss the simple case where grain growth is the only source for intrinsic stress during deposition. Unfortunately, this is never the case. In high atomic mobility systems, excess atoms in the grain boundaries can cause compressive stress. If this mechanism causes a compressive stress of $-\sigma_c(z)$ in the layer at z, the actual stress in this layer is

$$\sigma(z,t) = -\sigma_c(z) + \frac{E}{1-\nu}\frac{\Delta a}{k}\left(\frac{1}{z} - \frac{1}{Rt}\right) \tag{5.11}$$

Equation (5.11) describes the evolution of stress distribution when intrinsic stress is determined by both the compressive mechanism and grain growth during deposition. It reaches the yield limit when $\sigma(z,t) = -\sigma_c(z) + \frac{E}{1-\nu}\frac{\Delta a}{k}\left(\frac{1}{z} - \frac{1}{Rt}\right) = \sigma_y$. If $\sigma_c(z) \ll \sigma_y$, this leads to the same results in the previous subsections (Equation (5.9)). Otherwise, we can express $\sigma_c(z)$ in terms of the yield stress and a parameter $f(z)$, $\sigma_c(z) = f(z)\sigma_y, 0 \le f(z) < 1$. Using similar derivation procedures, we obtain the instantaneous stress caused by grain growth during deposition to be

$$\sigma_{in}^{gg}(d) = \frac{E}{1-\nu}\frac{\Delta a}{d}\left(\frac{1}{1+\frac{E\Delta a}{(1-\nu)(1+f)\sigma_y d}}\right) . \qquad (5.12)$$

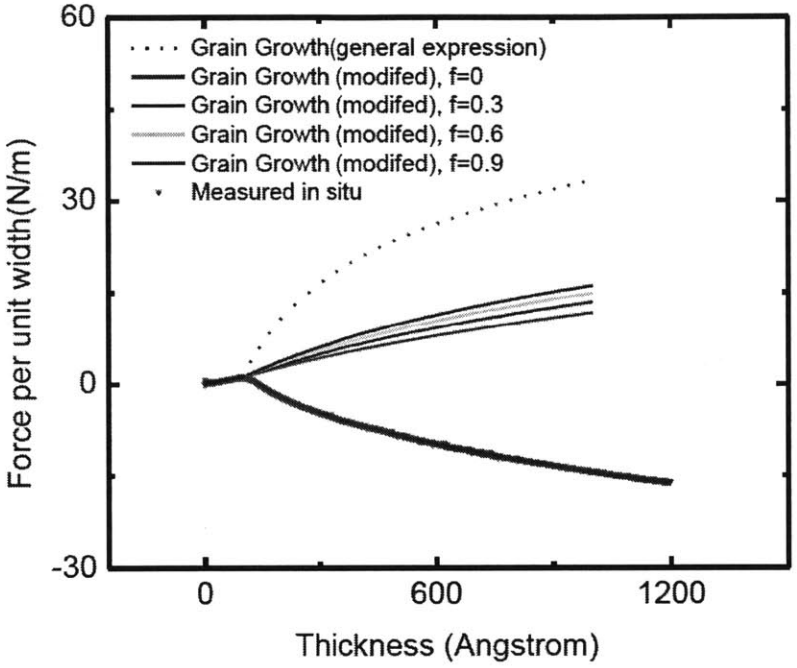

Figure 5.11. Stress caused by grain growth calculated using equation (5.3), (5.9) and (5.12), along with the stress of gold films measured *in situ*.

Figure 5.11 shows the stress evolution caused by grain growth during deposition, based on Equation (5.3), (5.9) and (5.12). Here we only calculate the simple cases where f is constant throughout the film. Clearly, the stress curves that take into account the strain gradient and yielding effect differ tremendously from the stress curve without such considerations (the blue dotted curve in Figure 5.11). The plots also show that the results taking into account the

compressive component (Equation (5.12), $f = 0.3, 0.6, 0.9$) only slightly deviate from the result assuming that grain growth is the only stress source (Equation (5.9), or $f = 0$).

In summary, we have analyzed the influence of grain growth on the intrinsic stress and stress distribution during deposition. We first derive a general expression for the instantaneous stress caused by grain growth (Equation (5.3)). Considering the strain gradient and the effect of yielding, we then obtain a modified expression for the instantaneous stress in Equation (5.9). Taking into account the sources of compressive stress in Equation (5.12) only leads to a small difference from the result calculated using Equation (5.9). Therefore, Equation (5.9) can be used to estimate the influence of grain growth on the instantaneous stress even if the magnitude and distribution of the compressive component are unknown.

5.4 INCORPORATION OF ADATOMS TO 2D ISLANDS AND TO GRAIN BOUNDARIES

Except for the presence of grain boundaries, postcoalescence polycrystalline growth is similar to homoepitaxial growth in which a single layer of atoms is often formed by nucleation, growth and coalescence of 2D islands (layer-by-layer mode)[15-18]. During film thickening, both the 2D island edges and the grain boundary (GB) surface sites are low chemical potential sites for adatom incorporation (see Figure 5.12(a)).

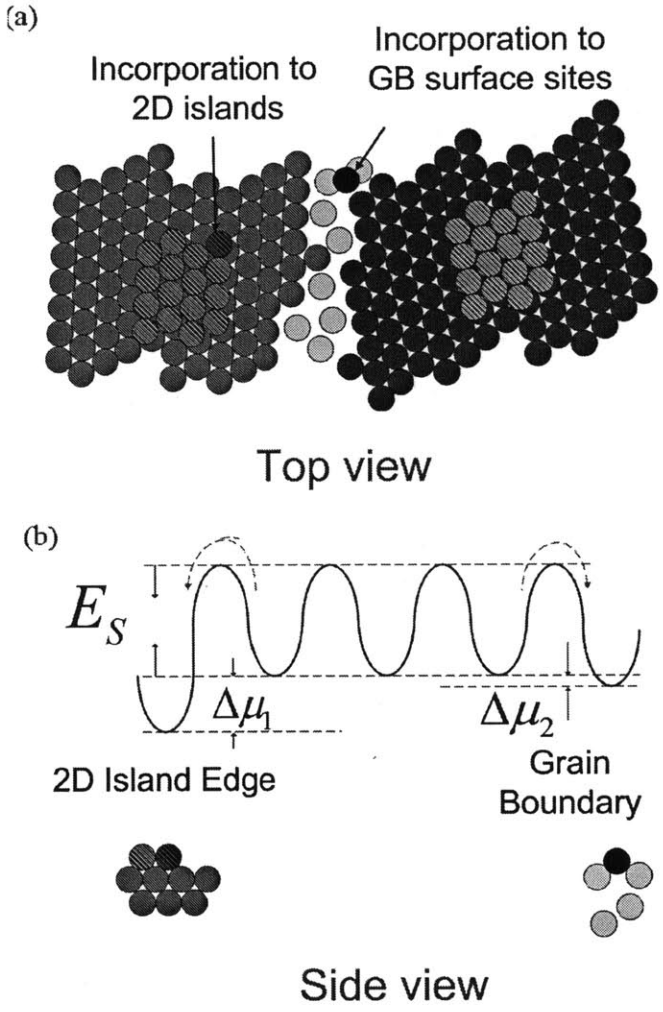

Figure 5.12. Mechanism for the compressive component of the intrinsic stress. (a) Illustration of the incorporation processes of adatoms to 2D islands and to GB surface sites. (b) Energy landscape for adatoms deposited between a 2D island and a grain boundary. $\Delta\mu_1$ and $\Delta\mu_2$ are the chemical potential differences between the grain surface sites and 2D island edges, and between the grain surface sites and GB surface sites, respectively.

Compared to the adatoms attaching to the 2D islands, the adatoms diffusing to GB surface sites form a less close-packed structure, and are in higher energy states with a better chance to jump back to the grain surface. As a result, most adatoms contribute to 2D island growth (i.e. film thickening), while only a small fraction contributes to adatom-GB incorporation. The corresponding energy landscape is shown in Figure 5.12 (b).

Multiple 2D islands could form on each grain's surface. Assuming δ is the distance between a GB and its neighboring 2D island, during deposition there is a capture zone of 2δ width (shown in Figure 5.13). Adatoms deposited outside this capture zone become part of the 2D islands before they can reach the grain boundary. Adatoms deposited inside the capture zone, are either captured by 2D islands or by GB surface sites, depending on the competition between 2D island growth and adatom-GB incorporation. We assume for the adatoms deposited inside the capture zone, the average probabilities of being captured by GBs and by 2D islands are p and $1-p$ ($p \ll 1$), respectively. For the adatoms deposited outside the capture zone, their probabilities of being captured by GBs and by 2D islands are 0 and 1. Therefore, for each grain, the ratio of the number of adatoms captured by GBs ($N_{adatom-GB}$) to the number of adatoms captured by 2D islands ($N_{adatom-2Disland}$) is

$$\frac{N_{adatom-GB}}{N_{adatom-2Disland}} = \frac{0\times(d-2\delta)+p\times 2\delta}{1\times(d-2\delta)+(1-p)\times 2\delta} \approx \frac{2p\delta}{d}. \qquad (5.13)$$

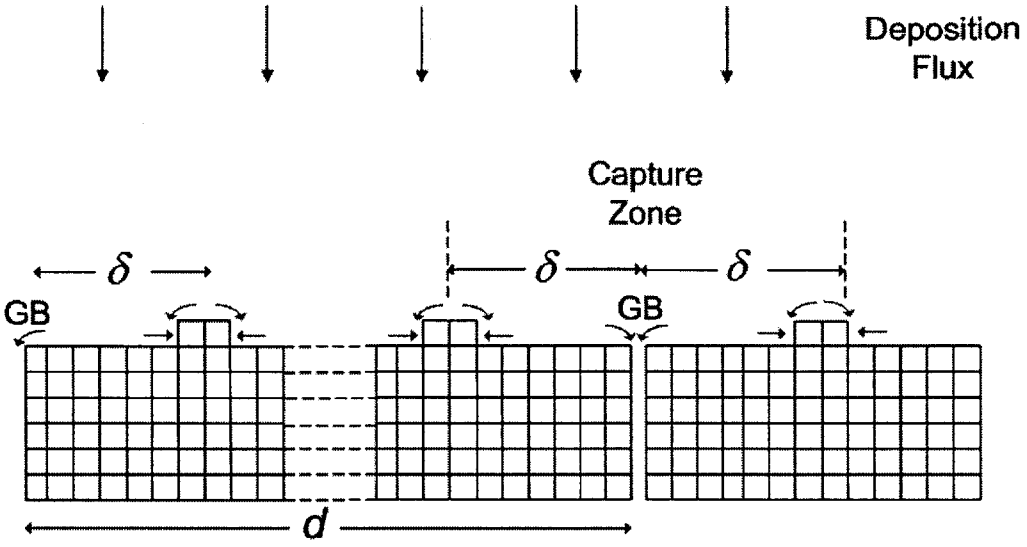

Figure 5.13. Illustration of the capture zone concept. The red and blue arrows refer to adatom incorporation in 2D islands and grain boundaries, respectively.

By definition, the value of δ cannot exceed the value of the 2D island spacing L_{island}. In other words, the value of δ ranges from 0 to L_{island}. Assuming a uniform distribution of the value of δ, the average distance between a GB and its neighboring island is $\bar{\delta} = L_{island}/2$. It has been suggested that excess atoms in grain boundaries can lead to compressive stress [3, 9]. Here the instantaneous stress caused by adatom-GB incorporation is

$$\sigma_{in}^{comp} = -M(\frac{2p\bar{\delta}}{d}) = -M(\frac{pL_{island}}{d}). \tag{5.14}$$

It should be noted that our model is different from that proposed by Chason and coworkers [9, 12, 19]. First, here the adatoms diffuse to the surface sites of GB but do not diffuse along GB.

Second, the rate of incorporation is controlled by the diffusion process on the film surface, and is not limited by the transition from surface into the GB.

Adatom dimers are stable under normal experimental conditions. In this case, the classical nucleation theory predicts the 2D island spacing to be [16-18]

$$L_{island} = a\eta^{-1/2}[(\frac{D_0}{Ra})e^{-E_s/kT}]^{1/6}, \tag{5.15}$$

where a is the lattice spacing; R is the deposition rate; D_0 and E_s are the diffusivity constant and energy barrier of adatom diffusion; and η is a dimensionless prefactor, whose maximum value has been estimated to be $\eta_{max} = 0.25$ [15]. At our experimental conditions, Equation (5.15) predicts the value of L_{island} in Ni films to be on the order of10nm, which is larger than the coalescence grain size measured in Figure 5.6. This means right after coalescence there is only one island forming on each grain surface. As a result, the entire grain surface is covered by the capture zone. For all the adatoms deposited on the grain surface, the average probabilities of being captured by grain boundaries and 2D islands are p and 1-p, respectively. Consequently, in this small grain size regime ($d < L_{island}$), the instantaneous stress caused by adatom-GB incorporation is

$$\sigma_{in}^{comp} = -M\frac{p}{1-p}, \tag{5.16}$$

which is independent of the grain size.

5.5 QUANTITATIVE COMPARISON BETWEEN THE MODELING AND EXPERIMENTAL RESULTS

5.5.1 EXPLANATION FOR THE STRESS TURNAROUND

So far, we have discussed two mechanisms for intrinsic stress generation: grain growth during deposition and adatom-GB incorporation on the film's surface. The grain growth mechanism changes the bulk stress of the film and causes a tensile component of the measured instantaneous stress. The adatom-GB incorporation process causes a compressive stress in the newly deposited layer on the film surface. The magnitude of this compressive stress changes from, being independent of, to scaling with, the inverse of the grain size as the film thickness increases so that the grain size increases from $(d < L_{island})$ to $(d > L_{island})$. Regarding the magnitude of the instantaneous stress, Equation (5.9) suggests the grain growth component (σ_{in}^{gg}) decreases slightly as the grain size increases; the compressive component (σ_{in}^{comp}) stays constant in the small grain size regime $(d < L_{island})$ but decreases rapidly in the large grain size regime $(d > L_{island})$. As a result, the overall instantaneous stress becomes less compressive during deposition, and eventually turns to tensile in the large grain size regime. This is why we see the stress turnaround. Because L_{island} increases at higher substrate temperatures or lower deposition rates, stress turns around in thicker films under such conditions (see Figure 5.3 and 5.4).

The above model can be further tested quantitatively with the experimental data for Ni films. First, we obtained the instantaneous stress (σ_{in}) from the plots in Figure 5.3 using

$\sigma_{in} = \frac{\Delta(\frac{F}{w})}{\Delta h}$. With the grain growth-related instantaneous stress (σ_{in}^{gg}) calculated using Equation (5.9), the compressive component can be then determined by $\sigma_{in}^{comp} = \sigma_{in} - \sigma_{in}^{gg}$. We did a series of calculations for the cases that the yield stress ranges from 450MPa to 750MPa (corresponding to $100 \pm 25\%$ of the maxium measured tensile stress) and the grain boundary width ranges from 0.5 Å to 1.0 Å[20]. In all these cases, two regimes are found in the σ_{in}^{comp} vs. $\frac{1}{d}$ plot. As can be clearly seen in Figure 5.14, when the grain size is small, σ_{in}^{comp} weakly depends on $\frac{1}{d}$ (flat regime); when the grain size becomes large, the magnitude of σ_{in}^{comp} decreases linearly with $\frac{1}{d}$ (linear regime). Another important feature to be noted is that when the films are deposited at higher temperatures, the boundary of the two regimes moves toward larger grain sizes (film thicknesses).

The results in Figure 5.14 are consistent with the model illustrated in Section 5.4. First, we see transition in behavior form being independent of d to scaling with 1/d as the grain size increases, as predicated by the model. In addition, when the substrate temperature is higher, this transition occurs in thicker films, and at larger grain sizes. According to our model, this is because the transition happens when $d = L_{island}$, and L_{island} increases with increasing substrate temperature.

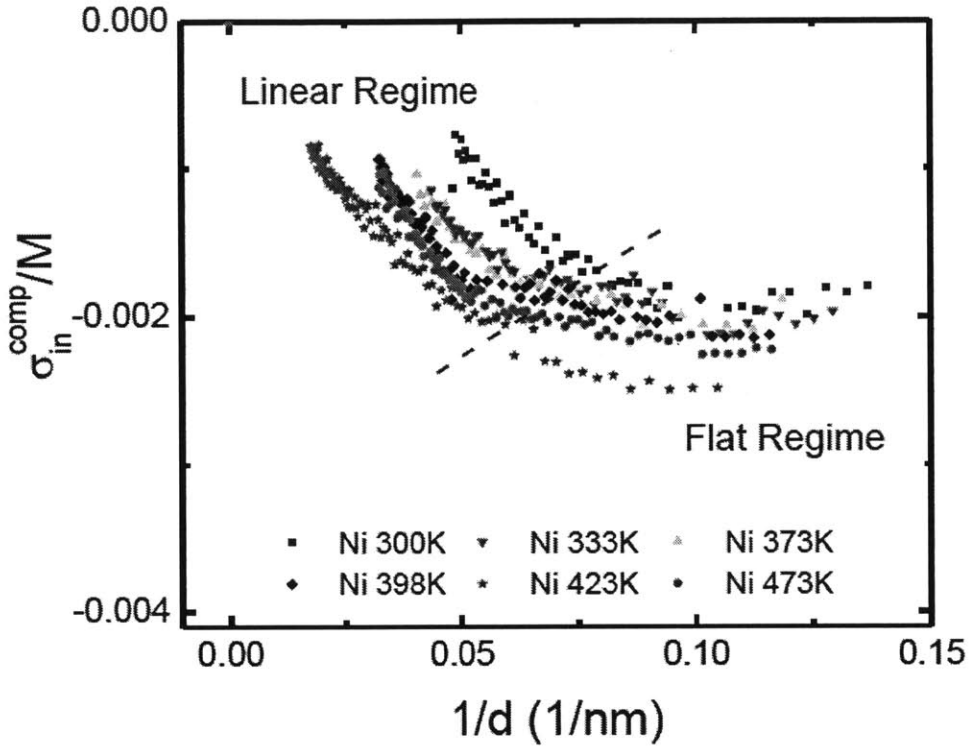

Figure 5.14. Plot of σ_{in}^{comp} as a function of $\frac{1}{d}$ based on the in situ measured data and Equation (5.9) (using $\Delta a = 1$ Å and $\sigma_y = 600MPa$).

In fact, by defining the boundaries of the flat regime and linear regime in Figure 5.14, we can determine the values of L_{island} during Ni film growth at different temperatures. As shown in Figure 5.15, L_{island} ranges from 12.2nm at 300Kto 19.9nm a 473K. These values are consistent with those calculated from Equation (5.15). The Arrhenius plot (inset) suggests that the effective activation energy of L_{island} is 0.035eV. Comparing with Equation (5.15), the activation energy for adatom diffusion is $E_s = 0.035 \times 6 = 0.21eV$. Adatom diffusion strongly

depends on the crystallographic orientation of the surface. (200) and (111) pole figure measurements show the as-deposited Ni films are (111) textured (Figure 4.9). Therefore, we conclude the activation energy for adatom diffusion on a (111) textured Ni film surface is $0.21eV$. This result is consistent with those obtained using other techniques. For example, using Field Ion Microscopy (FIM), Fu and Tsong[21]concluded that the activation energy for adatom diffusion on a Ni (111) surface is $E_s = 0.22 \pm 0.02eV$ and the diffusivity constant is $D_0 = 1 \times 10^{-9.2 \pm 0.7} m^2 / s$.

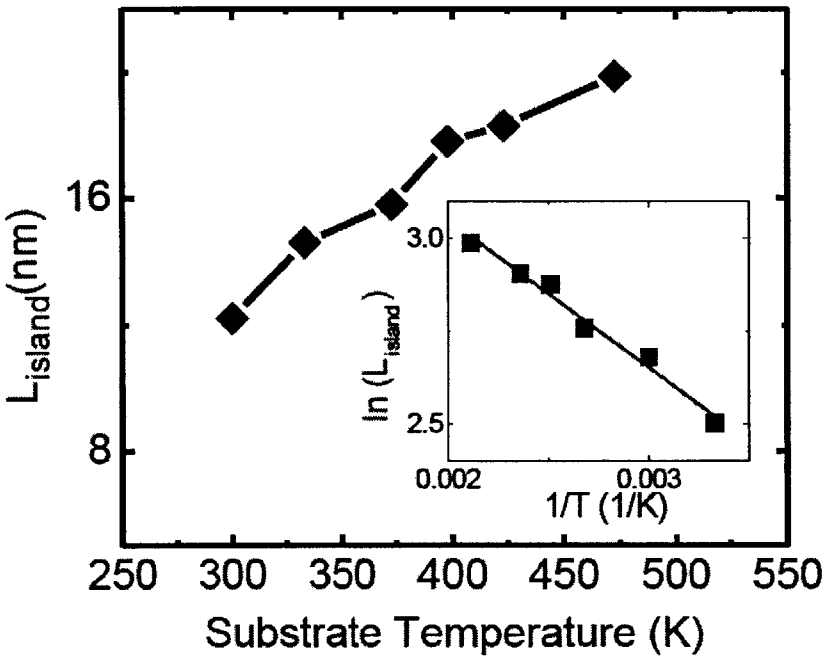

Figure 5.15. 2D island spacing as a function of the substrate temperature. Inset: the Arrhenius plot suggests that the activation energy for adatom diffusion on a (111) textured Ni film surface is $0.21eV$.

Now we summarize the modeling results in Section 5.3 and Section 5.4 as follows:

$$d \le L_{island}: \quad \sigma_{in} = \sigma_{in}^{comp} + \sigma_{in}^{gg} = \frac{E}{1-\nu}\frac{\Delta a}{d}\left(\frac{1}{1+\frac{E\Delta a}{(1-\nu)\sigma_y d}}\right) - M\frac{p}{1-p}, \tag{5.17a}$$

and

$$d > L_{island}: \sigma_{in} = \sigma_{in}^{comp} + \sigma_{in}^{gg} = \frac{E}{1-\nu}\frac{\Delta a}{d}\left(\frac{1}{1+\frac{E\Delta a}{(1-\nu)\sigma_y d}}\right) - M\frac{pL_{island}}{d}. \tag{5.17b}$$

Figure 5.16 shows the stress evolution in Ni films predicted using Equation (5.17) under different conditions. The temperature dependence can be seen in the plots at 300K +0.5Å/s, 373K +0.5Å/s and 473K +0.5Å/s. The deposition rate dependence can be seen in the plots at 373K +0.3Å/s, 373K +0.5Å/s and 373K +0.8Å/s. Here the precoalescence parts of the curves are based on the measured data. Clearly, the model captures all the important features of the *in situ* measured results in Figure 5.3, including stress turnaround, the dependence of the stress turnaround thickness on the substrate temperature and deposition ate, and the curvature of the stress curves. In the inset, we plot the average stress at the turnaround point as a function of the turnaround thickness under these conditions. The modeling results almost coincide with the experimental data in all cases.

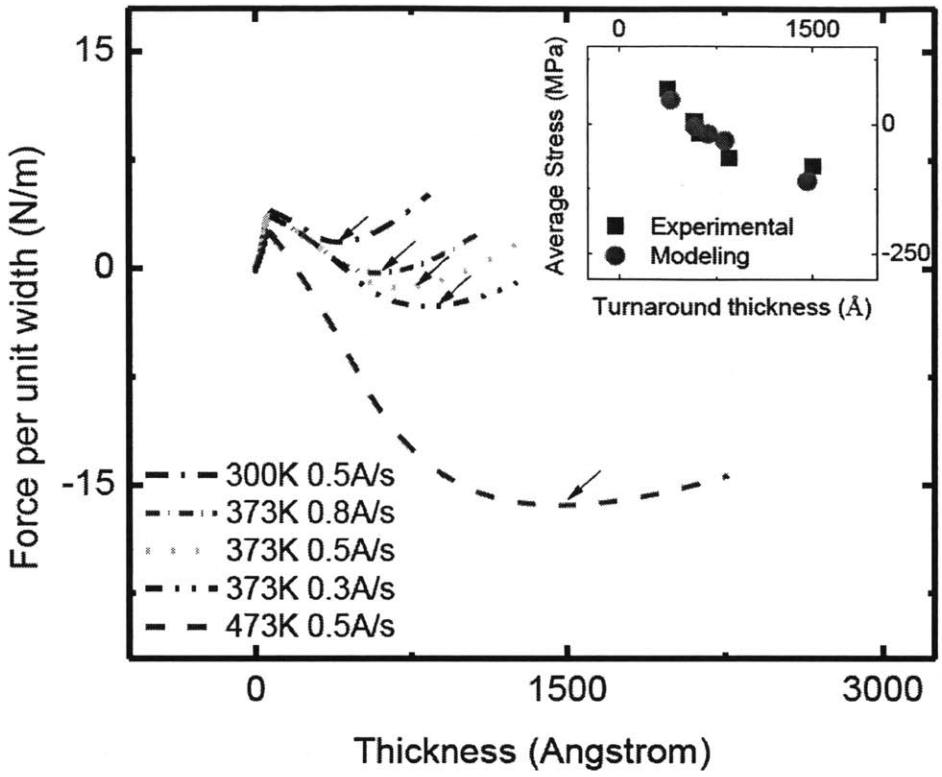

Figure 5.16. Comparison between the model and experiment. Stress curves for Ni films predicted using Equation (5.17), at substrate temperatures of 300K, 373K, 473K and deposition rates of 0.3Å/s, 0.5 Å/s, 0.8 Å/s. Inset: the average stress and the thickness at the turnaround point under such conditions for the model (squares) and experiments (circles). The parameter values used in the model are $E_s = 0.21eV$, $D_0 = 1\times10^{-9.2} m^2/s$ **(based on FIM experiment [21]);** $\Delta a = 1$ **Å,** $\sigma_y = 600MPa$, $\eta = 0.19 (< \eta_{\max} = 0.25)$ **[15] and** $p = 0.002$.

5.5.2 EXPLANATIONS FOR TYPE I AND TYPE II STRESS BEHAVIOR

Nix and Clemens [3] suggested that epitaxial inheritance of the coalescence stress can lead to a constant tensile stress during film thickening. This mechanism only weakly affects the shapes of the stress curves at high and intermediate homologous temperatures. At low homologous temperatures, however, it becomes the dominant mechanism because both grain growth and adatom diffusion are suppressed. As a result, a constant tensile stress is observed under conditions of low atomic mobility, as shown for Pt in Figure 5.17. This is true even if the adatom-GB incorporation process is not completely turned off. In that case, the compressive component is constant but small compared to the tensile coalescence stress.

Also shown in Figure 5.17 are the instantaneous stress evolution in the intermediate type (Ni at 300K and 373K) and Type II (Au and Cu at 300K), in which a flat regime and a linear regime can be roughly seen in this σ_{in} vs. $\frac{1}{h}$ plot. Because the grain growth-related instantaneous stress changes weakly with $\frac{1}{h}$ (Equation 5.9), this indicates that the compressive component in Type II systems can also be divided into two regimes: a flat regime when the grain size is small and a linear regime when the grain size is large.

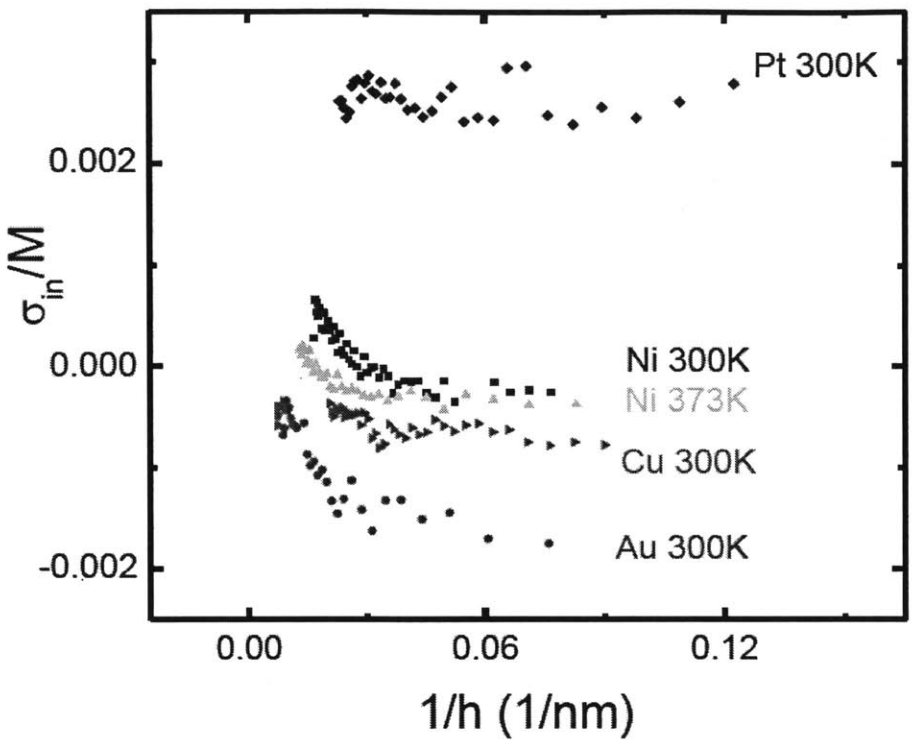

Figure 5.17. Plot of instantaneous stress as a function of the inverse of the film thickness, for all three types of stress behaviors.

In Type II systems, because the 2D island spacing L_{island} is large, the transition from the flat regime to the linear regime only occurs at a very large film thickness. However, *in situ* stress measurements are usually limited to film thicknesses of ~100-200nm. As a result, stress turnaround is generally not observed in Type II systems. Our recent experiments show that for Au films deposited at 300K with a deposition rate of 1nm/s, a stress turnaround can be seen when the film thickness exceeds $1.5\mu m$ (see Figure 5.18).

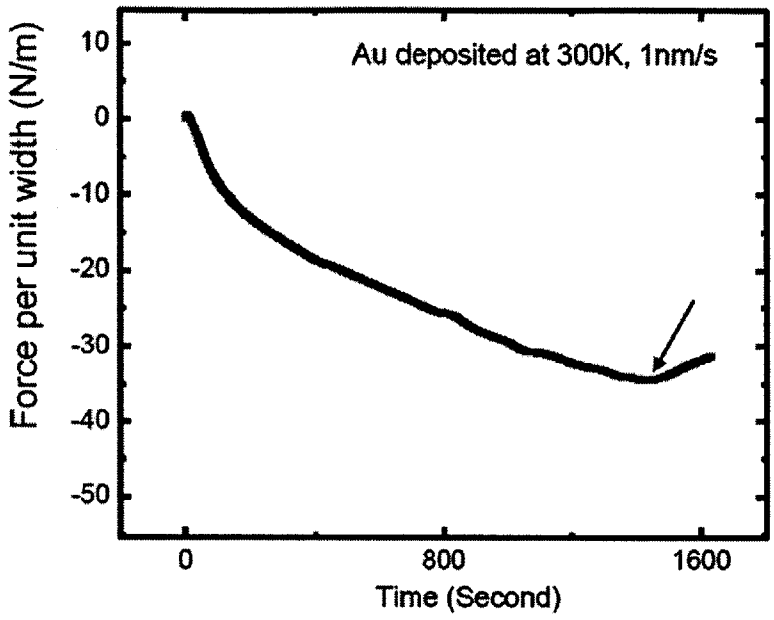

Figure 5.18. Stress turnaround in a Au film deposited at 300K, with a deposition rate of 1nm/s.

5.6 STRESS EVOLUTION DURING A GROWTH INTERRUPTION AND UPON RESUMPTION OF GROWTH IN THE INTERMEDIATE REGIME

In the previous sections, we have shown that the stress turnaround phenomenon observed of the intermediate type can be explained by grain growth during deposition and adatom-GB incorporation on the film surface. These two mechanisms are also the dominant mechanisms for postcoalescence stress evolution in Type II systems. In this section, we discuss the stress evolution during growth interruption and upon resumption in the intermediate regime. Such stress evolution in Type II systems has been investigated in Chapter 4.

Figure 5.19 shows the stress evolution in a Ni film deposited at 398K with five short interruptions during growth. The stress evolution of such film without growth interruptions has been shown in Figure 5.3. Before the minimum of the stress curve, the instantaneous stress is compressive, and the stress change during an interruption is toward the tensile direction. This change is reversible upon growth resumption as the stress rapidly returns to the pre-interruption stress evolution trajectory. After the minimum of the stress curve, the instantaneous stress is tensile, and the stress change during an interruption is also tensile. The instantaneous stress is compressive upon growth resumption, but turns around quickly to tensile during subsequent film thickening.

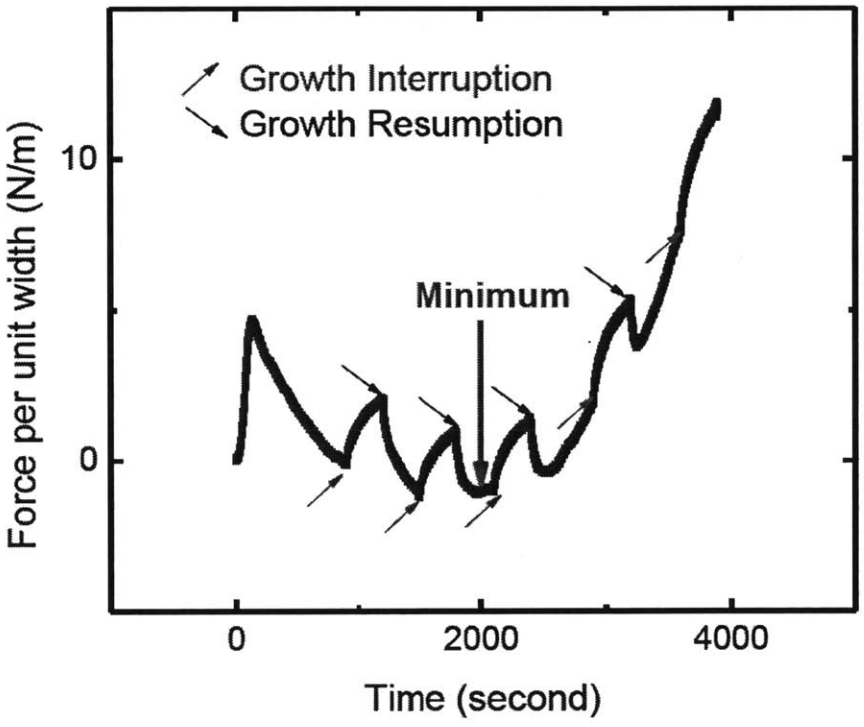

Figure 5.19. Stress evolution in a Ni film deposited at 398K and 0.5Å/s, with growth interruptions and resumptions before and after the minimum of the stress curve.

To summarize, no matter whether the growth is interrupted before or after the minimum of the stress curve, the stress change during an interruption is always toward the tensile direction and the stress upon growth resumption is always toward the compressive direction. This reversible interruption-resumption behavior is similar to what has been seen in Type II systems. The only difference here is that if the pre-interruption instantaneous stress is tensile, the stress is compressive upon resumption but changes to tensile afterwards, leading to compressive dips in the stress curves.

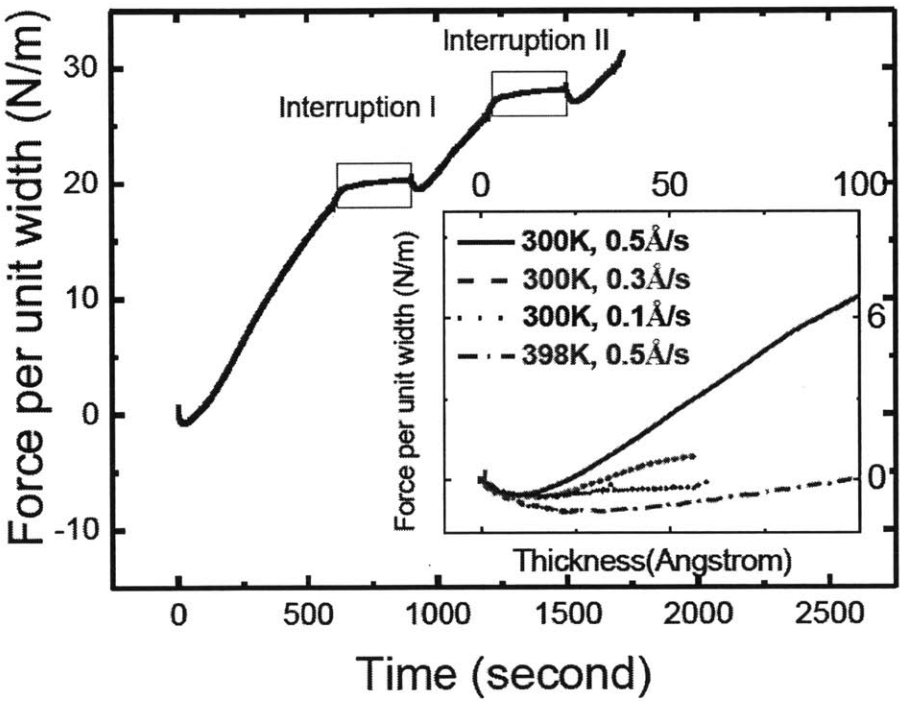

Figure 5.20. Compressive dips upon growth resumptions in Ni films deposited at 300K. The substrate is a 80nm thick Ni film on silicon. Inset: Temperature and deposition rate dependence of the compressive dip.

Figure 5.20 shows the stress evolution in Ni films deposited at 300K on 80nm Ni films. A compressive dip is seen as the growth is started. After that, the stress rapidly changes to tensile, and shifts towards the tensile direction during the subsequent two interruptions. Another two compressive dips are seen upon the two growth resumptions. The inset in Figure 5.20 shows that the compressive dip becomes wider and deeper as the temperature increases or the deposition rate decreases. This is consistent with the temperature and deposition rate dependence of the stress turnaround phenomenon.

The results in Figure 5.19 and Figure 5.20 can be well explained based on the content in this chapter and Chapter 4. In this chapter, we have shown that the adatom-GB incorporation process on the film surface leads to a compressive stress in the surface layer in the film. The grain growth process during deposition makes the bulk of the film less compressive or more tensile, giving rise to a stress gradient throughout the film. After the minimum of the stress curve, while the measured instantaneous stress is tensile, the stress in the surface layer is still compressive, and the bottom layers of the film are tensily strained (see Figure 5.21(a)).

In Chapter 4, we have shown that the stress change during short interruptions and upon growth interruptions is associated with the reversible change of the surface structure of the film. Speficially, the grooving process during a growth interruption can lead to relaxation of the stresses in the surface layers. Because the stress in the surface layer is always compressive, the stress change during a short interuption is always in the tensile direction. After the growth is resumed, the dyanmic surface morphology is reestablished so that compressive stresses are rebuilt in the surface layers (see Figure 5.21(b)).

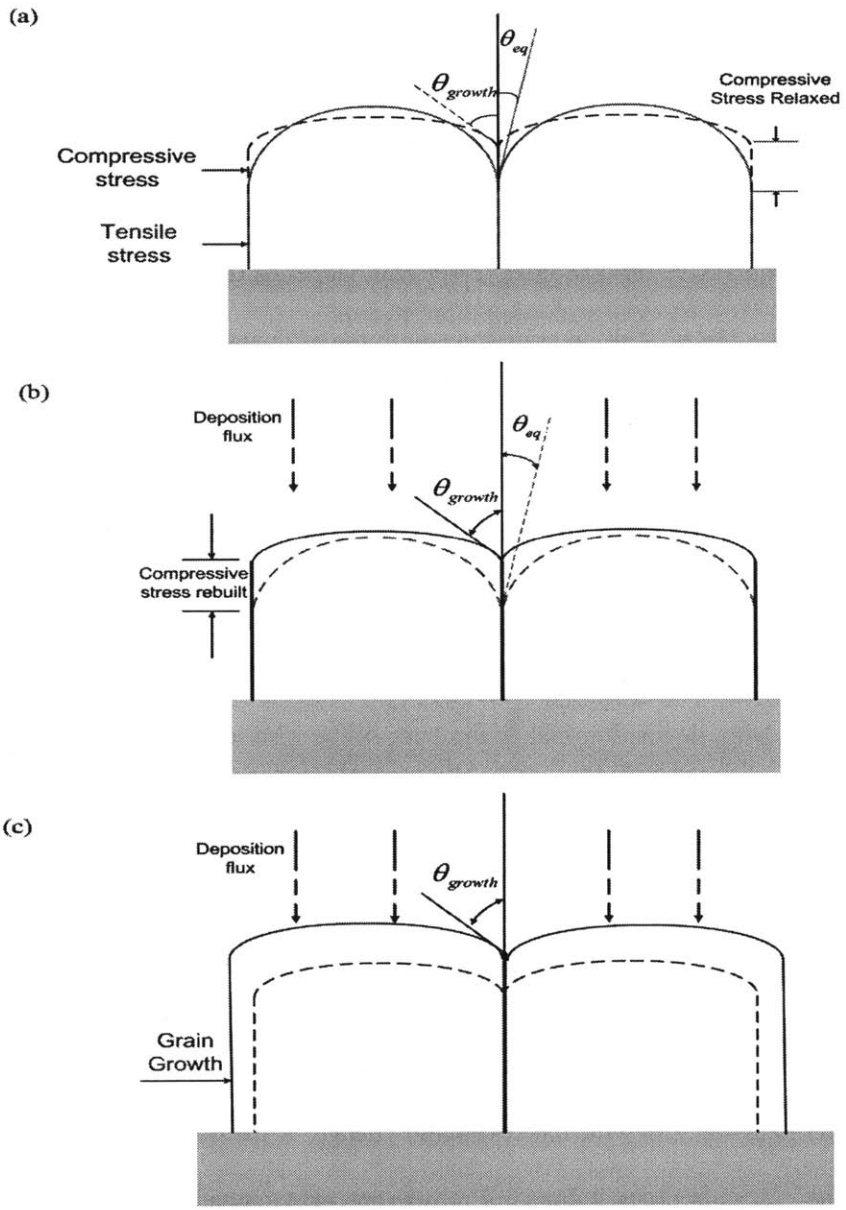

Figure 5.21. Illustration of the stress evolution during growth interruptions and upon resumptions in the intermediate type. (a) compressive stress relaxation during an interruption. (b) compressive stress is rebuilt upon growth resumption. (c) further film thickening leads to grain growth and the stress turnaround phenomenon.

Further film thickening leads to an increase of the grain size and a tensile component of the instantaneous stress. As a result, the instantaneous stress becomes less compressive and eventually turns around to become more tensile (see Figure 5.21(c)). This is why we see compressive dips after the growth is resumed. Because the compressive stress caused by adatom-GB incorporation is favored at higher temperatures or with lower deposition rates, the compressive dips are wider and deeper under such conditions.

5.7 SUMMARY

We have discovered a new stress behavior in Volmer-Weber systems with intermediate atomic mobility. The intermediate type stress behavior is characterized by the stress turnaround phenomenon that strongly depends on substrate temperature and deposition rate. Type I, the intermediate type and Type II stress behavior are observed in systems of low, intermediate and high atomic mobility, respectively.

The Hoffman-Nix-Clemens mechanism is the origin of the pre-coalescence tensile stresses in Type I, Type II and the intermediate type behavior. After coalescence, grain growth during deposition and excess adatoms trap in the grain boundaries are two general mechanisms for stress evolution in the intermediate type and Type II systems. The increase of grain size has two consequences. First, it changes the bulk stress of the film during deposition and causes a tensile component of the instantaneous stress. Second, it changes the grain size dependence of the compressive component of the stress, the magnitude of which is controlled by the competition between adatom-2D island incorporation and adatom-GB incorporation. Under conditions of low atomic mobility, epitaxial inheritance is the major mechanism for

postcoalescence growth. No stress change is observed during interruptions of growth in Type I systems. For the intermediate type and Type II systems, a reversible interruption-resumption behavior has been observed during short interruptions. This reversible behavior is associated with the grooving process during short interruptions and the reestablishment of the dynamic surface morphology upon growth resumption. Grain growth dominates the stress change during long interruptions in Type II systems. For the intermediate type behavior, the magnitude of the stress change during long interruptions strongly depends on temperature. For example, the stress change is substantial in nickel films deposited at 473K, but is negligible in nickel films deposited at 300K (see Subsection 4.3.1). The stress change in the former case has also been attributed to grain growth. Figure 5.22 shows a zone model diagram for the intrinsic stress evolution based on the results in Chapter 4 and Chapter 5.

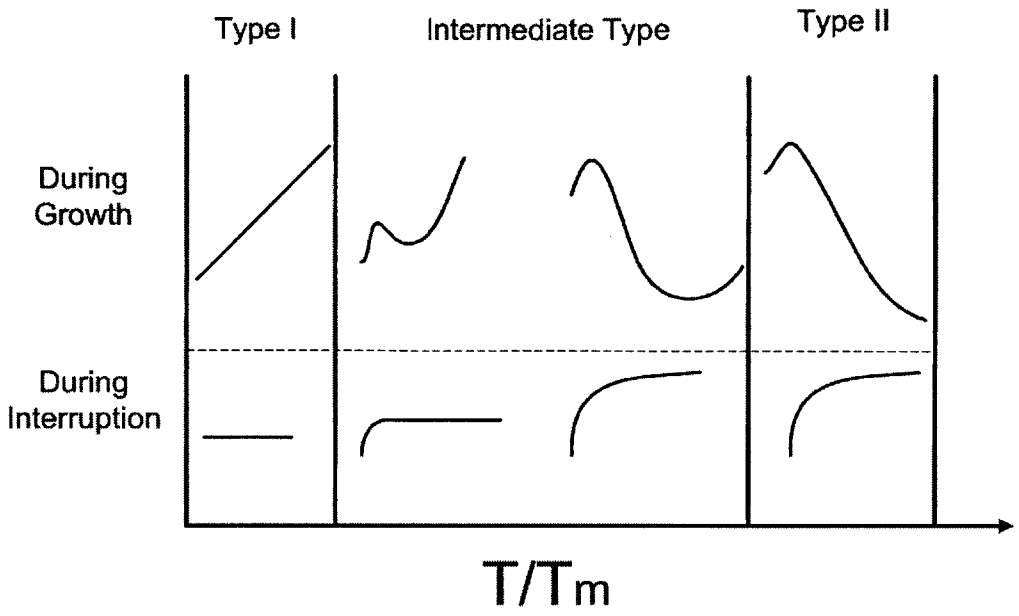

Figure 5.22. Zone model diagram for the intrinsic stress evolution in polycrystalline films.

In Table 5.2, we summarize the stress behaviors and the underlying mechanisms during growth and during growth interruptions for all types of Volmer-Weber systems. The transition from Type I to the intermediate type to Type II is continuous and can be accomplished by changing kinetic conditions, e.g. increasing substrate temperatures or decreasing deposition rates.

Stress Type	Type I	Intermediate Type	Type II
During coalescence	Tensile		
Major mechanism	Hoffman-Nix-Clemens Mechanism		
After coalescence (up to film thickness ~100-200nm)	Tensile	From Compressive to Tensile	Compressive
Major mechanism	Epitaxial inheritance from coalescence	Grain growth during deposition and extra adatoms trapping in the grain boundaries	
During short growth interruptions	N/A	Reversible interruption-resumption behavior	
Mechanism	N/A	Grooving process facilitated by surface diffusion	
During long growth interruptions	N/A	Negligible Change (Ni 300K)	Substantial Change
		Substantial Change (Ni 473K)	
Mechanism	N/A	Grain Growth	
Representative Systems	Ti, Fe, Cr, Pt at 300K	Pd at 300K; Ni from 300K to 473K.	Au, Ag, Cu at 300K

Table 5.2. Summary of the stress behaviors, underlying mechanisms and representative systems in all the temperature regimes.

REFERENCES

[1] R. Koch, Journal of Physics-Condensed Matter 6, pp. 9519 (1994).

[2] J. A. Floro, E. Chason, R. C. Cammarata, and D. J. Srolovitz, Mrs Bulletin 27, pp. 19 (2002).

[3] W. D. Nix, and B. M. Clemens, Journal of Materials Research 14, pp. 3467 (1999).

[4] R. W. Hoffman, Thin Solid Films 34, pp. 185 (1976).

[5] L. B. Freund, and E. Chason, Journal of Applied Physics 89, pp. 4866 (2001).

[6] S. C. Seel, and C. V. Thompson, Journal of Applied Physics 93, pp. 9038 (2003).

[7] F. Spaepen, Acta Materialia 48, pp. 31 (2000).

[8] C. Friesen, and C. V. Thompson, Physical Review Letters 89 (2002).

[9] E. Chason, B. W. Sheldon, L. B. Freund, J. A. Floro, and S. J. Hearne, Physical Review Letters 88 (2002).

[10] R. Koch, D. Z. Hu, and A. K. Das, Physical Review Letters 95 (2005).

[11] R. Koch, D. Z. Hu, and A. K. Das, Physical Review Letters 94 (2005).

[12] E. Chason, J. W. Shin, S. J. Hearne, and L. B. Freund, Journal of Applied Physics 111 (2012).

[13] Chaudhar.P, Journal of Vacuum Science & Technology 9, pp. 520 (1972).

[14] C. V. Thompson, and R. Carel, Journal of the Mechanics and Physics of Solids 44, pp. 657 (1996).

[15] J. A. Venables, G. D. T. Spiller, and M. Hanbucken, Reports on Progress in Physics 47, pp. 399 (1984).

[16] H. Brune, Surface Science Reports 31, pp. 121 (1998).

[17] A. Pimpinelli, and J. Villain, *Physics of crystal growth* (Cambridge University Press, Cambridge, U.K. ; New York, 1998), Collection Aléa-Saclay, 4.

[18] T. Michely, and J. Krug, *Islands, mounds, and atoms : patterns and processes in crystal growth far from equilibrium* (Springer, Berlin ; New York, 2004), Springer series in surface sciences,, 42.

[19] J. S. Tello, A. F. Bower, E. Chason, and B. W. Sheldon, Physical Review Letters 98 (2007).

[20] H. J. Frost, F. Spaepen, and M. F. Ashby, Scripta Metallurgica 16, pp. 1165 (1982).

[21] T. Y. Fu, and T. T. Tsong, Surface Science 454, pp. 571 (2000).

CHAPTER 6

EFFECT OF EVAPORANT INCIDENCE ANGLE ON STRESS AND STRUCTURE EVOLUTION DURING POLYCRYSTALLINE FILM GROWTH

6.1 INTRODUCTION

In Chapter 4 and Chapter 5, we have systematically studied the stress behaviors and the underlying mechanisms during and after growth of polycrystalline films in all temperature regimes. In addition to surface diffusion and grain growth, we expected that the angle of incidence of the evaporant flux would significantly affect stress evolution because of its influence on the surface morphology and grain structure during film deposition. The observed effects of the incidence angle on the evolution of intrinsic stress, surface structure and grain structure are the focus of this chapter.

A brief literature review is presented in Section 6.2, with an emphasis on the influence of two geometrical effects on surface morphology evolution. In Section 6.3, we show experimental data on the intrinsic stress evolution in gold and nickel films during oblique angle depositions. Two trends are found in the stress evolution curves. First, the thickness at which the tensile peak is observed increases with incidence angles. This can be attributed to the shadowing effect, which leads to preferential condensation of atoms on the tops of the islands, and therefore a delay of the coalescence process. The second trend is that the stress becomes less

compressive or more tensile when the film is deposited at a higher incidence angle. We discuss the origin of the second trend based on the experimental results in Section 6.4 and the analysis in Section 6.5.

The characterization work in Section 6.4 shows that the surface roughness increases significantly with the incidence angle. At a given angle, both the dome height of individual grains and the grain size increase with film thickness. At a given film thickness, the grain size slightly decreases at higher incidence angles, shown here for Ni deposited at 45°. In Section 6.5, we show that the difference in the grain sizes of the 0° and 45° deposited Ni films only leads to a small difference in the instantaneous stresses. Therefore, the change in the measured intrinsic stress at higher angles mostly originates from the change of the adatom-GB trapping process. Our analysis shows that the adatom-GB incorporation process is significantly suppressed by the shadowing effect and the enhanced surface roughness during oblique angle deposition. Since both effects become more important at higher incidence angles, the compressive stress decreases as the incidence angle increases. The findings in this chapter are summarized in Section 6.6.

6.2 OBLIQUE ANGLE DEPOSITION

The surface morphology of a continuous polycrystalline film is often determined by the nucleation of 2D islands, adatom diffusion on terraces on the surfaces of individual grains, and adatom attachment to 2D islands on those surfaces. In particular, the surface roughness is significantly influenced by the presence of Ehrlich-Schwoebel barriers [1, 2], which suppress

diffusion over descending steps. The atomic mobility, or the homologous temperature of the system, plays an important role in these diffusional processes.

During oblique angle deposition, geometrical effects, such as the shadowing effect and the steering effect [3-5], can also signficantly influence the surface morphology and grain structure of the film. Because of the shadowing effect (see Figure 6.1(a)), the atom flux is preferentially captured by the higher surface sites of the film. This can lead to a rough film surface and 3D defects (e.g. voids) in the bulk of the film. At high temperatures, surface diffusion can help to fill the voids and smooth the surface. At low temperatures, surface diffusion is suppressed so that the surface morphology is mostly determined by the location where the atomic flux condenses. Moreover, due to the short-range attraction between the substrate and the atom flux, the atomic trajectory can deviate significantly from the original one as the atoms approach a surface from an oblique angle (see Figure 6.1(b)). This is known as the steering effect, which was first demonstrated by Sanders *et al.* [6] using molecular dynamics calculations and later by Poelsema *et al.* [3] using experimental evidence. The steering effect gives rise to a redistribution of the incident atoms according to their morphology-dependent trajectories. As a result, the atoms arrive preferentially on protruding terraces. Both the shadowing effect and the steering effect lead to an enhancement of the surface roughness during deposition.

Therefore, the surface morphology and grain structure of films deposited from an oblique angle are controlled by a competition between the geometrical effects and surface diffusion processes. Under conditions of high atomic mobility and low incidence angles, the growth process is dominated by the surface diffusion processes. Under conditions of low atomic

mobility and high incidence angles, the growth process is dominated by the geometrical effects.

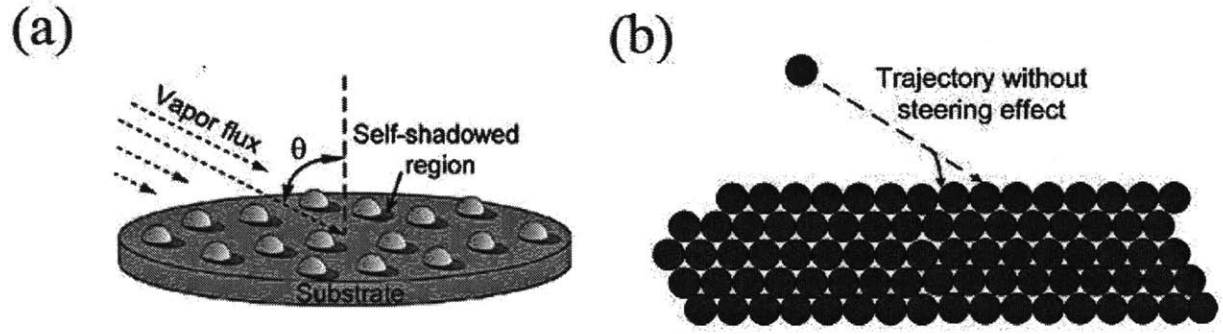

Figure 6.1. Illustration of (a) shadowing effect [7] and (b) steering effect. In (b), the dashed blue line and the solid red line represent the atom trajectory without and with the steering effect, respectively.

When the temperature is low enough and the angle of the incident beam (α) is high, growth from an oblique angle can lead to tilted columns growing toward the direction of the vapor source [8-13], as shown in Figure 6.2. The size of the column is also determined by the adatom mobility of the material and by the deposition conditions. Higher adatom mobility and higher temperature lead to larger-diameter columns. Early research on oblique angle deposition has focused on the relation between the orientation of the columnar structures and the deposition parameters. It has been generally found that the column tilt angle α_{column} is less than the deposition angle α. Many attempts have been made to qualitatively or quantitatively explain the tilt angle. In 1966, Nieuwenhuizen and Haanstra [13] presented TEM images for films grown by oblique angle deposition and proposed the relationship [12]

$$\tan\alpha = 2\tan\alpha_{column}. \tag{6.1}$$

Rather than being derived from basic principles, Equation (6.1) provides an empirical relation that correlates well with experimental data in the literature.

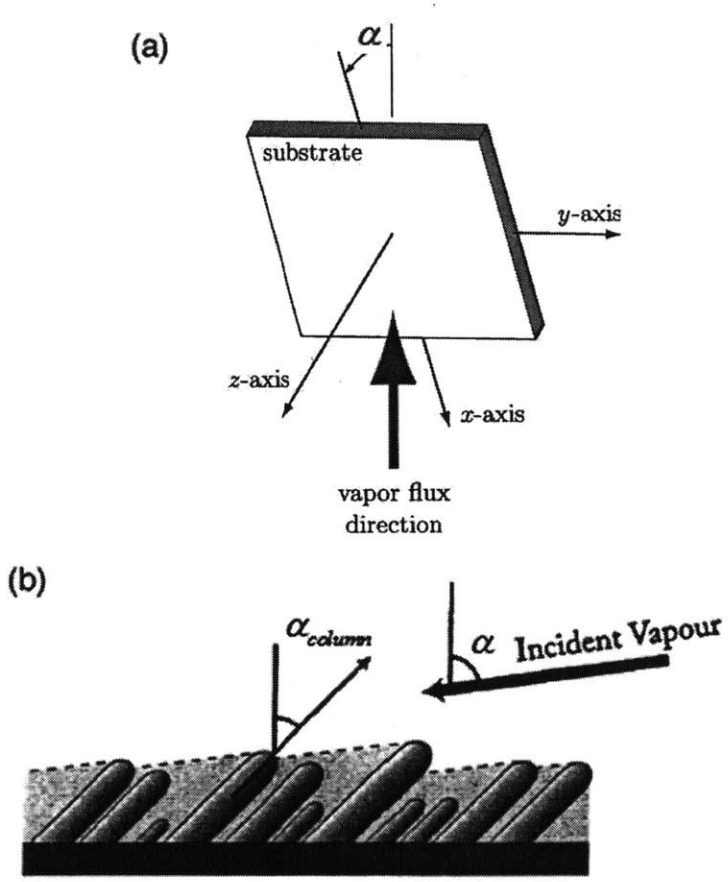

Figure 6.2 (a) Geometry of oblique angle deposition. [11] (b) Orientations of the tilted columns and the incident beams [12].

Complex nano-columnar structures [8-10] can be fabricated when the growth process is dominated by extreme geometrical effects, e.g. as obtained at glancing angles > 80°. If the substrate rotates during deposition, the orientation of the columns changes with time and film thickness. By adjusting the relation between the rotation speed and deposition rate, multiple microstructures can be produced. Figure 6.3 shows examples of nanostructured thin films fabricated using this method. The film consisting of tilted columns in (a) was fabricated by conventional oblique angle deposition without substrate rotation. By rapidly rotating the substrate 180° at a fixed frequency, a chevron film was fabricated in (b). In (c), a helical film was fabricated by continually rotating the substrate at a slow rate. If the rotation rate is too high, the helical structure will degenerate into a vertical post structure such as shown in (d). It should be noted that the stress and structure evolution in these complex structures are beyond the scope of this thesis. In the following sections, we study the stress and structure evolution in Ni films deposited at 0-45°and Au films deposited at 0-60°, both at room temperature. Under such conditions, the films are continuous so that the framework developed in previous chapters can still be used.

The angle of incidence of the flux also affects the surface evolution during growth of single-crystal and amorphous films. For example, in homoepitaxial growth of Cu films on a Cu (100) substrate at 250K, a gradual transition was observed from symmetric mound structures with side angles up to 55 degree to asymmetric mounds with increasing slopes up to 70 degree [15-18]. For oblique angle deposition of amorphous films, Mayr , Samwer and coworkers [19, 20] found that the typical hill size grows with film thickness, and that the surface roughness increases with incidence angles. These two features are similar to those observed in polycrystalline film growth.

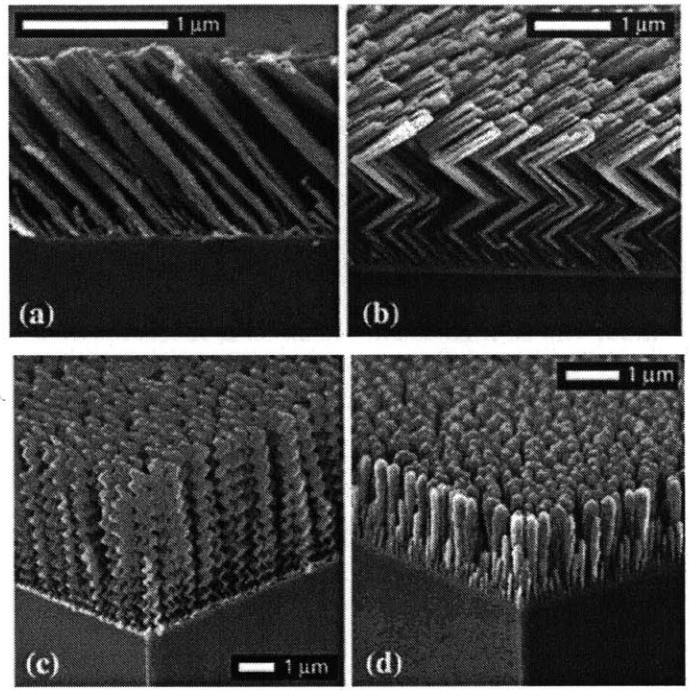

Figure 6.3. Various microstructures of thin films grown by oblique angle deposition. (a) tilted columns, (b) zig-zag structures, (c) helical structures and (d) array of nanorods [14].

To sum up, geometrical effects (mostly the shadowing effect) play important roles in developing surface roughness during oblique deposition of single-crystal, polycrystalline and amorphous films. The influence of these effects is more important at lower temperature, in which diffusion based surface relaxation processes are less efficient. At sufficiently low temperatures and high incidence angles, the typical grain structure is replaced by isolated nano-columns, the orientation of which is mostly determined by the angle of incidence of the flux.

6.3 STRESS EVOLUTION DURING OBLIQUE ANGLE DEPOSITION OF GOLD AND NICKEL FILMS

In Section 6.2, we have briefly reviewed the effect of the angle of incidence of the atom flux on the growth process of polycrystalline films. In this section, we discuss how the incidence angle can affect the intrinsic stress evolution in Ni and Au films. We have fabricated a tiltable stress sensor for *in situ* stress measurements during oblique angle deposition, as shown in Chapter 3. Inside the vacuum chamber, the sensor set-up is mounted onto the stage with the back plate (see Figure 3.4) contacting the stage. To be able to tilt from 0 to 90 degree, the stress sensor is not fully in contact with the back plate. Under conditions of ultra high vacuum, this limits the thermal conduction between the stress sensor and the sample stage. For this reason, all the stress measurements have been carried out at room temperature. Figure 6.4 (a) illustrates the way we measure the stress evolution during oblique angle deposition. Here α refers to the angle of the incident flux. Figure 6.4 (b) shows results for Au films with incidence angles of 30, 45, 52, 60° and Ni films with incidence angles of 15, 30, 45°.

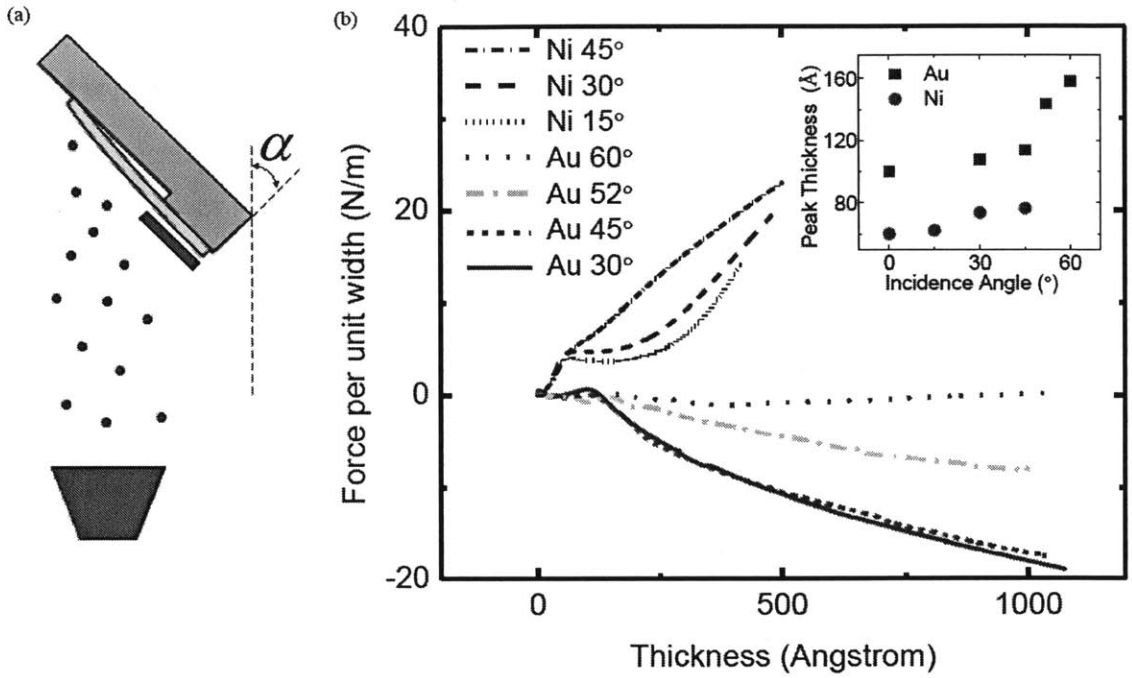

Figure 6.4. (a) Illustration of configuration used for in situ stress measurements for oblique angle deposition. (b) Stress evolution during oblique angle deposition of gold and nickel films. Inset: The thickness of tensile peak as a function of the incidence angle.

We refer to the thickness at which the tensile peak is reached as the peak thickness. Figure 6.4 (b) and the inset clearly show that the peak thickness increases with the angle of the incidence in both Au and Ni films. Since the tensile stress is caused by the zipping process during film coalescence, this indicates that the coalescence thickness increases with the angle of the incident flux. We can explain this trend by the geometrical effects discussed earlier. During the initial stages of film growth, adatoms condense onto the substrate and nucleate to form 3D islands. When the incident beam arrives at an oblique angle, the atoms are preferentially captured by the pre-exisiting islands because of the shadowing effect, and possibly also the

steering effect. This leads to a favored growth of the islands in the out-of-plane direction and a delay of the coalescence process. Consequently, the tensile peak is always observed in thicker films at higher incident angles.

In addition, Figure 6.4 (b) shows that Au films display typical Type II behavior up to an incidence angle of 45°. As the incidence angle further increases, the post-coalescence stress becomes much less compressive. At an incidence angle of 60°, the stress level is low after coalescence and a stress turnaround from compressive to tensile can be observed at a thickness of ~ 40nm. Generally, the post-coalescence stress in Au films becomes less compressive or more tensile as the incidence angle increases.

Similar phenomena have been observed in Ni films. It can be seen that the Ni films display the intermediate type of stress behavior up to an incidence angle of 30°. The turnaround thickness reduces from 37nm at 0°, to 19nm at 15° and to 15nm at 30°. At an incidence angle of 45°, the Ni film develops tensile stresses in all the growth stages, which is typical for Type I stress behavior. In other words, the post-coalescence stress in Ni films also becomes less compressive or more tensile as the incidence angle increases. The weakening of the compressive stress at higher incidence angles must correlate with the surface and/or grain structure evolution during growth. Characterizations of surface and grain structure evolution are presented in the next section.

6.4 SURFACE AND GRAIN STRUCTURE EVOLUTION DURING OBLIQUE ANGLE DEPOSITION OF GOLD AND NICKEL FILMS

6.4.1 SURFACE TOPOGRAPHY EVOLUTION

We used Atomic Force Microscopy (AFM) to study the surface topography of gold and nickel films grown by oblique angle deposition. Figures 6.5 (a) to (d) show AFM images of 115 nm-thick gold films grown at different incidence angles. It can be seen that the range of surface heights increases from 14.7nm at an incidence angle of 0°to 56.3nm at an incidence angle of 60°. This can be attributed to the more important role played by the shadowing effect at higher angles. Plots of inclination angle distribution in Figure 6.5 (e) show that a larger fraction of the surface area becomes steeper as the angle of incidence increases.

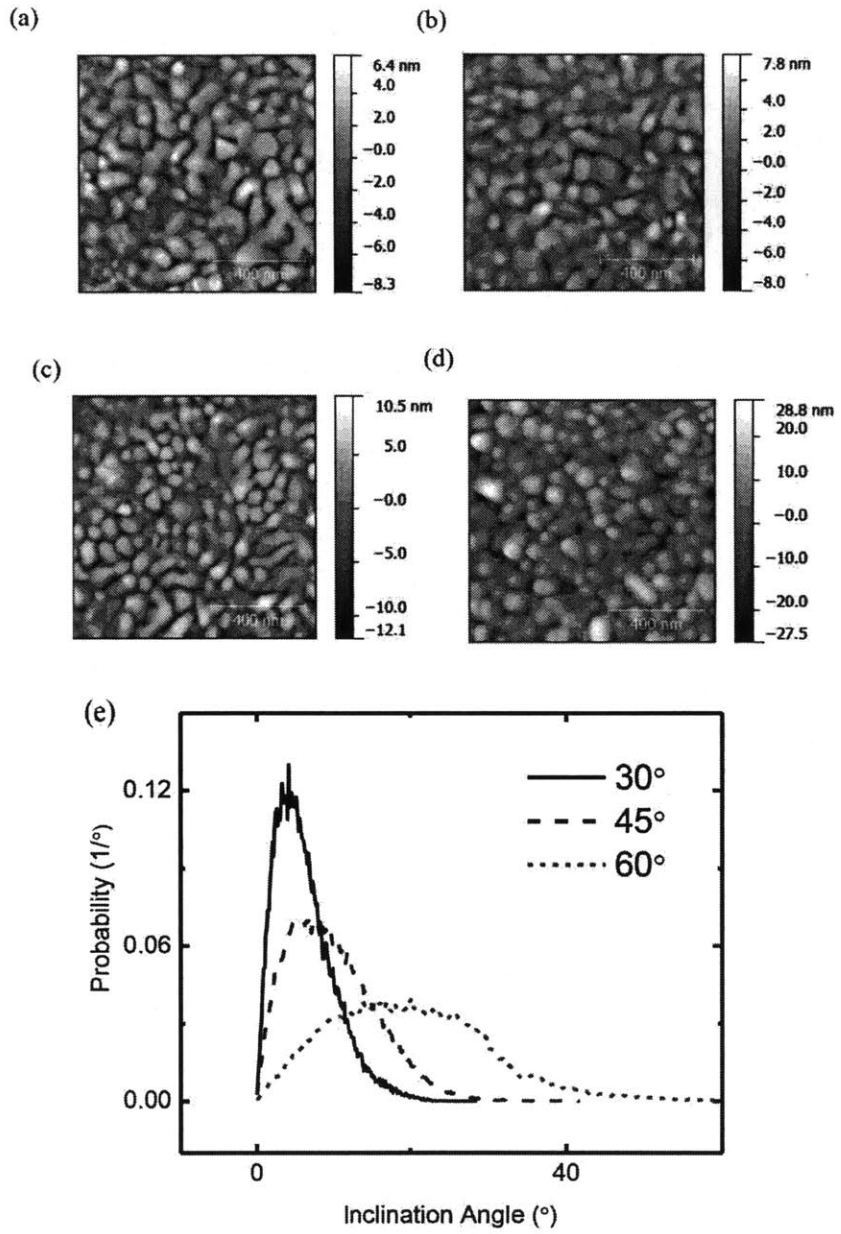

Figure 6.5. AFM images of 115nm-thick gold films deposited at (a) 0°, (b) 30°, (c) 45° and (d) 60°. The scan size is $1\mu m \times 1\mu m$. (e) Distribution of inclination angles of the films deposited at 30°, 45° and 60°.

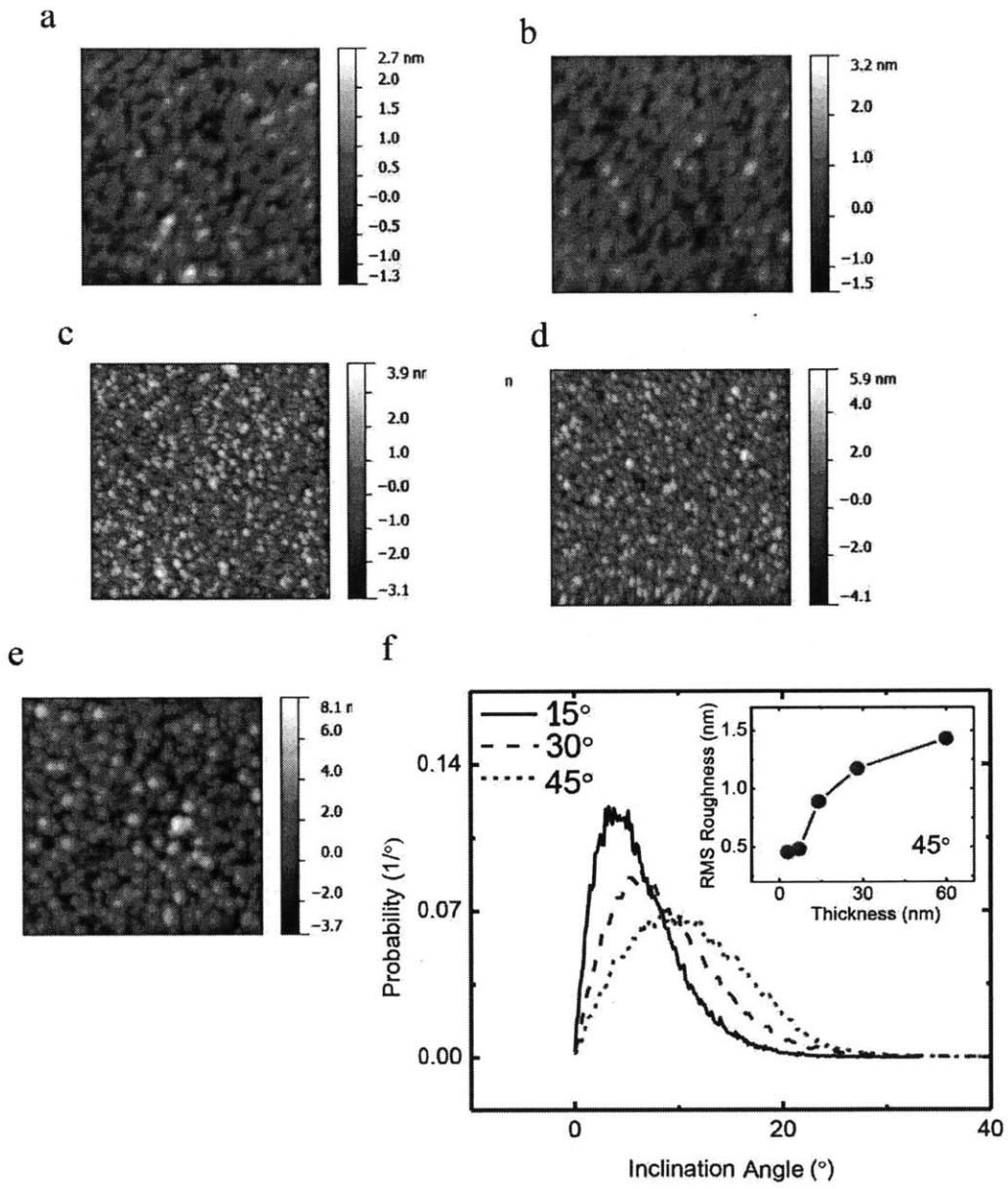

Figure 6.6. AFM images of nickel grown at an incidence angle of 45°with thicknesses of (a) 3nm, (b) 7nm, (c) 14nm, (d) 28nm and (e) 60nm. The scan size is $0.5\mu m \times 0.5\mu m$. (f). Distributions of the inclination angles for the surfaces of Ni films deposited at different

angles of incidence. Inset: RMS roughness as a function of the film thickness for Ni films grown at 45°.

Similar trends have been observed in Ni films. The AFM based analysis clearly shows that the surface roughness of Ni films increases as the incidence angle increases from 0 to 15, 30 and 45°. Moreover, we have studied the thickness dependence of the surface topography in Ni films grown at 45°. The relevant AFM images are shown in Figures 6.6. (a) and (b) show the surface topography before the film becomes fully continuous. After the coalescence process, both the size and depth of the surface domain increase with the film thickness during deposition (see Figures 6.6 (c), (d) and (e)). Figure 6.6 (f) summarizes the thickness and angle dependencies of the surface roughness of Ni films. It can be seen that the surface roughness increases with both the thickness and the incidence angle.

6.4.2 GRAIN STRUCTURE EVOLUTION

We used TEM to study the grain structure evolution in Ni films grown at 45°. Because the angle of the incidence was not high, complex nano-columnar structures similar to those in Figure 6.3 were not found from Cross-sectional TEM images. Instead, the microstructures of the films are similar to those of films grown by normal deposition. Plan view TEM images in Figure 6.7 show that the grain size increases with film thickness, as observed in the case of normal deposition.

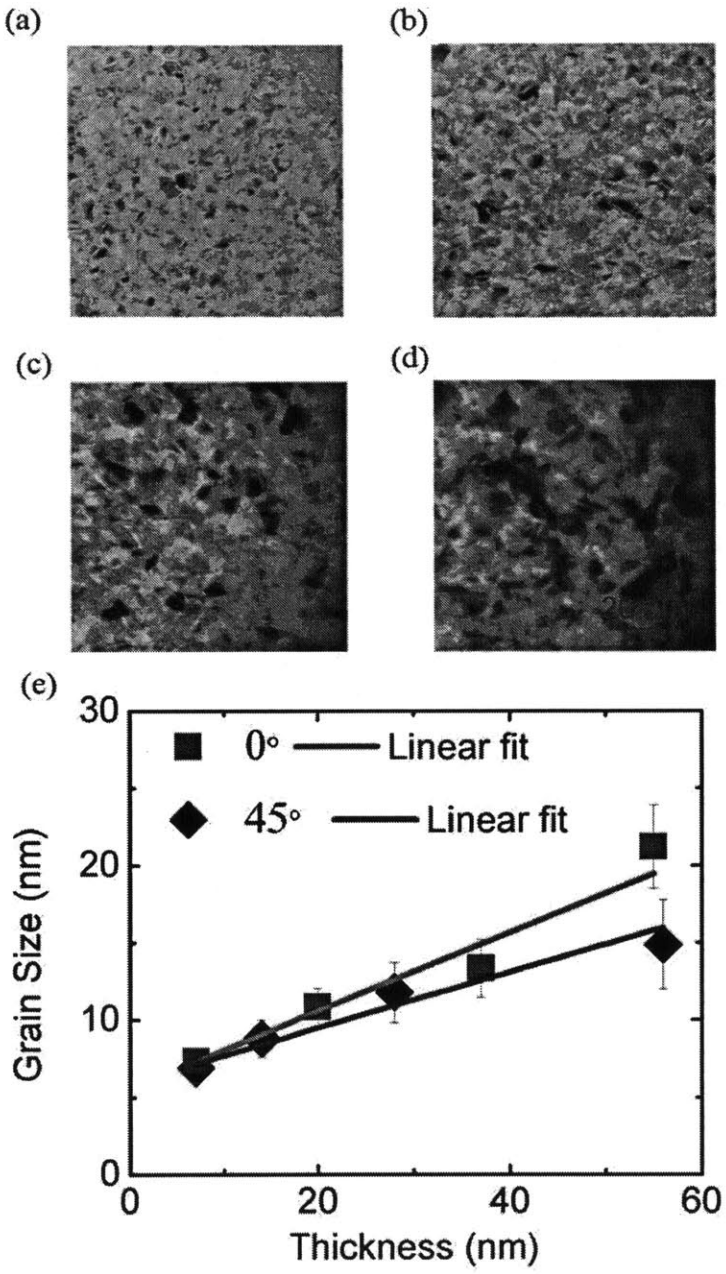

Figure 6.7. Bright field, plan-view TEM images of Ni films grown at 45°, with film thicknesses of (a) 7nm, (b) 14nm, (c) 28nm and (d) 55nm. (e) The grain size-thickness relationships in Ni films deposited at 0° and 45°.

Plan view TEM images show that for the 55nm Ni films, the grain size in the films deposited at 45° is slightly smaller than the grain size in the films deposited at 0°. As before, we used image analysis to quantify the average grain size in these films. Figure 6.7 (e) compares the grain size-thickness relationships in the Ni films deposited at 0° and 45°. For the films deposited at 45 °, the average grain size also increases linearly with film thickness, but it increases more slowly than the film deposited at 0°.

6.5 DISCUSSION

In the last section, we showed that the surface roughness and steep regions of gold and nickel films increase significantly with the angle of incidence of the evaporant flux. At a given film thickness, the grain size slightly decreases at higher incidence angles, as shown in Figure 6.7 for Ni films. At a given angle, the RMS roughness of the surface and the grain size all increase with the film thickness. In this section, we investigate how these evolutions affect the intrinsic stress during film growth.

6.5.1 COMPARISON OF THE COMPRESSIVE COMPONENT IN NICKEL FILMS DEPOSITED AT 0° AND 45°

Grain growth during deposition leads to a tensile component of the instantaneous stress, $\sigma_{in}^{gg}(d) = \frac{E}{1-\nu}\frac{\Delta a}{d}\left(\frac{1}{1+\frac{E\Delta a}{(1-\nu)\sigma_y d}}\right)$ (see Chapter 5). The instantaneous stress caused by grain growth during deposition of Ni films at 45° can be calculated using this equation and the plot

in Figure 6.7(e). The measured instantaneous stress can be obtained using $\sigma_{in} = \frac{\Delta(\frac{F}{w})}{\Delta h}$ and the stress curve in Figure 6.4. The compressive component of the instantaneous stress can then be calculated using $\sigma_{in}^{comp} = \sigma_{in} - \sigma_{in}^{gg}$. We compare the instantaneous stresses measured *in situ*, caused by grain growth, and caused by the compressive mechanism for deposition at incidence angles of 0° and 45° in Figure 6.8.

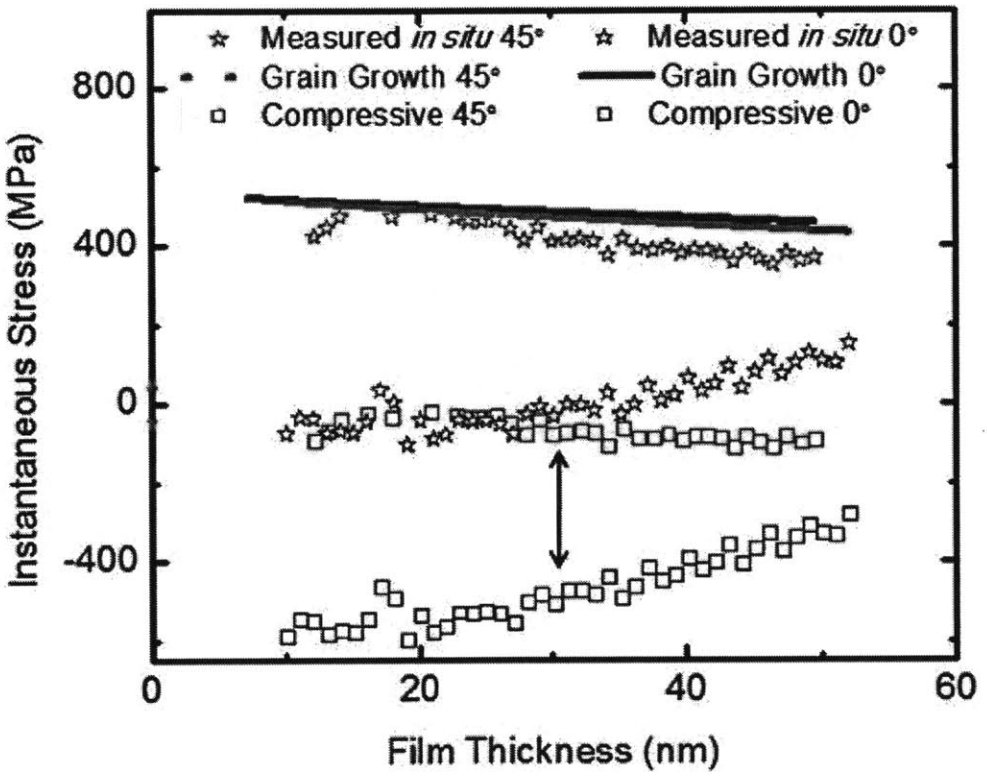

Figure 6.8. Instantaneous stress measured in situ, the component caused by grain growth, and the component caused by the compressive mechanism. A comparison between the Ni films deposited at angles of incidence of 0 and 45°.

It can be seen that the difference in the grain size-thickness relationships in Figure 6.7 (e) only leads to a small difference in the instantaneous stress caused by grain growth. Therefore, the difference in the measured stress mostly originates from the difference in the compressive component, as marked by the arrow in Figure 6.8. The small compressive stress for the 45° deposition can be attributed to the enhanced roughness and shadowing effect, as shown in the following subsections.

6.5.2 EFFECT OF SURFACE ROUGHNESS

In Chapter 5, we have shown that for a flat grain surface, the compressive component of the intrinsic stress is determined by a competition between the adatom-2D island attachment and the adatom-GB attachment. For a rough surface, numerous step edges are present on the film surface. As a result, the compressive stress is determined by a competition between adatom-step edge attachment and adatom-GB attachment. We use the framework developed in Chapter 5 to quantitatively analyze this case.

We assume that for the atoms deposited on the terrace adjacent to the grain boundary, the possibility of attaching to the GB surface sites is p_{GB} and the possibility of attaching to the step edge is $1-p_{GB}$. Let the width of this terrace be λ. For each grain, therefore, the ratio between the number of atoms attaching to GB and the number of atoms attaching to step edges is $\frac{N_{GB}}{N_{SE}} = \frac{2p_{GB}\lambda}{(1-p_{GB})2\lambda + d - 2\lambda} \approx \frac{2p_{GB}\lambda}{d}$. The number of step edges on each grain surface is $n = 2w_d / a$, where w_d is the height of the dome and a is the lattice constant (see

Figure 6.9 (a)). Therefore, the average terrace width is $\bar{\lambda} = \frac{d}{n} = \frac{da}{2w_d} = \frac{a}{2\beta}$, where $\beta = w_d / d$.

The resultant compressive stress is

$$\sigma_{in}^{comp} = -M \frac{2p_{GB}\bar{\lambda}}{d} = -M \frac{2p_{GB}}{d}(\frac{a}{2\beta}) = -M \frac{p_{GB}a}{w_d}, \qquad (6.2)$$

which is proportional to the inverse of the dome height. Equation (6.4) shows that due to the competition with adatom incorporation at step edges, the compressive stress associated with grain boundary attachment decreases more when the dome height is larger. AFM measurements clearly show that for a given film thickness, the dome height increases as the incidence angle increases (see Figure 6.9(b)). Therefore, the compressive component of the intrinsic stress significantly decreases at higher incidence angles.

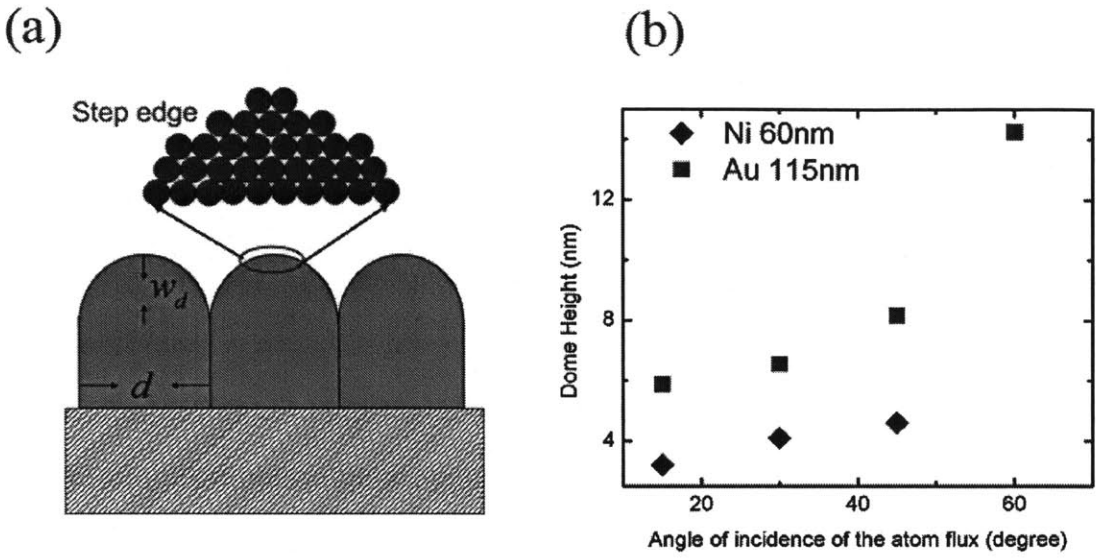

Figure 6.9. (a) Illustration of step edges on the surface of each grain. (b) The dome height measured by AFM as a function of the angle of incidence of the flux. Here we show the cases of 60nm Ni and 115nm Au.

6.5.3. SHADOWING AREA AND DOWNHILL DIFFUSION

We have shown that the compressive component of the intrinsic stress originates from adatom attachment to the surface sites of grain boundaries. For a polycrystalline film with a rough surface, the grain boundaries are often located at the valleys on the surface. For a sufficiently rough surface, oblique angle deposition can lead to no condensation on the terraces adjacent to the grain boundaries. This effect is illustrated in Figure 6.10 (a), where the region without adatom condensation has been highlighted in red. Here α is the angle of the incident flux, d is the grain size, and w_d is the height of the dome. Δw_1 and Δw_2 are the heights of the shadowed terraces on the 'illuminated' side and the shadowed side, respectively.

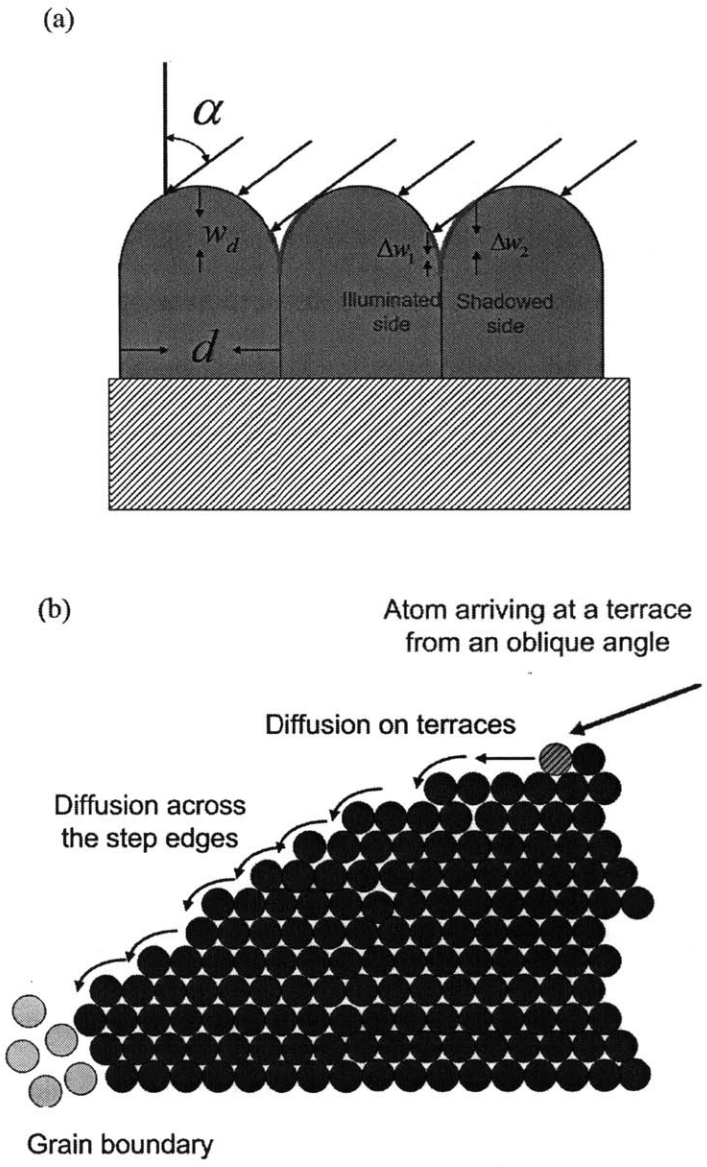

Figure 6.10. Effect of shadowing on adatom condensation and diffusion during oblique angle deposition.

In this case, adatom attachment to grain boundaries requires downhill diffusion across the step edges. Additional thermal energy is required to overcome the Ehrlich-Schwoebel (ES) barriers. The rate for crossing step edges can be written as $\nu^* = \nu_0^* e^{-(E_s+\Delta E)/kT}$, compared to $\nu = \nu_0 e^{-E_s/kT}$ for diffusion on a terrace. Here E_s is the activation energy for terrace diffusion and ΔE is the additional energy to cross a step edge. It should also be noted that ν_0 is the attempt rate for a random walk that is irrespective of direction, whereas ν_0^* is the attempt rate for a specific direction. Therefore, the value of ν_0^* should be smaller than ν_0. For example, Field Ion Microscopy experiments show that $\frac{\nu_0^*}{\nu_0} \sim 10^{-2}$ for homoepitaxial growth of Pt films [21]. Furthermore, as an adatom crosses a step, there is a high probability of being incorporated into the edge of the step. If this probability is p_E, the probability of an atom diffusing from a high terrace to a grain boundary is $p = 1 - n^{\dagger} p_E$, where $n^{\dagger}$ is the number of step edges in the diffusion path. Because of the above reasons, the adatom GB attachment is significantly suppressed when no atoms condense on the terrace adjacent to a grain boundary, and a larger shadowed region leads to a lower compressive component of the intrinsic stress.

The area of the shadowed region depends on the local curvature of the domed surface at the grain boundary. Here we use the simplest geometry to demonstrate the incidence angle and surface roughness dependencies of the shadowed area. If the dome on each grain surface is a spherical cap, the heights of the shadowed terraces can be derived as

$$\Delta w_1 / d = \beta\left(\frac{1+\sin\alpha}{2}\right) + (1+\cos 2\alpha)\sqrt{\frac{\beta^2+1}{2\beta\cos\alpha} - 1} - \left(\sin 2\alpha + \frac{1-\sin\alpha}{2\beta}\right), \qquad (6.3a)$$

and

$$\Delta w_2 / d = \frac{\beta}{2}(\sin\alpha + 1) + \frac{1}{2\beta}(\sin\alpha - 1), \tag{6.3b}$$

where $\beta = w_d / d$ and Δw_1 and Δw_2 are defined in Figure 6.10 (a).

For a shadowed area to exist, $\alpha > \arcsin(\frac{1-\beta^2}{1+\beta^2})$. The numbers of step edges to cross in the shadowed regions on each side of the grain boundary are

$$n_1 = (\frac{d}{a})[\beta(\frac{1+\sin\alpha}{2}) - (1+\cos 2\alpha)\sqrt{\frac{\beta^2+1}{2\beta\cos\alpha} - 1} - (\sin 2\alpha + \frac{1-\sin\alpha}{2\beta})] \ , \tag{6.4a}$$

and

$$n_2 = (\frac{d}{a})[\frac{\beta}{2}(1+\sin\alpha) + \frac{1}{2\beta}(\sin\alpha - 1)]. \tag{6.4b}$$

Figure 6.11shows a plot of n_1 and n_2 as a function of the incidence angle and the parameter β. It should be note that here the unit of n_1 or n_2 is (d / a). For the 55nm Ni films grown from 45°, the value of (d / a) is ~ 80. It can be seen that the numbers of step edges in the diffusion path increases with β and the incidence angle α. For a given film thickness, as the incidence angle α increases, the dome height increases and the grain size slightly decreases (shown in Section 6.4). As α increases, therefore, the value of β increases, and the area of the shadowed

region increases. Consequently, the compressive stress caused by adatom-GB attachment decreases more at a higher incidence angles due to the shadowing effect.

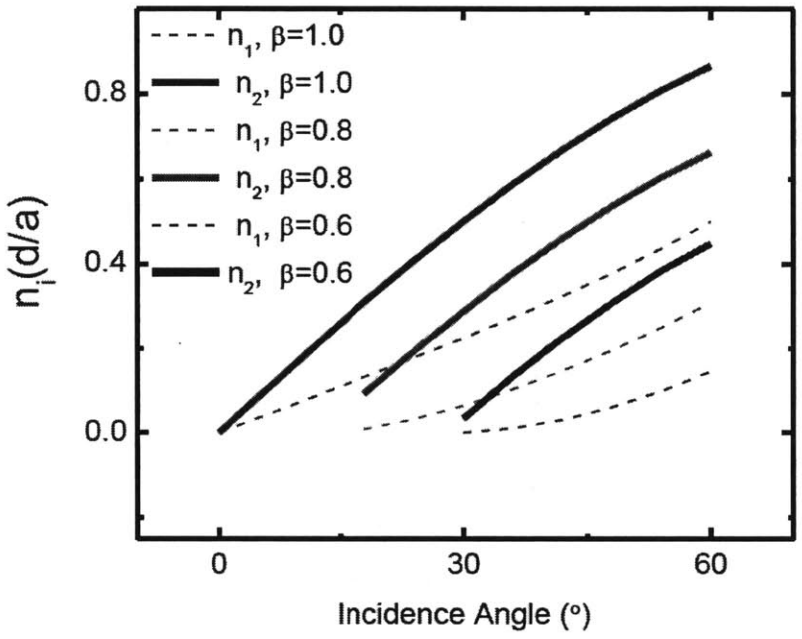

Figure 6.11. Numbers of terraces in the shadowing area as a function of the incidence angle.

Moreover, the steering effect can lead to a redistribution of the atom flux, with the atoms preferentially captured by protruding sites on the surfaces. This effect can further reduce the number of adatoms on the terraces that are close to grain boundaries, and thereby reduce the compressive stress caused by adatom-GB attachment.

6.6 SUMMARY

The angle of incidence of the evaporant flux can significantly influence the surface morphology and stress evolution during polycrystalline film growth. From *in situ* stress measurements of gold and nickel films, we have found that tilting the sample to higher angles leads to (a) an increase of the film thickness at which the peak tensile stress is reached (when the film becomes continuous), and (b) a more tensile or a less compressive stress evolution after island coalescence. The first phenomenon is due to the shadowing effect, which leads to preferential growth along the out-of-plane direction of the 3D islands and a delay of the coalescence process. For the second phenomenon, we show that the difference in the measured stress mostly originates from the difference in the compressive component caused by the adatom incorporation at grain boundaries. When the atom flux arrives at a higher angle with respect to normal incidence, the adatom -GB trapping process is significantly suppressed because of the shadowing effect and the enhanced surface roughness that develops during oblique angle deposition.

Competition with the adatom-step edge incorporation process makes adatom-GB incorporation less likely on rougher surfaces. In addition, with a sufficiently rough surface, oblique angle deposition can result in zero condensation of atoms on the terraces adjacent to grain boundaries. As a result, the adatom-GB incorporation requires downhill diffusion of adatoms, which have to overcome an additional Ehrlich-Schwoebel barrier as they cross a terrace edge. In this process, the adatom also has a high probability of being incorporated into the step. Furthermore, the steering effect can lead to a redistribution of the atom flux, with the atoms being preferentially captured by protruding sites on the surfaces. The shadowing effect,

the steering effect and the presence of Ehrlich-Schwoebel barriers all lead to a rougher surface during oblique angle deposition and a smaller magnitude of the compressive stress caused by adatom-GB incorporation.

From Figure 6.4, it is interesting to note that at sufficiently high angles, the stress behavior in Ni films changes from the intermediate type to Type I, while the stress behavior in Au films changes from Type II to the intermediate type. Therefore, the angle of incidence of the evaporant flux is another parameter that can be used for tuning the type and magnitude of the intrinsic stress that develops during growth of polycrystalline films.

REFERENCES

[1] Schwoebe.Rl, and E. J. Shipsey, Journal of Applied Physics 37, pp. 3682 (1966).

[2] G. Ehrlich, and F. G. Hudda, Journal of Chemical Physics 44, pp. 1039 (1966).

[3] S. van Dijken, L. C. Jorritsma, and B. Poelsema, Physical Review Letters 82, pp. 4038 (1999).

[4] Y. Shim, V. Borovikov, and J. G. Amar, Physical Review B 77 (2008).

[5] J. G. Yu, J. G. Amar, and A. Bogicevic, Physical Review B 69 (2004).

[6] D. E. Sanders, D. M. Halstead, and A. E. Depristo, Journal of Vacuum Science & Technology a-Vacuum Surfaces and Films 10, pp. 1986 (1992).

[7] J. L. Plawsky, J. K. Kim, and E. F. Schubert, Materials Today **12**, pp. 36 (2009).

[8] M. M. Hawkeye, and M. J. Brett, Journal of Vacuum Science & Technology A 25, pp. 1317 (2007).

[9] K. Robbie, and M. J. Brett, Journal of Vacuum Science & Technology a-Vacuum Surfaces and Films 15, pp. 1460 (1997).

[10] K. Robbie, J. C. Sit, and M. J. Brett, Journal of Vacuum Science & Technology B 16, pp. 1115 (1998).

[11] R. Messier, V. C. Venugopal, and P. D. Sunal, Journal of Vacuum Science & Technology a-Vacuum Surfaces and Films 18, pp. 1538 (2000).

[12] L. Abelmann, and C. Lodder, Thin Solid Films 305, pp. 1 (1997).

[13] Nieuwenh.Jm, and H. B. Haanstra, Philips Technical Review 27, pp. 87 (1966).

[14] J. J. Steele, and M. J. Brett, Journal of Materials Science-Materials in Electronics 18, pp. 367 (2007).

[15] F. L. W. Rabbering, G. Stoian, R. van Gastel, H. Wormeester, and B. Poelsema, Physical Review B 81 (2010).

[16] S. van Dijken, G. Di Santo, and B. Poelsema, Physical Review B 63 (2001).

[17] S. van Dijken, L. C. Jorritsma, and B. Poelsema, Physical Review B 61, pp. 14047 (2000).

[18] H. Wormeester, and B. Poelsema, Physical Review B 66 (2002).

[19] S. G. Mayr, and K. Samwer, Journal of Applied Physics 91, pp. 2779 (2002).

[20] S. Vauth, C. Streng, S. G. Mayr, and K. Samwer, Physical Review B 68 (2003).

[21] T. Michely, and J. Krug, *Islands, mounds, and atoms : patterns and processes in crystal growth far from equilibrium* (Springer, Berlin ; New York, 2004), Springer series in surface sciences, 42.

CHAPTER 7

SUMMARY AND FUTURE WORK

7.1 KEY FINDINGS

Combining *in situ* stress measurements, surface and microstructure characterization and analytical modeling, the goal of this thesis research was to elucidate the underlying mechanisms for intrinsic stress evolution during and after polycrystalline film growth. The investigation of the stress behavior has been carried out under different conditions. The experimental variables included the material, the film thickness, the substrate temperature, the deposition rate, the interruption time and the angle of incidence of the depositing atoms. A series of mechanisms has been proposed and justified for the stress change towards the tensile direction during a growth interruption, for the transition from a compressive stress to a tensile stress state after coalescence under conditions of intermediate atomic mobility, and for the change to a less compressive or more tensile stress state in oblique angle deposition. The results of this work offer a way to control the residual stresses in thin films during and after processing.

The following conclusions can be drawn based on the framework presented in this thesis:

- In systems of high or intermediate atomic mobility, a reversible stress is observed during a short interruption of growth. The change of force per unit width associated with the short interruption is weakly dependent on the film thickness and substrate temperature. This

reversible stress originates from the reversible change of the film surface in the presence and in the absence of the atom flux. During growth, the surface is flat and the dihedral angle at the grain boundary is higher than the equilibrium angle. Excess atoms trapped in the grain boundaries can lead to a compressive stress in the film. During a growth interruption, surface diffusion allows the groove to evolve to the equilibrium depth. This process leads to the removal of trapped atoms in the surface layers of the film and a relaxation of the compressive stress.

- The long-term change of force per unit width during a growth interruption is irreversible, and is strongly dependent on temperature and film thickness. This originates from a structure evolution processes in the bulk of the film. Because of the adhesion at the substrate-film interface, grain growth in the film causes tensile stress. Characterization of the grain size in gold films suggests that a significant portion of the stress change during a long growth interruption can be attributed to grain growth.

- The stress evolution in systems of intermediate atomic mobility involves a turnaround from the compressive to the tensile state after coalescence. This stress turnaround phenomenon is strongly dependent on the substrate temperature and deposition rate, and can be attributed to the grain growth occurring during film deposition. The increase of grain size not only leads to a tensile component of the intrinsic stress, but also changes the grain size dependence of the compressive component caused by the trapping of excess atoms in the grain boundaries.

- Oblique angle deposition leads to (a) an increase of the coalescence thickness, and (b) a less compressive or a more tensile stress in the film. The first trend can be explained by the shadowing effect, which leads to preferential condensation of the atoms on higher sites of the surface, and thereby leads a delay of the coalescence process. The second trend can be attributed to the shadowing effect, the steering effect, and the enhanced surface roughness, which all lead to suppression of the adatom-grain boundary incorporation process.

- For a flat surface, the magnitude of the compressive component of the intrinsic stress is controlled by a competition between the incorporation of atoms into 2D islands and incorporation in grain boundaries. The compressive stress caused by this mechanism is independent of grain size when the grain size is small, and is proportional to the inverse of the grain size when the grain size is large. For a rough surface, the magnitude of the compressive component is controlled by a competition between the adatom-step edge incorporation and adatom-grain boundary incorporation. A higher ratio between the dome height of a grain and its in-plane size leads to a smaller compressive stress.

- Intrinsic stresses in polycrystalline films can be categorized into three types: Type I, the intermediate type and Type II. These behaviors are observed in systems of low, intermediate and high atomic mobility, respectively. The transition of the stress behavior from Type I, to the intermediate type of behavior and to Type II behavior is continuous and can be achieved by adjusting deposition conditions. Whether the post-coalescence stress is tensile, or compressive, or evolving from compressive to tensile state depends on the homologous

temperature, the deposition rate and the angle of the incident atomic flux. The relevant stress evolution category diagrams are shown in Figure 7.1.

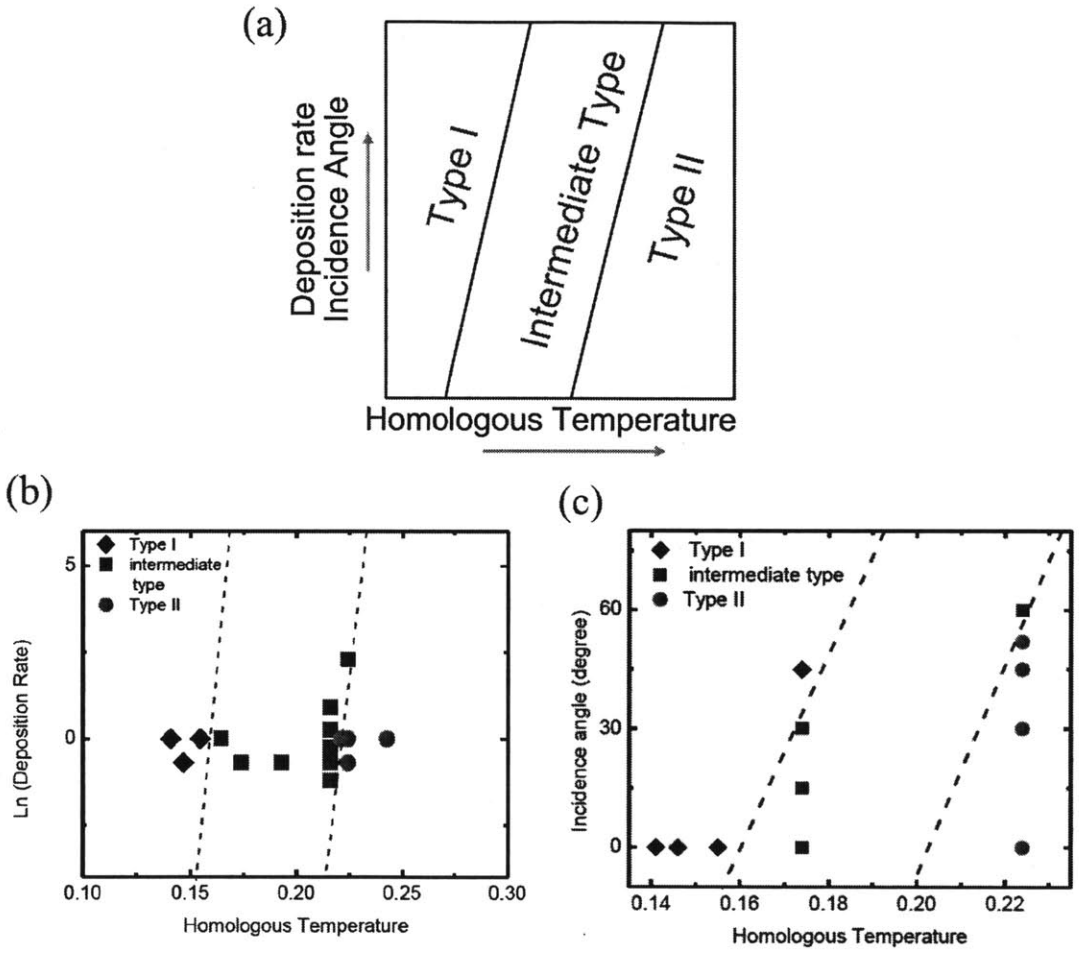

Figure 7.1. Stress evolution category diagrams. (a) A schematic diagram. The experimental data show that the stress behavior can be controlled by adjusting (b) the deposition rate and the homologous temperature of the system, or by adjusting (c) the incidence angle of the flux and the homologous temperature of the system.

7.2 FUTURE WORK

The work in this thesis focuses on the fundamentals of stress evolution and the underlying mechanisms, under normal deposition conditions. A few directions of great interest can be pursued in future work.

First, the surface topography of the substrate should have a significant influence on the structure and stress evolution in thin films and related nanoscale patterns. We can fabricate surface features on the substrate and then measure the stress in the films deposited on this substrate. The features could range from 1D periodic trenches, pits of random distribution to array of pits and array of hills. The fabrication methods include conventional lithography, interference lithography [1, 2], e-beam lithography and block-copolymer self-assembly [3] based techniques, depending on the targeted feature size. When the feature size is reduced below 100nm, it is smaller or at least comparable to the grain size in the films. The geometrical confinement could lead to a dramatic change of the structure, intrinsic stress and the mechanical behavior of the films. It should be noted that if the trench is deep, the flat surface approximation is no longer valid and the Stoney equation cannot be used to correlate the measured cantilever deflection with the average stress in the film. New analytical models should be built for the relation between the stress and the measured deflection in this case.

Another direction to pursue is the stress evolution in films of controlled microstructure. This can be done by means of seeded growth, in which the deposition is carried out on islands of controlled sizes (and sometimes even of controlled orientations). These islands can be formed by dewetting. In particular, it will be of great interest to study how the coalescence stress

changes with the initial island size and spacing. Hearne *et al.* [4] have studied stress evolution during electrodeposition of semi-cylindrical polycrystalline islands on the substrate surface with parallel trench-like holes. They found that the measured coalescence stress scaled with the trench spacing in a way that was well matched with a finite element simulation of the type developed by Seel *et al.* [5]. However, the conditions of these experiments differ in important ways from the vapor-phase deposition described in this thesis. The length scales were significantly larger (with a minimum trench spacing of 0.3μm), the islands were polycrystalline, and the island geometry was one-dimensional. Moreover, effects of impurity and surface charging during electrodeposition were not taken into account.

In addition, the chemistry of the substrate and the film surfaces should play an important role in the stress development during the island growth stage. This can be seen from the fact that the initial compressive stress is not always observed in *in situ* measurement. The stresses in the islands depend on the electronic structures of the substrate surface and the deposited materials. Possible experiments include depositing the islands on substrates with specific chemical modifications. DFT (Density Functional Theory) based calculations may be used to interpret the results.

Using the tiltable stress sensor, the impact of the angle of the incident flux on reversible stress evolution in Type II systems can be investigated. We have shown that the stress change during a growth interruption is associated with the shape change of the grain surface. At higher angles, the surface becomes rougher and the grain boundary grooves are deeper. As a result, under such conditions, the stress change during a growth interruption might be reduced or might be in the compressive direction. Also, to measure the surface roughness evolution *in*

situ during growth and growth interruptions, a laser scattering technique may be used in the future. Qualitatively, a rougher surface will lead to a weaker specular reflection. To quantitatively characterize the surface roughness, it is necessary to measure the power spectral density at different spatial frequencies. This can be done using a light source with a fixed wavelength and rotating the sample and detector (Angle Resolved Spectroscopy, ARS) [6]. Alternatively, a white or UV light source can be used and nonspecular reflection in a single direction can be analyzed at different frequencies using a spectrometer [7].

Moreover, the stress evolution during a pulsed deposition can be measured by adding a motor-controlled sample shutter in the Perkin-Elmer system. The stress and structure of the film are then a function of the rotation frequency and the nominal deposition rate. The stress evolution in low melting materials such as Sn and Mg would also be interesting because their microstructures can be different from the films discussed in this work. For example, Sn films are sometimes not fully continuous even when the thickness is on the order of 1 μm. Besides polycrystalline films, amorphous films and alloyed films can be studied using the current set-up. The understanding of the experimental results would require knowledge of structure evolution during the growth of these films.

Finally, such *in situ* stress measurement can be used to study other kinetic processes, such as chemical reactions and phase transformations. For example, understanding the lithiation process is of great interest to the battery community. *In situ* stress measurement of the electrode material could unveil new insights into the surface and microstructure evolution during this process [8].

REFERENCES

[1] I. Divliansky, T. S. Mayer, K. S. Holliday, and V. H. Crespi, Applied Physics Letters **82**, pp. 1667 (2003).

[2] H. H. Solak *et al.*, Microelectronic Engineering **67-8**, pp. 56 (2003).

[3] M. Park, C. Harrison, P. M. Chaikin, R. A. Register, and D. H. Adamson, Science **276**, pp. 1401 (1997).

[4] S. J. Hearne, S. C. Seel, J. A. Floro, C. W. Dyck, W. Fan, and S. R. J. Brueck, Journal of Applied Physics **97** (2005).

[5] S. C. Seel, and C. V. Thompson, Journal of Applied Physics **93**, pp. 9038 (2003).

[6] V. A. Sterligov. *Angle-Resolved Light Scattering from Semiconductors*, Phys. Stat. Sol. **A170,** 443 (1998)

[7] R. Scheer, A. Neisser, K. Sakurai, P. Fons, and S. Niki, *$Cu(In_{1-x}Ga_x)Se_2$ Growth Studies by in situ Spectroscopic Light Scattering*. Appl. Phys. Lett. **82**, 2091 (2003).

[8] M. J. Chon, V. A. Sethuraman, A. McCormick, V. Srinivasan, and P. R. Guduru, Physical Review Letters **107** (2011).

APPENDIX A DETAILS OF GRAIN GROWTH

In Chapter 4, we discussed the grain growth observed during growth interruptions of gold and nickel films, with an emphasis on its effect on the intrinsic stress evolution. In these cases, grain growth occurs at a homologous temperature ~0.2-0.3, much lower than the temperature expected for grain growth to occur in bulk materials. This can be attributed to the high driving force associated with the nanoscale grain size in these films, which is a natural consequence of vapor phase deposition. In this section, we provide more details on the structure change associated with grain growth based on TEM observations, including the grain growth mode during and after deposition, grain boundary migration, and defect generation.

A.1 GRAIN GROWTH DURING AND AFTER DEPOSITION

Grain growth can occur both during and after deposition. For high mobility metals such as Au, Ag, Cu and Al, the films often develop equiaxed structure when deposited at room temperature so that the average grain size is roughly equal to the film thickness [1]. Under conditions of constant deposition rate, this leads to a grain growth of linear growth rate [2], which should be distinguished from normal grain growth in which the average grain size follows a parabolic law. In addition, this mode of grain growth occurs in the presence of a deposition flux, in contrast with the grain growth without deposition flux that has been extensively discussed in literature [1-7].

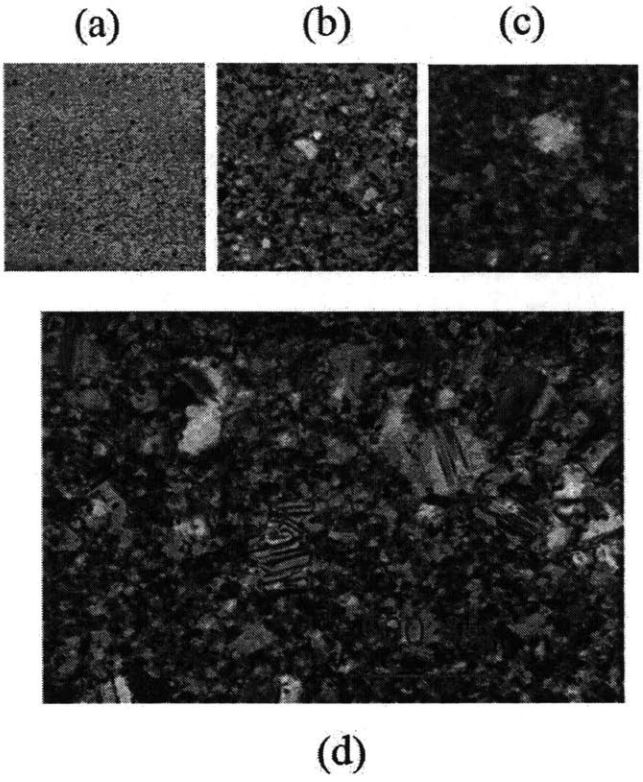

Figure A.1. Plan view TEM images of (a) 7nm, (b) 55nm, (c) 100nm thick Ni films deposited at 473K and (d) a 100nm thick Ni film deposited at 473K and then annealed at 473K for 60min.

When the film is thin, the grain size often has a monomodal distribution and abnormal large grains are rarely observed (see Figure A.1(a)). When the film gets thick enough, some abnormal large grains can be observed during deposition (see Figure A.1 (b) and (c)). Further film thickening results in an increase of the size of both the abnormal large grains and the matrix of small grains, with the latter strongly dependent on the film thickness. When the growth is stopped, substantial abnormal grain growth may continue to occur, while the size of the matrix grains also slightly increases (see Figure A.1 (d)). It should be noted that the onset

temperature for grain growth in the presence of an atom flux (during deposition) is lower than the onset temperature for grain growth in the absence of an atom flux (after deposition). For example, in Ni films deposited at 300K, grain growth has been observed during deposition but not after deposition.

A.2 ABNORMAL GRAIN GROWTH

Here we report TEM observation of abnormal grain growth during growth interruptions of gold films. The film was 45nm thick and was deposited at room temperature. Figure A.2 shows TEM video snapshots of the microstructure evolution during a 60second recording. During the initial thirty-three seconds of recording, only a few small and discrete grain boundary movements were observed. Starting from the 34th second, the upper left boundary of the circled grain suddenly migrated a total area of ~8000 nm^2 within a five-second interval. During this interval, the grain boundary could have a velocity as high as 50nm/s, considerably faster than long-range diffusion processes. However, the motion of the grain boundary was discontinuous and no further migration occurred in the following 5 min of the experiment. Moreover, the grain growth was not homogeneous--the other regions in the image largely remained unchanged during the whole period of recording.

During migration, an individual grain boundary can have a velocity as high as 50nm/s. This unusually high grain boundary mobility might be explained using the atomic shuffling model proposed by Babcock and Balluffi [8-10], who observed jerky motion of a Σ5 boundary in Au films (grain size~ 500nm) through hot stage *in situ* TEM. Based on this model, grain boundary migration may only require dislocation motion with a much lower activation energy

than long-range diffusion processes, which are activated at elevated temperatures. The fact that some small grains resist the expansion of larger ones may suggest the existence of specific configurations of grain boundary structure in which atomic shuffling is unfavorable. However, this model has not been experimentally justified. Further studies are needed to reveal the atomic mechanism for grain boundary migration in the cases discussed above.

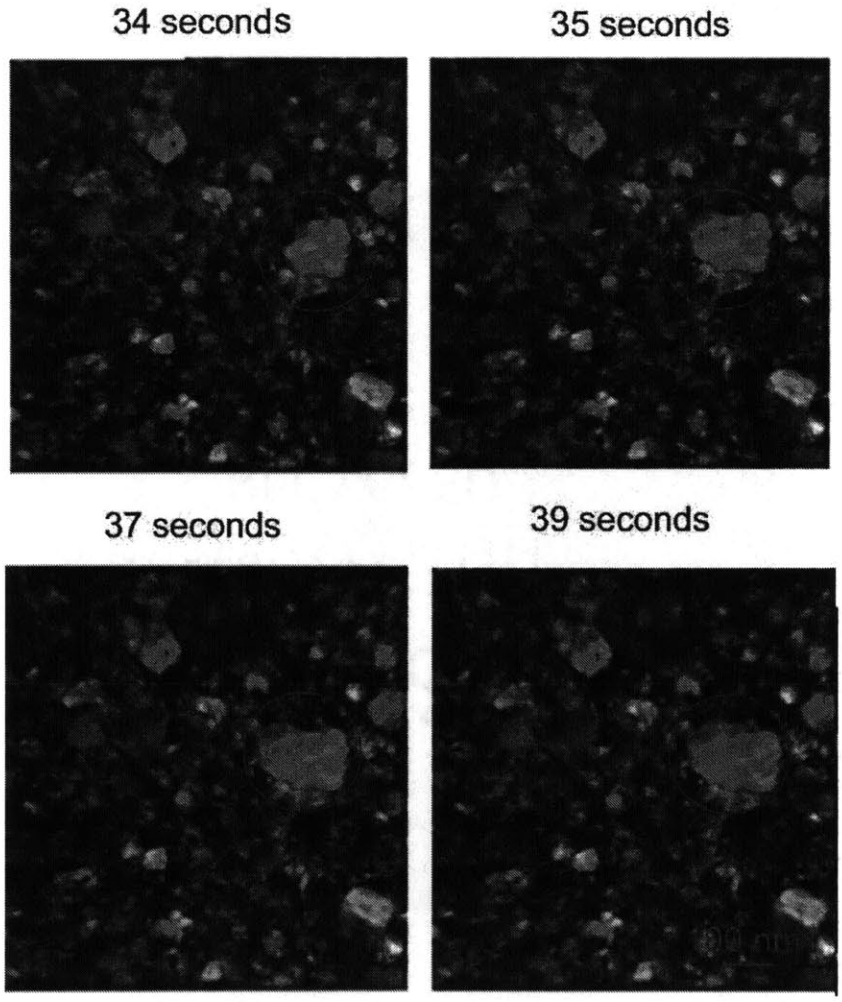

Figure A. 2. TEM video snapshots of a 45nm gold film at room temperature.

A.3 DEFECTS CREATED DURING ABNORMAL GRAIN GROWTH

A variety of defects can be generated during abnormal grain growth, including dislocations, sub-grain structures, twins and other planar defects. As an example, Figure A.3 shows a typical grain structure of a 45nm-thick gold film after substantial abnormal grain growth. A few planar defects (labeled p) and line defects (labeled L) can be seen in the central large grain. The generation of these defects may be associated with grain boundary migration during abnormal grain growth, because most of them are connected to the grain boundaries.

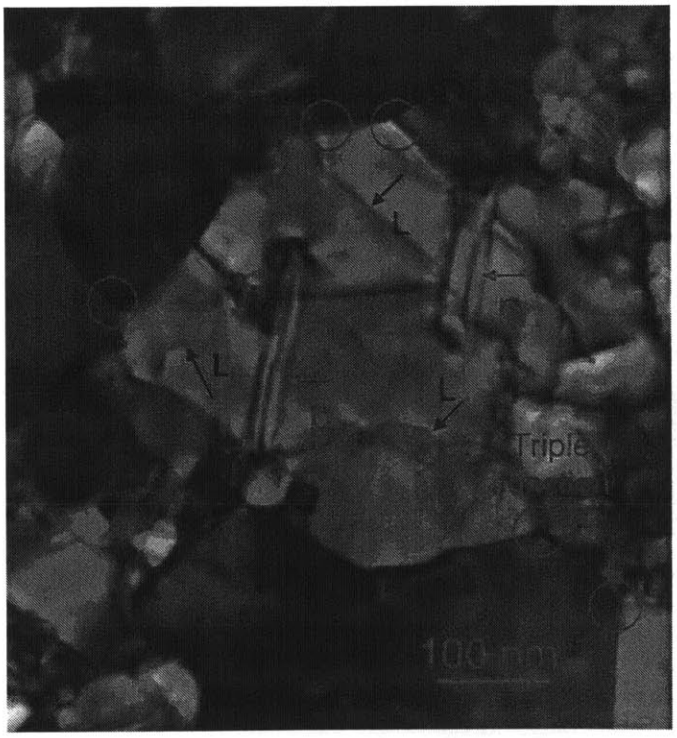

Figure A.3. Defect creation in a 45nm gold film after substantial abnormal grain growth.

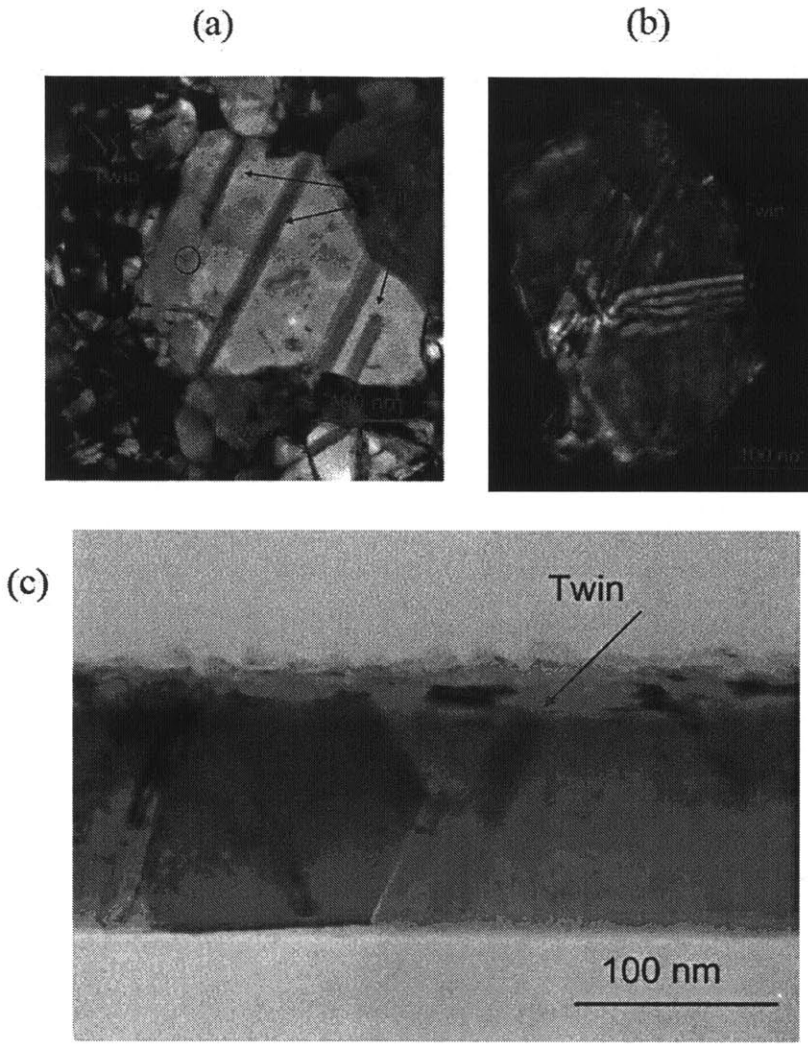

Figure A.4. Annealing twins: (a) bright field TEM image of a polycrystalline gold film, (b) dark field TEM image of a nickel film, and (c) a cross-sectional TEM image of a nickel film.

Annealing twins are the most common planar defects in abnormal large grains in nickel and gold films. The twins can transverse the grain, terminate inside the grain or interact with each

other (see Figure A.4). Usually at least one side of a twin terminates at grain boundaries, indicating that its generation is associated with grain boundary migration during grain growth. The stacking-fault energy is low for gold ~35 mJ/m^2 [11], but is high for nickel ~125 mJ/m^2 [12]. It is thus questionable to argue that the generation of annealing twins is governed by the stacking-fault energy.

Sub-grain structures (labeled S in Figure A.5) are sometimes observed inside abnormal large grains, in both gold and nickel films. This can be a result of occasional imperfect alignment of atomic planes during grain boundary migration, which leads to a network of low angle grain boundaries forming inside the abnormal large grain. In addition to dislocation lines and planar defects, a complex defect of unknown structure and origin can be seen inside the large grain in Figure A.6 (a). Also can be seen is the formation of dislocation defects associated with grain boundaries (bottom-right). As shown in Figure A.6 (b) and (c), some complicated fringes are seen in large grains in nickel films, possibly originating from a thickness gradient or faceting.

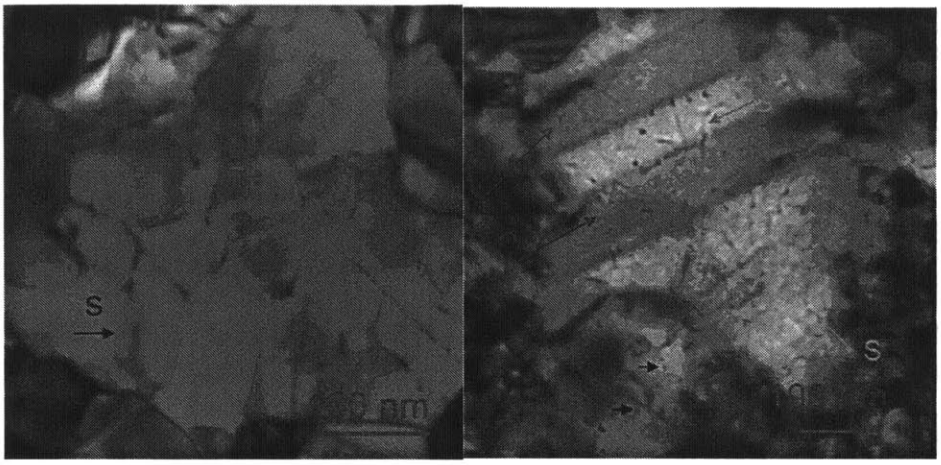

Figure A.5. Sub-grain structures inside abnormal large grains of gold (left) and nickel (right) films.

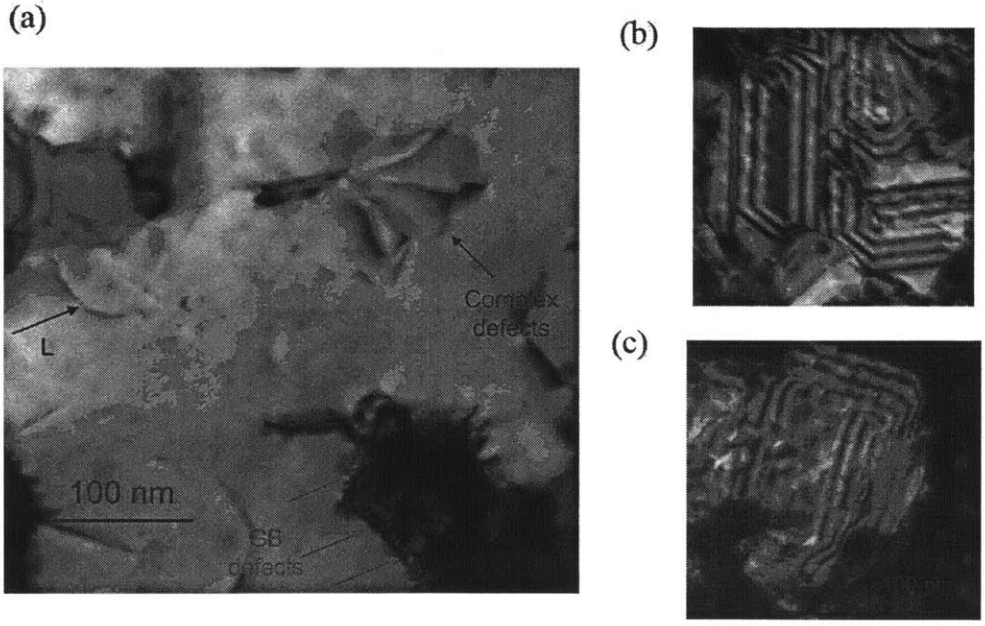

FigureA.6. Other defects observed in (a) Au, (b) and (c) Ni films.

Figure A.7 shows defect evolution during a two-minute interval in gold films recorded at room temperature *in situ* in a TEM. Two changes were observed. The first is the elimination of stacking faults inside the circled large grain. It is interesting to compare the stacking faults here and twins discussed before. The stacking faults were not connected to grain boundaries and were eliminated during growth interruptions, while the twins are always connected to the grain boundaries and are commonly observed inside large grains. Note that during this interval, the boundary of the circled grain also moved slightly (left and bottom edges). The second change in Figure A.7 is the change of the orientation and length of the line defect pointed out by the blue arrow. This change is accompanied by the length reduction of a planar defect (labeled p) that is connected to the line defect. The length of the line defect increased from ~31.5nm to ~39.5nm, while the planar defect reduced ~15nm in length. By doing this, the total energy decreases since the planar defect has a much higher energy than the line defect.

Figure A.7. Defect evolution during a two-minute interval observed in a 45nm gold film.

REFERENCES

[1] C. V. Thompson, Annual Review of Materials Science **20**, pp. 245 (1990).

[2] K. N. Tu, A. M. Gusak, and I. Sobchenko, Physical Review B **67**, p. 245408 (2003).

[3] F. J. Humphreys, and M. Hatherly, *Recrystallization and related annealing phenomena* (Elsevier, Amsterdam ; Boston, 2004), 2nd edn.

[4] C. V. Thompson, Journal of Applied Physics **58**, pp. 763 (1985).

[5] E. A. Holm, and S. M. Foiles, Science **328**, pp. 1138 (2010).

[6] J. E. Palmer, C. V. Thompson, and H. I. Smith, Journal of Applied Physics **62**, pp. 2492 (1987).

[7] G. S. Rohrer, in *Annual Review of Materials Research*2005), pp. 99.

[8] S. E. Babcock, and R. W. Balluffi, Philosophical Magazine a-Physics of Condensed Matter Structure Defects and Mechanical Properties **55**, pp. 643 (1987).

[9] S. E. Babcock, and R. W. Balluffi, Acta Metallurgica **37**, pp. 2367 (1989).

[10] S. E. Babcock, and R. W. Balluffi, Acta Metallurgica **37**, pp. 2357 (1989).

[11] M. L. Jenkins, Philosophical Magazine **26**, pp. 747 (1972).

[12] K. Hattar, D. M. Follstaedt, J. A. Knapp, and I. M. Robertson, Acta Materialia **56**, pp. 794 (2008).

APPENDIX B EFFECT OF OXYGEN PARTIAL PRESSURE ON STRESS EVOLUTION IN GOLD FILMS

The growth process of polycrystalline films is strongly influenced by the vacuum condition during deposition. It is thus of great interest to study how the presence of a specific type of gas can affect the intrinsic stress evolution process. Such experiments can be performed by flowing gases into the vacuum chamber through a leak valve (see Chapter 3). By changing the gas flow rate, we can *in situ* manipulate the composition and partial pressure of the gases in the chamber. The partial pressure of the gas can be monitored using the RGA (residual gas analyzer) and the ion gauge.

Figure B.1 shows the intrinsic stress evolution in gold films in the presence of oxygen. In Figure B.1 (a), the oxygen partial pressure was fixed at 4.5×10^{-6}Torr during the initial 2000second of growth, in which a reversible stress was observed during the interruption and upon the resumption of growth. After 2000second, the oxygen partial pressure was changed to 5.0×10^{-7}Torr. Clearly, the slope of the stress curve, or the instantaneous stress, suddenly changed at 2000seconds, as highlighted using the dotted dark cyan line and the dash red line. Further analysis shows that the decrease of the oxygen partial pressure from 4.5×10^{-6}Torr to 5.0×10^{-7} Torr led to a decrease of the compressive instantaneous stress from ~75MPa to ~40MPa.

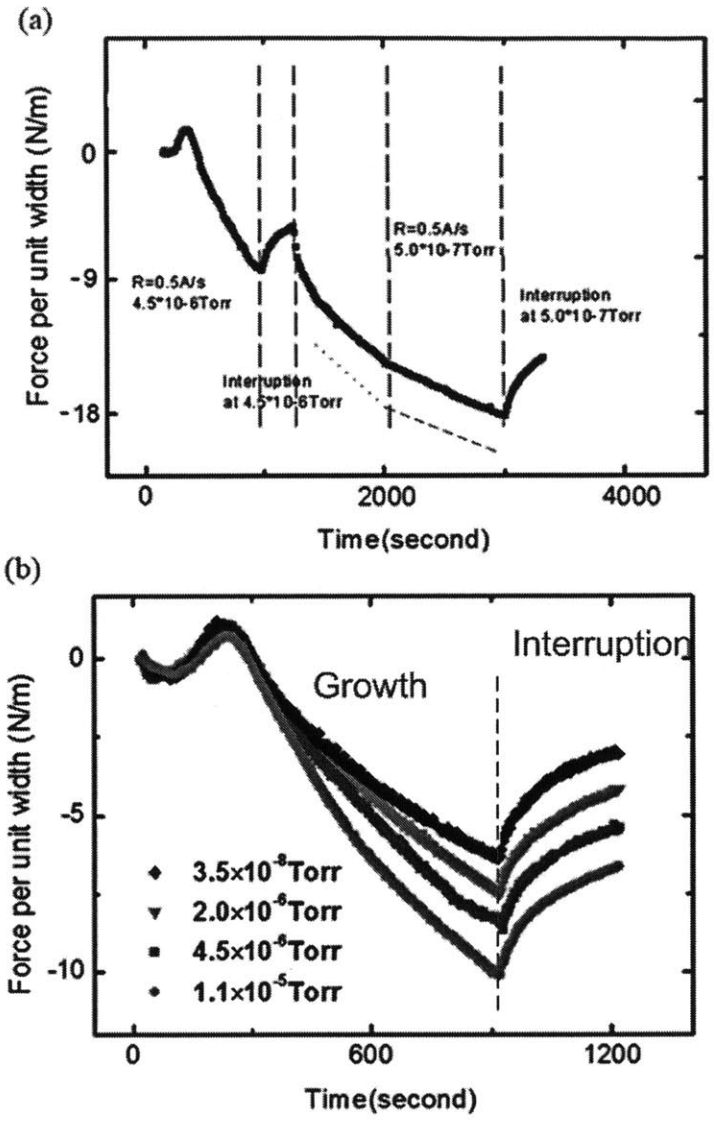

Figure B.1 . Dependence of stress evolution on oxygen partial pressure in the vacuum chamber. (a) In situ manipulation of the oxygen partial pressure during deposition of a gold film. (b) Comparison of the stress evolution in gold films, with an oxygen partial pressure of 3.5×10-8 Torr, 2.0×10-6Torr, 4.5×10-6Torr, and 1.1×10-5Torr. All the depositions were carried out at 300K, with a deposition rate of 0.5Å/s.

In Figure B.1 (b), we compare the stress evolution in gold films with different oxygen partial pressures during growth. A similar trend is found, that is, the stress becomes more compressive as the oxygen partial pressure increases. This trend might be explained as follows. During growth, incorporation of excess oxygen atoms into the grain boundaries can lead to a compressive stress in the film. In addition, the presence of oxygen may somehow suppress the grain growth process during deposition, and thereby may lead to a smaller tensile component of the intrinsic stress. As result, the overall instantaneous stress becomes more compressive as the oxygen partial pressure increases. However, the oxygen partial pressure seems to have a weak influence on the stress change during the interruptions of growth. To fully understand these phenomena, it is necessary to investigate the effect of oxygen on the structure change of the film surface during interruptions of growth.

APPENDIX C GROWTH AND DEWETTING OF POLYCRYSTALLINE FILMS ON TEMPLATED SUBSTRATES

During thin film growth, the topography of the substrate can affect the nucleation and growth processes of the 3D islands before the film becomes continuous, and may affect the surface morphology and grain structure of the film after it becomes continuous. Here we study the growth and dewetting processes of Sn and Au films on templated substrates consisting of inverted pyramidal pits. The array of pits was fabricated in (100) Si wafers using interference lithography and anisotropic etching [1]. The period of the pits is 200nm.

Thermal annealing of a continuous film can cause dewetting of the film [2-6] . If the film is deposited on templates, curvature driven surface diffusion can lead to mass transport from the mesas into the pits, and thereby lead to formation of an array of nanoparticles in the pits. For materials with high surface energy anisotropy (e.g. gold), alignment of crystallographic orientation of the nanoparticles has been observed [2, 3].

C.1 GROWTH OF TIN FILMS ON INVERTED PYRAMIDS

Tin has a very low melting temperature, 231.9 °C. Its atomic mobility is expected to be high during deposition at room temperature. This may help the mass transport process and the formation of the array of nanoparticles. Figure C.1 shows the results of 15nm and 25nm Sn

films grown on inverted pyramids. Here the films were deposited using an e-beam evaporator in MTL at MIT. The base pressure of the system was ~10^{-6} Torr.

All the films were deposited at room temperature. Figure C.1 (b) shows the formation of irregular shaped islands in a 15nm-thick Sn film. This morphology might be attributed to oxidation of the film during growth. In (c) to (f), the substrate was preheated by optical illumination using a melted tungsten source. The maximum temperature of the substrate after preheating is estimated to be around 100-150 °C. However, the exact temperature of the substrate during deposition is unknown. In these cases, deposition of Sn films on inverted pyramids resulted in ordered arrays of nanoparticles, both in the pits and on the mesas.

The size of the nanoparticles in the pits is controlled by the width of the pits. The nanoparticles on the mesas are formed by a coarsening process during deposition. As the film thickness increases, the size of these particles increases and their density decreases. The particle size and density can also be adjusted by enhancing the coarsening process, which has to be done using *in situ* annealing techniques. This is because Tin forms oxides in air, and the free energy for forming Tin oxide is lower than that for the reaction of H_2 and O_2. Therefore, annealing Sn films in forming gas cannot prevent oxidation. In addition, it should be noted that Sn films do not become continuous even if the thickness is ~1μm, probably because of the high atomic mobility. It is thus difficult to make particles accumulate in the pits by dewetting of the film.

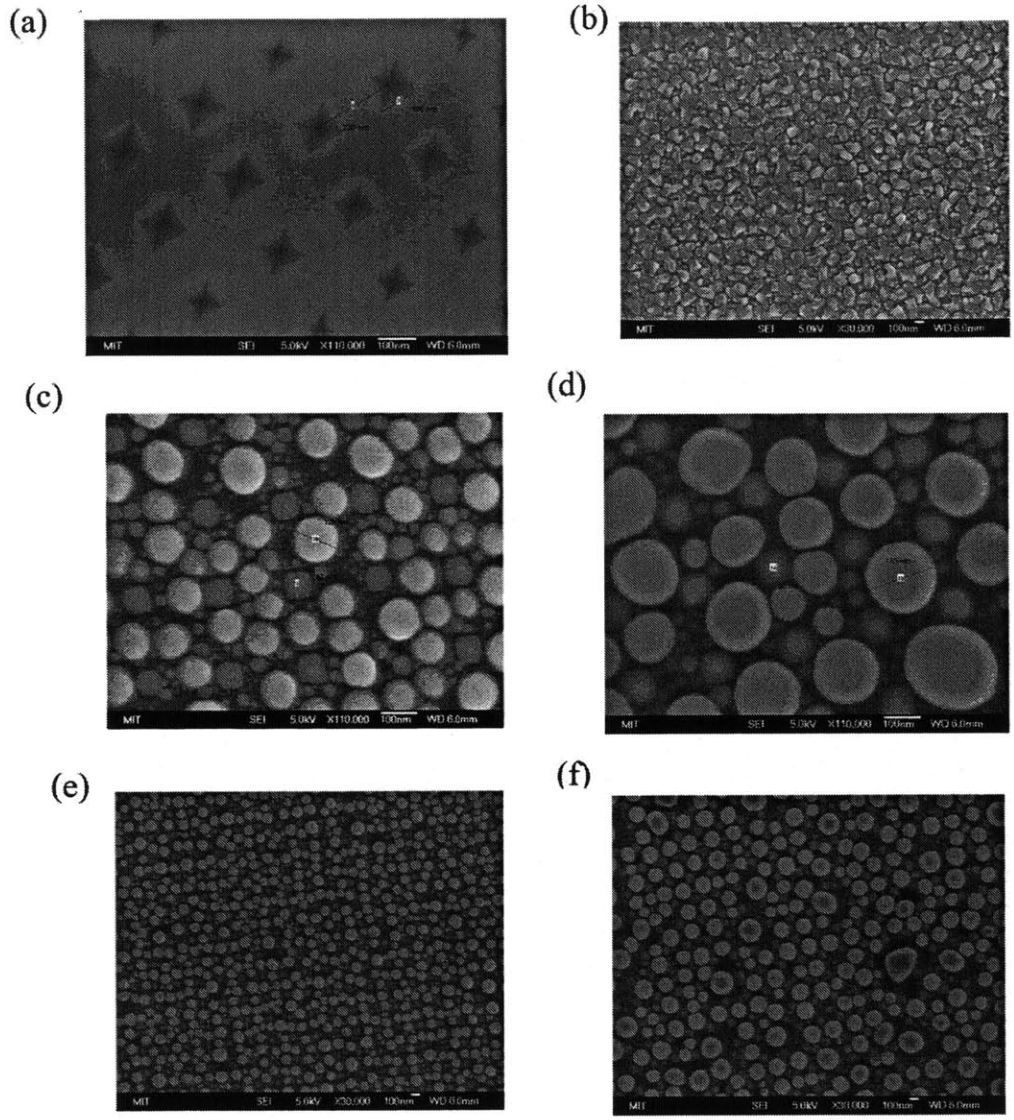

Figure C.1 (a) An SEM image of a Si substrate with periodic artificial surface topography for templating of film deposition processes. (b) Surface morphology of a nominally15nm Sn film deposited at room temperature. (c) and (e): Surface morphology of a nominally 15nm Sn film deposited at room temperature with substrate preheating.

(d) and (f): surface morphology of a 25nm Sn film deposited at room temperature with substrate preheating.

C.2 CYCLIC DEPOSITION AND DEWETTING OF GOLD FILMS ON INVERTED PYRAMIDS

Giermann and Thompson [2] have shown that dewetting of a continuous gold film on templated substrates can lead to formation of an array of nanoparticles with aligned crystallographic orientations. Here this result was reproduced. We deposited an 18nm-thick gold film on inverted pyramids at room temperature by sputter deposition. The base pressure of the system was in the range of 10^{-7} -10^{-6} Torr. After deposition, the film was *in situ* annealed at 664°C for 90mins.

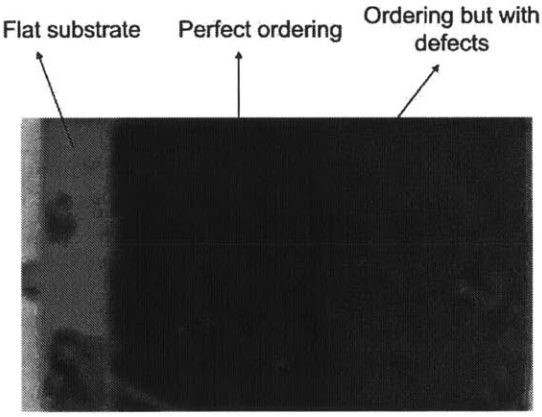

Figure C.2. A picture of a18nm gold film on a piece of templated substrate after dewetting. The size of the perfect ordering region is ~0.7cm × 0.4cm.

A picture of the sample after deposition and dewetting is shown in Figure C.2. The SEM images in Figure C.3 show that the three distinguishable regions in C.2 correspond to dewetting of the gold film on a flat region of the substrate, perfect ordering of nanoparticles, and ordering of nanoparticles but with defects, respectively. The difference in color seen in C.2 is a result of the collective scattering of light by the ordered and disordered gold nanoparticles.

(111) and (200) pole figures in Figure C.4 show that both the gold particles in Figure C.3 (b) and (c) have a crystallographic orientation close to that of (100) single crystal gold films. Compared to the gold particles in the perfect ordering region (Figure C.3(b)), the particles in the defective region (Figure C.3(c)) have a weaker alignment of the crystallographic orientation. For example, the (111) pole figure shows that there are some particles with (111) planes parallel to the substrate surface. In addition, the four-fold symmetric pattern in the (200) pole figure (Ψ ~15-45°) may suggest the formation of twins in the particles in the defective region [1].

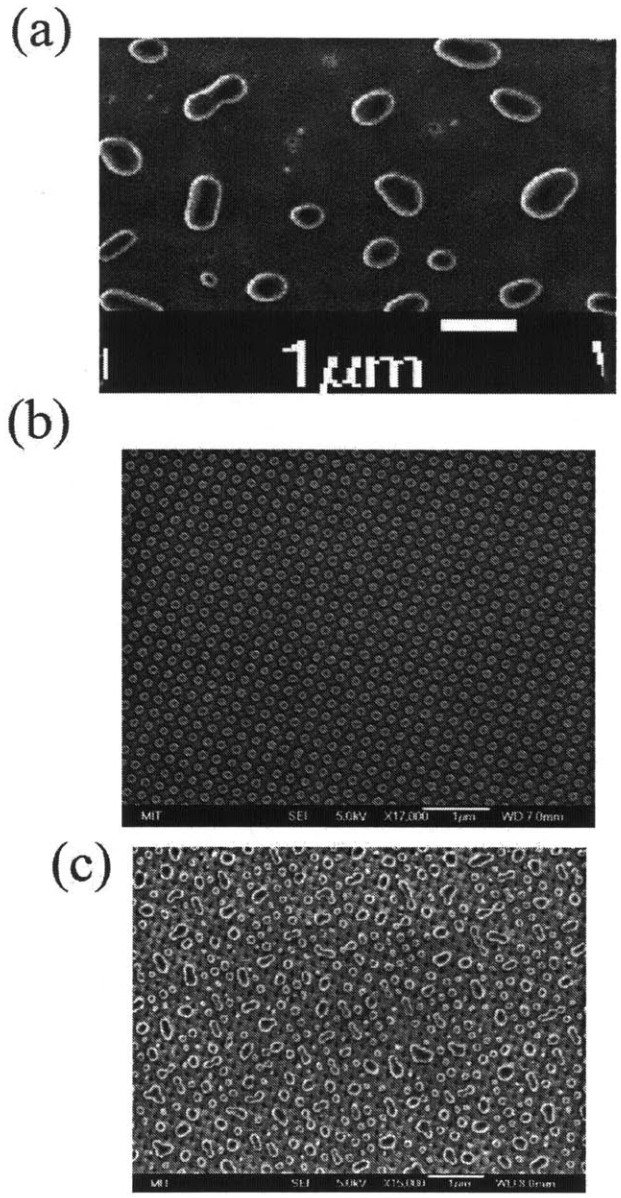

Figure C. 3. SEM images of the three regions in Figure C.2. (a) Dewetting of the gold film on a flat region on substrate. (b) The perfect ordering region. (3) Ordering but with defects.

(111)

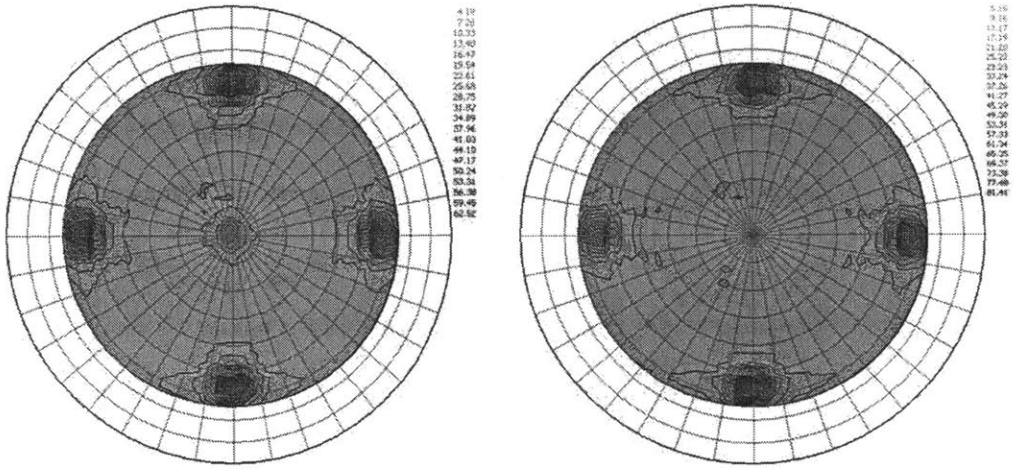

(200)

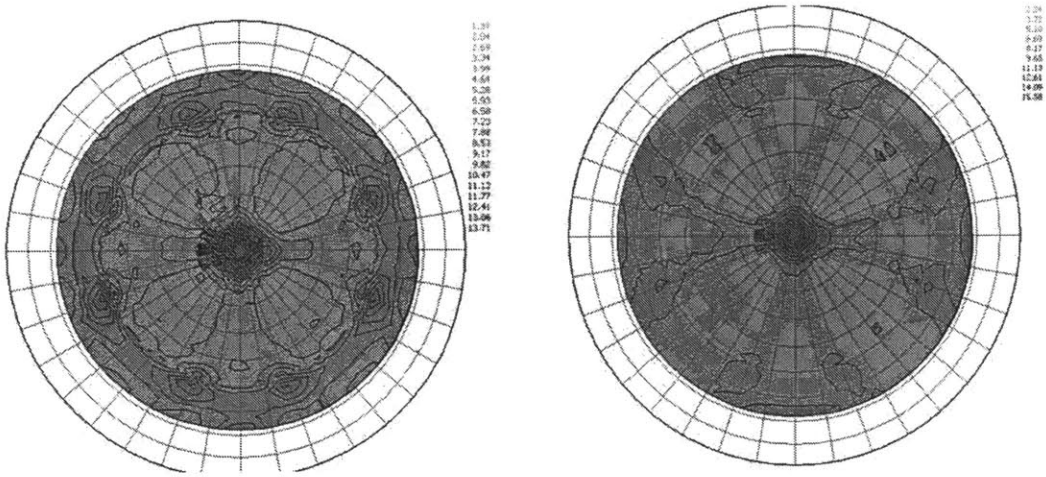

Figure C.4. (111) and (200) pole figure measurements of the gold film after dewetting. Left column: ordering but with defects. Right column: the perfect ordering region.

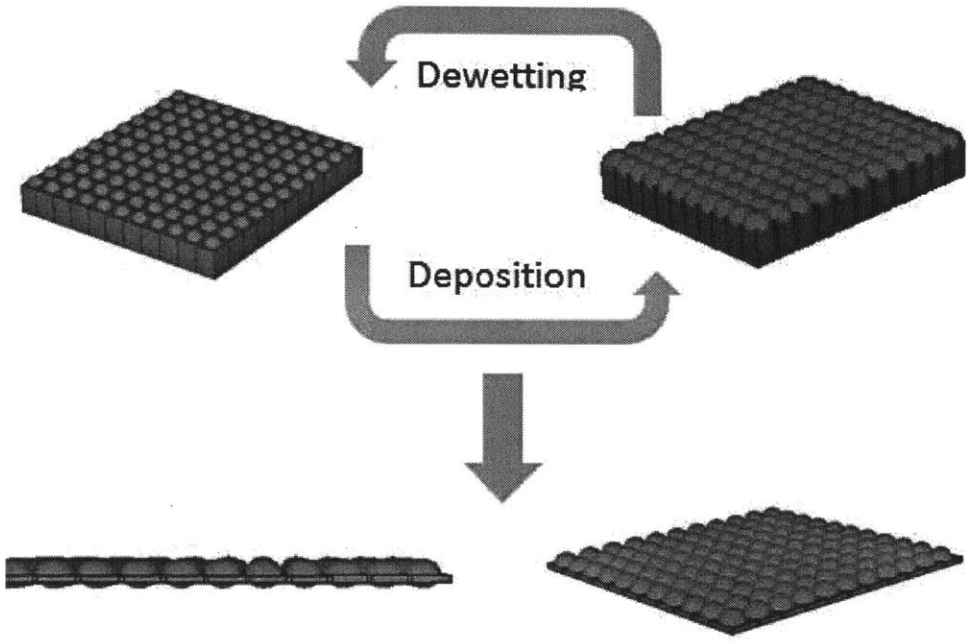

Figure C.5. Illustration of the cyclic deposition and dewetting processes.

We deposited another 14nm of gold films on the array of nanoparticles formed in Figure C.3(b). Then we annealed the sample at 600°C in a tube furnace. This resulted in an array of crystallographic orientation-aligned nanoparticles, with a larger particle size. By repeating the deposition and dewetting processes, the particle size can be increased and controlled. The cyclic deposition and dewetting processes is illustrated in Figure C.5. The experimental result is shown in Figure C.6. The 52nm-thick gold film in (d) is close to a continuous (100) single crystal gold film. However, quite a few defects can be seen in the SEM image. For future work, these defects may be eliminated by adjusting the film thickness, deposition rate and the deposition temperature during the cyclic deposition and dewetting processes.

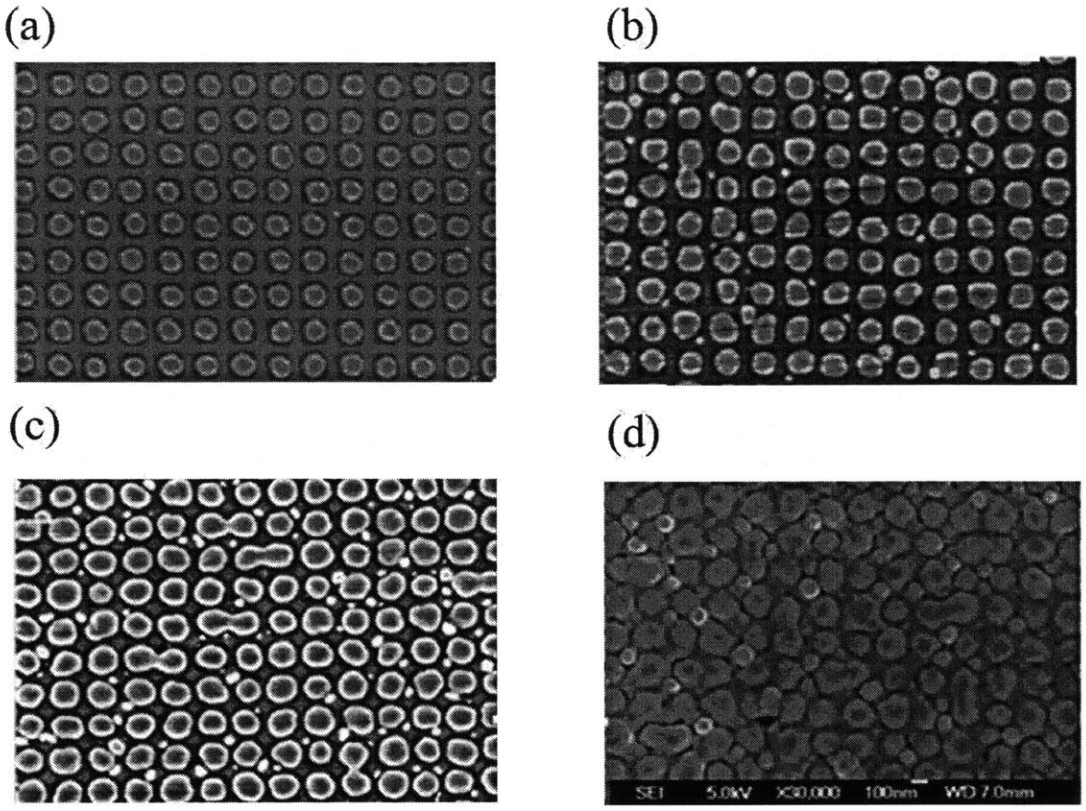

Figure C.6. Gold films on inverted pyramids by cyclic deposition and dewetting. The thicknesses are (a) 18, (b) 32, (c) 42, and (d) 52nm.

REFERENCES

[1] A. L. Giermann, (Massachusetts Institute of Technology, 2009), p. 190 p.

[2] A. L. Giermann, and C. V. Thompson, Applied Physics Letters 86 (2005).

[3] A. L. Giermann, and C. V. Thompson, Journal of Applied Physics 109 (2011).

[4] D. Kim, A. L. Giermann, and C. V. Thompson, Applied Physics Letters 95 (2009).

[5] C. V. Thompson, in *Annual Review of Materials Research, Vol 42*, edited by D. R. Clarke2012), pp. 399.

[6] J. Ye, and C. V. Thompson, Advanced Materials 23, pp. 1567 (2011).